© 2024

ELIZABETH J. CLIFFORD

ALL RIGHTS RESERVED

MULTIPHYSICS CAVITATION MODEL WITH APPLICATION TO SELF-CIRCULATING JOURNAL BEARINGS

A Dissertation

Presented to

The Graduate Faculty of The University of Akron

In Partial Fulfillment

of the Requirements for the Degree

Doctorate of Philosophy

Elizabeth J. Clifford

May, 2024

MULTIPHYSICS CAVITATION MODEL WITH APPLICATION TO SELF-

CIRCULATING JOURNAL BEARINGS

Elizabeth J. Clifford

Dissertation

Approved:

_____
Advisor
Dr. Nicholas G. Garafolo

_____
Committee Member
Dr. Christopher C. Daniels

_____
Committee Member
Dr. Saikishan Suryanarayanan

_____
Committee Member
Dr. J. Patrick Wilber

_____
Committee Member
Dr. Edward A. Evans

_____
Committee Member
Dr. Sergio Felicelli

Accepted:

_____
Department Chair
Dr. Sergio Felicelli

_____
Dean of the College of
Engineering and Polymer Science
Dr. Craig Menzemer

_____
Dean of the Graduate School
Dr. Suzanne Bausch

_____
Date

ABSTRACT

A physics-based gaseous cavitation model for a self-circulating bearing is proposed. Bearing applications often require external pumping systems to provide the necessary amount of lubricant for load carrying capacity and thermal management to maintain safe and continuous operation. A self-circulating bearing replaces the commonly used external pumping system to carry away used and heated lubricant away from the system with a wrap-around passive reservoir. A stationary porous bushing allows for the heated lubricant to flow from the bearing clearance through to the passive reservoir, where fluid can cool before being pulled back into the working zone. The eccentric shaft generates the pressure difference needed to ensure the fluid circulates naturally between these two regions. The self-circulating system will extend life expectancy of bearings in complex installations where monitoring and repair are difficult.

The stationary porous bushing was modeled with a novel closed form solution resulting from a superposition solution to the 3D Laplace equation. The passive reservoir was simplified to be a pressure distribution found in previous experimental work to be representative of the reservoir's behavior. The flow from the porous bushing into the bearing clearance was represented by Darcy's law. Due to the laminar flow within the bearing, the fluid inertia and shear between the

bushing and fluid were assumed negligible. Increasing the permeability of the bushing decreased the load capacity.

The Raleigh-Plesset-Scriven model for cavitation was used to update lubricant properties within the two-phase fluid of oil and air. The effect of allowing for the fluid to withstand tension was compared to simpler cavitation models: the load capacity of the bearing decreased.

One of the stated advantages of the self-circulation bearing is the heat dissipation from the working fluid. A thin film energy equation was applied to study the temperature effects on the fluid throughout the simulation. Comparison between a solid and self-circulating bearing with equal heat transfer coefficients confirmed that a self-circulating bearing lowered the temperature of the lubricant. The novel model developed incorporated bubble dynamics and thin film energy which allowed for proper simulation of a self-circulating bearing. The numerical model allowed for investigation of the effects of changing permeability, bushing thickness, and speed on the temperature, pressure, and cavitation of the fluid.

DEDICATION

To my family: Mike, Mom, Dad, Chase, Bridget and Rachel.

ACKNOWLEDGEMENT

The author thanks Dr. Christopher C. Daniels for his continued guidance, patience, and wisdom.

The author thanks Dr. Minel (Jack) Braun, who outlined this journey and provided a foundation which I will build upon for the remainder of my career. The author would also like to thank Dr. Nicholas G. Garafolo, Dr. Sergio Felicelli, Dr. Saikishan Suryanarayanan, Dr. Edward A. Evans, and Dr. J. Patrick Wilber for their patient review of the manuscript and their helpful recommendations.

The author sends a special thanks to their family, given and made, for their support, encouragement, and laughs.

TABLE OF CONTENTS

Page

LIST OF FIGURES……..viii

LIST OF TABLES……..xi

CHAPTER

I. INTRODUCTION 6

1.1 Self-Circulating Literature.....14
1.2 Porous Journal Bearing Literature.....16
1.2.1 Journal Bearing Boundary Conditions 16
1.2.2 Injection Velocity Representation.....18
1.2.3 Boundary Condition at the Porous-Fluid Film Interface 21
1.2.4 Porous Bushing Model.....25
1.3 Cavitation Literature 29
1.3.1 Types of Cavitation and Tensile Stress in Fluids 30
1.3.2 Cavitation Based on Single Phase Reynolds Equation.....33
1.3.3 Cavitation Based on Two-Phase Homogeneous Navier Stokes 36
1.3.4 Cavitation based on two-phase homogeneous Reynolds equation 38
1.4 Scope of Research.....39
1.4.1 Details of Completion.....40
1.4.2 Questions Answered.....41
1.5 Statement of Novelty.....42

II. SELF-CIRCULATING BEARING 43

2.1 Passive Reservoir 43
2.2 Porous Bushing.....45
2.2.1 Representation of the fluid film pressure for use by the porous bushing solution 55
2.2.2 Validation of the porous bushing solution 57
2.3 Fluid film representation.....58
2.3.1 Numerical solution of the Reynolds equation.....63

2.4 Analysis Parameters 66

III. CAVITATION DEVELOPMENT 68

3.1 Gumbel Cavitation 68
3.2 Rayleigh-Plesset Equation 68
3.2.1 Modified Rayleigh-Plesset-Scriven Equation, Void Transport 76
3.2.2 Discretization of the Rayleigh-Plesset-Scriven Equation 81
3.2.3 Fukamatsu Experiment Comparison 82
3.3 Thin film energy equation 86
3.3.1 Geometry and Material Properties 92

IV. RESULTS AND DISCUSSION 95

4.1 Effect of Bushing Pressure Representation 97
4.2 Isothermal with Gumbel Cavitation 99
4.2.1 Injection Velocity 101
4.2.2 Permeability 104
4.2.3 Effects of bushing thickness 107
4.3 Isothermal Investigations with Pseudo Cavitation 110
4.3.1 Comparison of cavitation models 110
4.3.2 Effect of changing permeability 115
4.3.2 Effect of changing thickness 118
4.3.3 Effect of changing speed 122
4.4 Thermal investigations 126
4.4.1 Solid bearing vs self-circulating bearing 128

V. CONCLUSIONS 133

BIBLIOGRAPHY 137

APPENDICES 148

APPENDIX A. MODIFIED REYNOLDS EQUATION DERIVATION 149

APPENDIX B. POROUS BUSHING SOLUTION 158

APPENDIX C. MATLAB CODE 173

LIST OF FIGURES

Figure Page

1-1: Schematic of a typical journal bearing including supply ports to provide oil from the external pumping system. 7

1-2: Schematic of a wind turbine gearbox with journal bearing [1] 8

1-3: Illustration of the main components of a self-circulating bearing. 10

1-4: Demonstration of the self-circulating concept. 12

1-5: Illustration of the wedge problem presented in work by Li [24] 23

1-6: Circumferential pressure development based on film rupture theories: (a) Gumbel [45]; (b) Swift-Stieber [46,47]; (c) JFO and Floberg; and (d) Elrod [50], and Vijayaraghavan and Keith [52] figure shared from [41]. 34

2-1: Sample supply pressure for self-circulating bearing [65]..... 44

2-2: Depiction of separated boundary conditions for the closed-form solution representing the porous bushing. 46

2-3: Flowchart for calculating injection velocity for a single grid point. 56

2-4: Validation of Porous Model with Madjumar [34]. 58

2-5: Numerical flowchart for a self-circulating journal bearing with Gumbel cavitation. 65

3-1: The spherical Rayleigh bubble within an infinite liquid. 69

3-2: Pressure inside and immediately outside the bubble and the stress acting on the surface. 70

3-3: Pressures and surface stress for the surface of a spherical bubble. 73

3-4: Comparison of void fraction without C_B (A) and void fraction calculation with C_B(B). 78

3-5: Solid journal bearing used in experiments [72]. 83

3-6: Characterization of the tensile capabilities of bubble theory cavitation models [62,72,73]. 85

3-7: The control volume for the development of the thin film energy equation. 87

3-8: Energy advection and storage for thin film energy equation. 88

3-9: Energy transfer and generation through convection, conduction, and viscous dissipation. 89

3-10: Numerical Flowchart coupling the RPS, Reynolds, energy and porous bushing equations. 94

4-1: Pressure contour within the fluid film. 96

4-2: Pressure distribution in porous bushing (H = 0.2 · R; $\omega = 5000$). 99

4-3: Effect of changing permeability on midplane injection velocity. 103

4-4: Midplane injection velocity for changing bushing thickness. 103

4-5: Maximum pressure for changing eccentricity at each permeability. 105

4-6: Load and stability analysis for changing permeability. 106

4-7: Velocity field for self-circulating bearing. 107

4-8: Load capacity as a function of eccentricity for various busing thicknesses. 108

4-9: Attitude angle for changing the thickness of the porous bushing. 109

4-10: Maximum pressure values for various bushing thicknesses. 110

4-11: Load capacity for changing permeability for each cavitation model. 112

4-12: Attitude angle for changing permeability for each cavitation model. 113

4-13: Load capacity for changing thickness for each cavitation model. 114

4-14: Attitude angle comparison of each cavitation model with different bushing thickness..... 115

4-15: Midplane pressure curves to investigate the cavitation zone for changing permeability in (a) low and (b) high eccentricity bearings. 117

4-16: Midplane pressure curves to investigate the cavitation zone for changing thickness in (a, c) low and (b, d) high eccentricity bearings. 120

4-17: Midplane void fraction curves for varying eccentricity at a bushing thickness of 0.2r. 121

4-18: Midplane pressure curves to investigate the cavitation zone for changing speed in (a) low and (b) high eccentricity bearings. 123

4-19: Load and stability investigation for changing speed with pseudo cavitation considered. 125

4-20: Temperature contours for (a) solid and (b) self-circulating bearing..... 129

4-21: Midplane void fraction and pressure comparison for a solid (a) and self-circulating (b) bearing with pseudo cavitation. 131

4-22: Load comparison for a solid and self-circulating bearing with pseudo cavitation with thermal considerations. 132

LIST OF TABLES

Table Page

3-1: Bearing parameters used to validate the cavitation model..... 84

4-1: Load results for varying grid sizes. 96

4-2: Load results for varying time steps. 97

4-3: Isothermal model settings for self-circulating bearing. 101

4-4: Isothermal model settings for self-circulating bearing with pseudo cavitation..... 111

4-5: Model settings for a thermal model with pseudo cavitation..... 127

NOMENCLATURE

A	constant for bubble radius and void fraction relationship	
A_h	pore area	(m^2)
c	concentric bearing clearance	(m)
c	specific heat capacity	$(\mathrm{J kg^{-1} K^{-1}})$
C_B	bubble concentration factor	(-)
D	bearing diameter	(m)
e	bearing eccentricity	(m)
f_k	Fourier coefficient of cosine	(-)
g_k	Fourier coefficient of sine	(-)
h	bearing clearance	(m)
H	porous bushing thickness	(m)
h_h	bushing heat transfer coefficient	$(\frac{W}{m^{2}\text{°C}})$
h_s	shaft heat transfer coefficient	$(\frac{W}{m^{2}\text{°C}})$
K	permeability coefficient	(m²)
L	bearing length	(m)
P	pressure in bearing clearance	(Pa)
P_1	pressure in Porous media	(Pa)

P_2	pressure in Porous media	(Pa)
P_b	fluid film pressure	(Pa)
P_B	bubble pressure	(Pa)
P_{B0}	initial bubble pressure	(Pa)
P_R	pressure at bubble radius	(Pa)
P_s	supply pressure from reservoir	(Pa)
P_∞	working fluid pressure far from the bubble	(Pa)
q_{gen}	heat generation	(J)
r	radial coordinate	(-)
R	bubble radius	(m)
R_{char}	characteristic bubble radius of initial bubble field	(m)
R_i	inner radius of porous bushing	(m)
R_o	outer radius of porous bushing	(m)
Re_c	cylindrical Reynolds number	(-)
T	bubble surface tension	(N)
T_s	shaft temperature	(℃)
T_h	bushing temperature	(℃)
T_0	Initial bubble temperature	(℃)
U	combined velocity	(ms^{-1})
U_1	shaft velocity	(rpm)
U_2	bushing velocity	(rpm)
u	circumferential fluid velocity	(ms^{-1})

$\bar{u}$	average circumferential fluid velocity	(ms^{-1})
v	axial fluid velocity	(ms^{-1})
$\bar{v}$	average axial fluid velocity	(ms^{-1})
V_{cell}	volume of computational cell	(m^3)
V_{inj}	injection velocity	(ms^{-1})
w	load capacity of bearing	(N)
w_r	radial load of bearing	(N)
w_t	tangential load of bearing	(N)
x	circumferential coordinate	(-)
y	axial coordinate	(-)
z	bushing axial coordinate	(-)
α	local void fraction	(-)
u_D	fluid velocity	(m/s)
β	non-Darcy coefficient	($\mathrm{m}^3\mathrm{s}^2\mathrm{kg}^{-1}$)
ε	eccentricity ratio	(-)
κ^s	surface dilatational viscosity	(N $\mathrm{m}^{-2}\mathrm{s}^{-1}$)
ρ	density	(kgm^{-3})
ρ_L	oil density	(kgm^{-3})
ρ_G	air density	(kgm^{-3})
ρ_{G0}	bubble initial density	(kgm^{-3})
σ_{rr}	bubble surface stress	(Pa)

θ	bushing circumferential coordinate (-)	
λ	feeding parameter	(-)
τ_x	axial shear	(Nm^{-2})
μ	oil viscosity	(Pa·s)
μ_G	air viscosity	(Pa·s)
μ_L	oil viscosity	(Pa·s)
ϕ	attitude angle	(deg)
ω	journal angular velocity	(rad/sec)
γ	static surface tension	(N)

CHAPTER I

INTRODUCTION

The purpose of a bearing is to allow two parts, called the bushing and shaft, to rotate independently relative to one another. In a journal bearing, the bushing and shaft are cylindrical in shape, and a lubricant fills the space, or clearance, between the two parts. An external radial load is transmitted through the bushing-lubricant-shaft assembly, shown in Figure 1-1. The external load causes a radial offset between the bushing and shaft centerlines known as the eccentricity. The radial displacement forms a convergent and divergent region in the clearance's fluid film. With relative rotation between the bushing and shaft, fluid pressure increases, creating a load-carrying film. Since pressure changes are intensified by increased rotational speed, so is eccentricity.

The pressure decreases where the fluid film widens in the divergent area. If the pressure decrease is significant, the fluid may rupture, which is called cavitation. The rupturing fluid does not support load, and cavitation can cause damage to the shaft and bushing, decreasing both performance and bearing life.

One can infer that preventing fluid rupturing is a top priority when designing a bearing for a specific application.

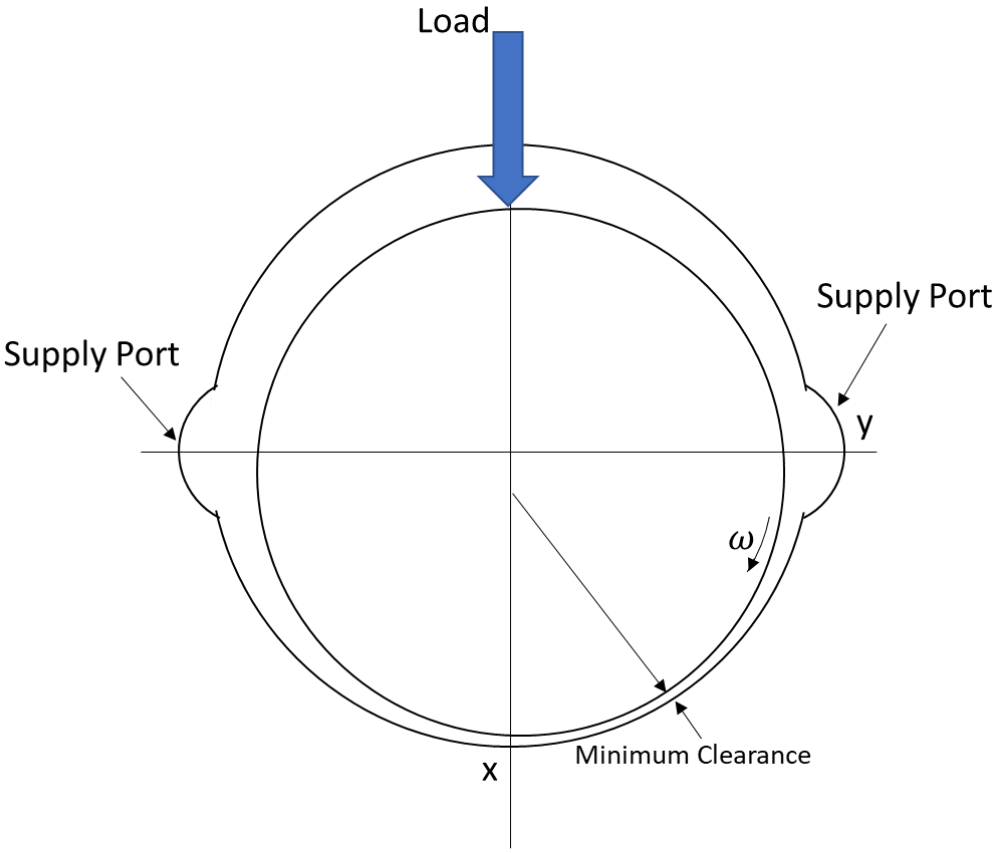

Figure 1-1: Schematic of a typical journal bearing including supply ports to provide oil from the external pumping system.

Under most conditions, the location of the shaft's centerline relative to the bearing remains fixed. At select combinations of geometry, fluid viscosity, rotational speed, and external load, the relative positions of the shaft and bearing centerlines are dynamic and oscillatory. This is called bearing instability and is undesirable, so bearing designers avoid these conditions.

Journal bearings have extensive history and usage. One example is within gear boxes. Figure 1-2 shows a journal bearing comprised of a planet gear supported by a journal bearing. Within the sample gearbox shown, each planet gear is an example of a journal bearing. Journal bearings are also present in engines and a multitude of applications where the shaft and bearing need to rotate independently and support a load. In addition to the journal bearing, an external pumping system is needed to supply replacement fluid for the inevitable leakage. The supply ports (Figure 1-1) show how the fluid would enter the bearing clearance.

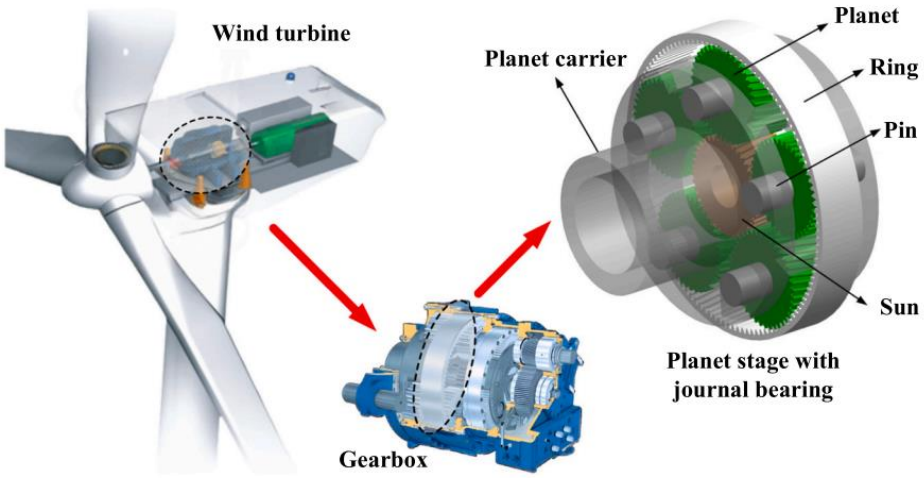

Figure 1-2: Schematic of a wind turbine gearbox with journal bearing [1].

As today's designers demand more performance, bearing temperatures increase and lubrication systems require new circulation and thermal conditioning solutions. Proposed remedies to high lubricant temperatures have taken many

forms: air-based solutions, powder lubricants, and liquid metal lubrication systems [2]. A novel self-circulating system was patented by Dr. Minel Braun et al. [3] and is the focus of this investigation. The proposed system eliminates the need for an external pumping system. Instead, the pressure differential between the converging and diverging portions of the bearing circulates fluid through a porous bushing between the fluid-film clearance and a passive reservoir. The circulation of the fluid allows for heat dissipation, prevents cavitation, and preserves the stability and integrity of the lubricating fluid. Figures 1-3 and 1-4 illustrate the self-circulating concept. Figure 1-3 demonstrated the eccentricity ratio of the bearing, ε, which represented the offset between the shaft and bushing as well as the relevant forces used to support the shaft.

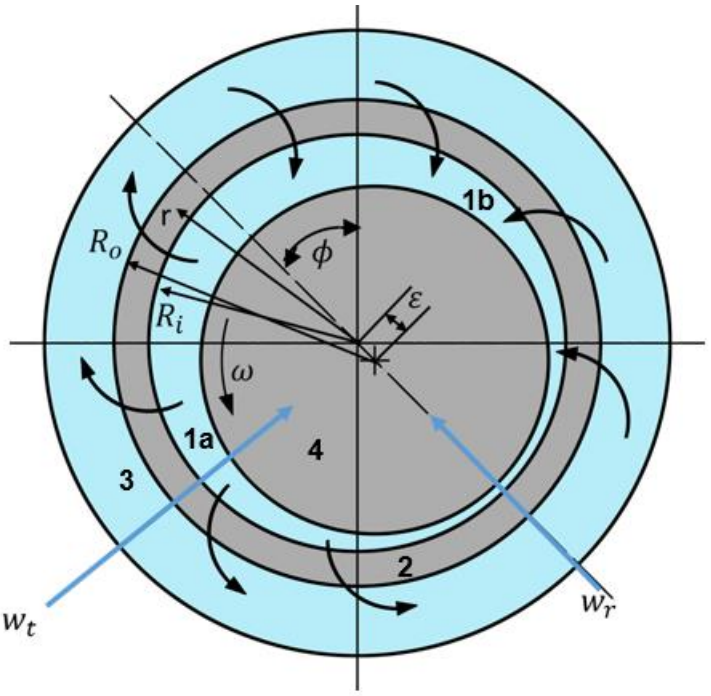

Figure 1-3: Illustration of the main components of a self-circulating bearing. Locations 1a and 1b are the convergent and divergent zones of the fluid film, respectively. Component 2 is the porous bushing. Region 3 represents the passive reservoir. Component 4 is the bearing's shaft.

The shaft (component 4 in Figure 1-1) is a standard journal bearing component and is not altered for the self-circulating bearing. The fluid film behaves much like in a standard porous journal bearing. The relationship between the convergent and divergent zones (locations 1a and 1b respectively) of the fluid film play a key role in the function of the self-circulating bearing. The porous bushing (component 2) replaces the solid bushing of a typical journal bearing and allows fluid to flow from the clearance to surrounding reservoir and

vice versa. The porous bushing has a variety of parameters that affect the ease with which fluid flows between the fluid film and reservoir (region 3). Two important porous bushing properties are the permeability and porosity. Porosity is the fraction of void to total volume [4]. Permeability is a macroscopic measure of the medium's ability to transmit fluid through it [5]. In this work, permeability will be varied and its effects on the exchange of fluid and bearing characteristics studied. Apart from permeability, thickness of the porous bushing also affects the amount of fluid that passes through the bushing. A thicker porous bushing makes the fluid's path through the matrix more difficult. While this reduces the magnitude of the injection velocity, it allows for more cooling of the fluid before it enters the new domain since the bushing acts as a heat sink.

Figure 1-4 illustrates the typical lubricant flow through the porous bushing around the bushing's circumference. From 0 to 180º (area 1), the arrows depict the lubricant moving out of the fluid film and into the reservoir due to the elevated pressure (P) in the converging fluid film relative to the reservoir pressure (Ps). The reverse is true between 180 and 360º of area 2, the divergent section of the bearing, where the fluid film pressure drops below the reservoir pressure. Here, the lubricant flows from the reservoir into the bearing clearance. This demonstration neglects any effects of the porous bushing.

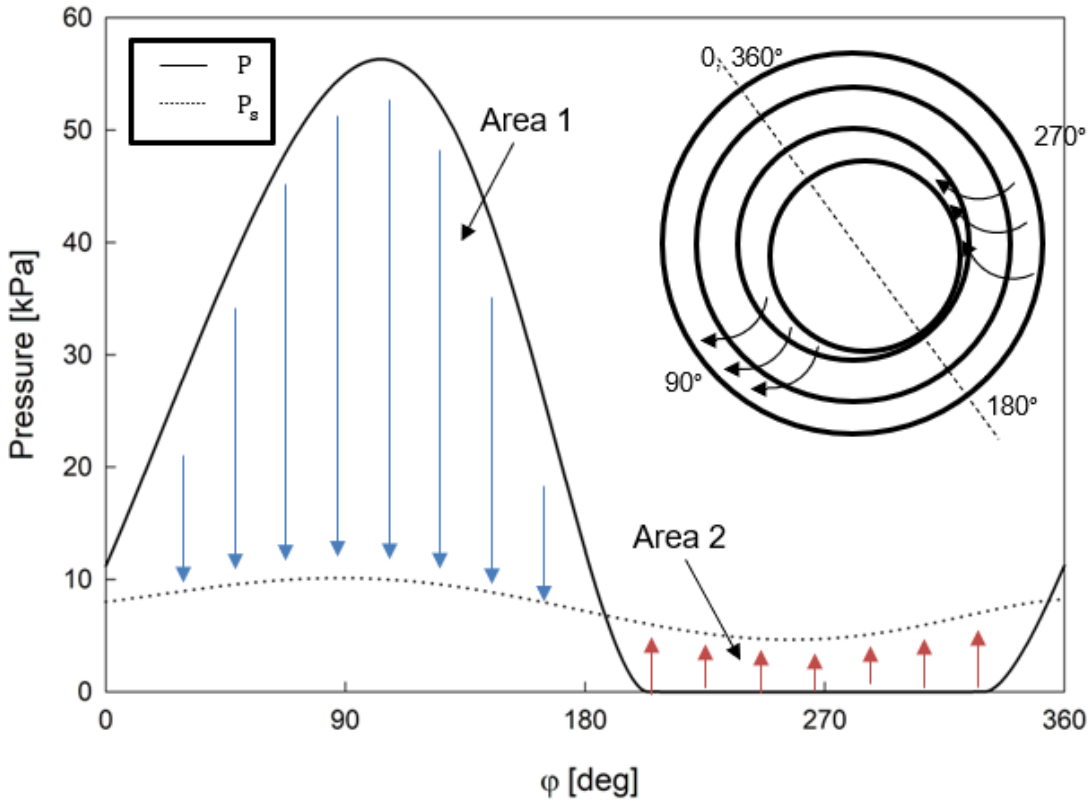

Figure 1-4: Demonstration of the self-circulating concept. Area 1 represents the area where the lubricant pressure is higher than the reservoir, so fluid will flow out of the bearing clearance and into the reservoir. Area 2 represents the diverging section of the bearing, where the pressure in the fluid film is lower than the reservoir pressure. In area 2, fluid will flow from the reservoir and into the bearing clearance.

The injection velocity, a result of the pressure differential within the porous bushing, also has characteristics that warrant a brief discussion. Historically, there have been three main methods for representing the injection velocity into the fluid film from a porous bushing. The first is known as Darcy's law (Equation 1.1).

$$\frac{\Delta P}{L} = -u_D \frac{\mu}{K A_h} \tag{1.1}$$

Darcy's law describes the flow due to pressure change and accounts for the permeability of the flow path and the fluid viscosity. The inclusion of additional resistance due to inertial forces is represented by the addition of the Forchheimer term, the second term on the right-hand side of Equation 1.2.

$$\frac{-\Delta P}{L} = \frac{\mu}{K A_h} u_D + \frac{\beta \rho}{A_h^2} {u_D}^2 \tag{1.2}$$

The Brinkman term extends the representation of fluid flow to incorporate the pressure change, inertial effects, and the viscous shear of the fluid in Equation 1.3. This equation is a result of the assumption that particles in the fluid are spheres held in place by external forces, in a bed of closely packed particles which support each other by contact [4].

$$-\nabla p + \mu \nabla^2 u_D - \frac{\mu}{k} u_D = 0 \tag{1.3}$$

Various studies have focused on the improvement of different representations of the injection velocity which conclude that for most applications Darcy's law is a sufficient representation of the injection velocity [5,6]. The injection velocity is connected to the fluid film pressure as the V_{inj} term within the Reynolds equation, Equation 1.4.

$$\frac{\partial}{\partial x}\left(\frac{\rho h^3}{12\mu}\frac{\partial P}{\partial x}\right)+\frac{\partial}{\partial y}\left(\frac{\rho h^3}{12\mu}\frac{\partial P}{\partial y}\right)=\frac{\partial(\rho h)}{\partial t}+\frac{\partial}{\partial x}\left(\frac{\rho h U}{2}\right)-\rho V_{inj} \qquad 1.4$$

In this work, the Reynolds equation is used to represent the pressure within the working fluid. The detailed derivation and assumptions of the Reynolds equation are found in Chapter 3.

1.1 Self-Circulating Literature

The self-circulating literature begins with the work of Johnston et al who modeled the passive reservoir of a linear slider bearing [8]. The model created by Johnston et al. investigated the range of parameters that would produce the conditions of a virtual pump to circulate the fluid through the porous medium. The results of the study indicated that the maximum pressure generated inside the film increases in a nearly linear fashion with the velocity of the slider. Johnston also found that decreasing the depth of the reservoir increased the pressure in the fluid film, but this occurred at the expense of the flow circulation in the bearing clearance. The pressure inside the film increased nearly linearly with the

porous medium thickness up to a limiting porous medium thickness, after which the trend was reversed. As the permeability was increased, the hydrodynamic pressure generated decreased within the slider bearing. The simulation proved that the self-circulating mechanism is enabled by the convergent-divergent shape of the film which acted as a virtual pump, transferring fluid between the active film and reservoir. Johnston proposed that the work presented would mimic the behavior of a long reservoir-extended porous journal bearing.

Balasoiu et al. extended Johnston's work to a self-circulating cylindrical journal bearing and analyzing the relationship between various parameters and the stability of the bearing [1]. This work used a commercial code, CFD-ACE+, and finite volume method to analyze a 3D isothermal model. The Forchheimer term accounted for the pressure drop due to inertial effects induced by high velocity flows. Balasoiu focused on how the flow within the bearing operated and the effect of various bearing parameters on operation. It was shown that a higher permeability allowed for superior circulation but lowered the load carrying capacity of the bearing. An increase in porosity for constant permeability showed the same effects. It was concluded that a compromise between the permeability, porosity, and desired bearing characteristics must be made. The new type of bearing was recommended for high permeability ranges of $1\ x\ 10^{-10}\ m^2$ and $1\ x\ 10^{-11}\ m^2$. The use of commercial software limited the control over the cavitation model.

1.2 Porous Journal Bearing Literature

Porous journal bearings have been extensively studied with publications by Cameron as early as 1962 [9]. The knowledge base will be highlighted for the aspects most relevant to a self-circulating bearing application. The porous literature overview is organized into four main categories: journal bearing boundary conditions, injection velocity representation, porous-fluid film interface boundary conditions, and porous bushing models. Most papers utilize periodic boundary conditions in the circumferential direction of the bearing and thus it can be assumed that these are the conditions in the discussed publication unless otherwise noted. The axial ends of the bearing are either exposed to atmospheric pressure or in a few cases sealed to create a higher pressure within the bearing to increase the load capacity [10]. The axial condition will only be noted if the sealed end condition is employed.

1.2.1 Journal Bearing Boundary Conditions

Prior to the computing advancements present today, simplifications were often made regarding the length of the bearing. A short or long (infinite) bearing assumption meant that either the axial or circumferential direction respectively could be neglected. This allowed for easier numerical models or in some cases closed form solutions for the journal bearing lubricant pressure.

Shir studied the infinitely long bearing in the hydrodynamic porous region [11]. The work looked at the effects of permeability with all other variables held constant. It was found that permeability moved the maximum pressure location and decreased the resultant pressure-force resultant and total-force. The effect on the torque and shear stress due to increases in permeability were less significant. A small clearance, or eccentricity ratio near unity, were found to make the effects of permeability more pronounced.

Murti studied hydrodynamic lubrication of long porous journal bearings [12]. The porous medium was represented by the addition of a Darcy term to the modified Reynolds equation. The boundary conditions used were periodic for the fluid film, pressures equated at the interface, and a no slip condition at the outside of the porous bearing. Others used this no-slip boundary condition including Cusano [13].

While advancements in technology have eliminated the necessity for these simplified geometries, the initiators of the field need to be recognized. The representation of the injection velocity from the porous bushing is often still represented the way early authors proposed [12]. The fundamentalists provided concise solutions to the pressure within the simplified bearing that serve as good validation for today's more complex models.

1.2.2 Injection Velocity Representation

While early studies used Darcy's law to represent the injection from the porous medium, there were concerns about its accuracy. Neale [14] studied the practical significance of the Brinkman-Extended Darcy model and stated the Darcy equation is not compatible with the existence of a boundary layer region in the porous medium because no macroscopic shear term is associated with this equation [14]. Upon further investigation however, it became clear that Darcy's law is valid for flow outside the boundary layer. Thin channels were cautioned as they can exhibit larger effects on external flows from the boundary layer. This literature supported the working assumption that if the overall effects of external flow are being examined and not the flow patterns nor boundary layers, the Darcy term represents the porous medium well.

Boundary layer thickness was again found to increase the load capacity and decrease the coefficient of friction and attitude angle of a bearing in Lin's 1993 paper [14]. Here, the Brinkman-Extended Darcy model was used to analyze the hydrodynamic lubrication of short porous journal bearings. The effects of the boundary layer region were found to increase the pressure distribution and thus the load capacity of the short porous journal bearing when compared to the Darcy model with and without slip conditions. The friction parameter and attitude angle were also decreased in comparison to the Darcy model. It was noted that a higher eccentricity ratio and/or a higher permeability parameter increased the

effects of the boundary layer. This conclusion agreed with Rouleau [16], with both mentioning that a thin, porous wall increases these effects.

Cieslicki [17] presented an investigation of the effect of inertia on the flow of air through porous bearing sleeves. The Forchheimer term was used since, for the same pressure drop, the velocity of gas was at least a magnitude higher than for oil. Cieslicki concluded that the inertial effects must be considered when analyzing the flow characteristics in moderate and low porosity porous sleeves. In the investigation, two distinct zones were established: a weak inertia zone of small seepage velocity and the Forchheimer zone. Future work was recommended to establish the coefficients used to describe the flow in the first parabolic zone, represented by a parabolic fit, as well as the second zone, represented by a linear fit. Authors drew no conclusions for oil applications, but a case could be conjured that Darcy's law alone is sufficient for an oil application due to the lower velocities for identical pressure drops.

Hwang [18] studied the significance and effect of the Brinkman-Extended Darcy model using an unwrapped journal bearing geometry. The methods and results could still be considered relevant for along porous journal bearing. Hwang found that the Brinkman-Extended Darcy model predicted increased load capacity and decreased friction coefficient. This makes sense because Brinkman term represents the viscous shear terms which create a higher pressure. Another conclusion was that the viscous shear effects on the

bearing characteristics progressively increase when a thicker porous bearing was studied.

The practical significance of the Brinkman-Extended Darcy model was also investigated by Neale [19]. It was concluded after deriving the Beavers and Joseph [20] semi-empirical theory with Darcy's law including slip flow boundary conditions that it produced identical results to those derived using Brinkman's extension of Darcy's law with rigorous boundary conditions. Beavers and Joseph explored the change in velocity in the boundary layer with flow through a porous medium. Darcy's law neglects this change in velocity; authors presented a simple theory to replace this boundary layer effect as a slip velocity in conjunction with Darcy's law to properly represent the flow. [20] "For flow outside of boundary layer regions the Brinkman equation reduces, practically speaking, to the widely utilized Darcy Law." [19] It was cautioned that no matter how small the boundary layer is, it can have surprisingly significant effects on the external flow in thin channels.

The various works on the injection velocity, particular applications for each of the three representations can be made. The Forchheimer term is necessary for high velocity applications, particular examples included air bearings. The Brinkman term was recommended for study of the boundary layer. For most cases, Darcy's law was sufficient to account for the injection of fluid from the porous medium into the bearing clearance. Darcy's law can be further improved with boundary conditions at the fluid film-porous interface.

1.2.3 Boundary Condition at the Porous-Fluid Film Interface

As highlighted by Elsharkawy [21], there are four main cases of boundary conditions studied for porous bearings: no slip, velocity slip condition, shear stress continuity, and shear stress jump at the interface. While certain applications and specific studies on the flow within the porous medium require more complex boundary conditions, the velocity flow field within the porous bearing is low and the no slip boundary condition can be utilized.

Two studies by Cusano and Murti focused on a no slip boundary condition. Cusano [22] utilized the no slip boundary condition and compared the finite bearing to long and short bearing approximations. He concluded that the finite bearing solution predicted a higher eccentricity ratio for a given load than either approximation. The load-eccentricity curves presented compared the porous approximations to an experimental solid bearing. The experimental results validated the numerical model and geometry assumptions as well as the no slip assumption. Murti [23] also used a no slip condition for a long porous bearing. The conclusions drawn were that the load capacity of porous bearings progressively decreased with the permeability parameter and that there was a more even pressure distribution in the film as the permeability parameter increased.

The second condition is a velocity slip condition that specifies a velocity at the boundary to represent the change in velocity a boundary layer would present. Li [24] studied non-Newtonian fluids in a wedge bearing to model the

microstructure of lubricating surfaces as thin, porous film press fitted on an impermeable substrate. The modified Reynolds equation was used with the Brinkman-extended stress jump boundary condition. It was concluded that the flow resistance in the porous region increased as the permeability decreased, as the stress jump parameter decreased, as the viscosity ratio increased, or as the porous film thickness increased. Li demonstrated that increased flow resistance resulted in larger load capacity. This study did not investigate journal bearings specifically.

Stress jump at the interface was the boundary condition used in Li's paper. [25] This model was applied to thin film lubrication problems. The model was made with four material properties: viscosity ratio, porous thickness, stress jump parameter, and permeability. The effects of these properties on the interfacial velocities, velocity distributions, and the performance of a 1D wedge problem were discussed. A wedge bearing differs from the journal bearing in both sides of the film clearance bound by porous media. A modified Reynolds equation was used to represent the working fluid’s flow. The work is relevant to a journal bearing because of the small clearance present and similar velocities and representations of the flow between and within porous media.

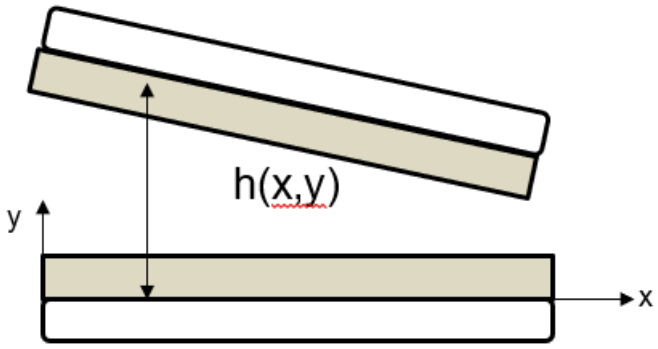

Figure 1-5: Illustration of the wedge problem presented in work by Li [24].

It was concluded that the stress jump parameter had significant effects on the velocity distribution and bearing performance amongst other effects of the material properties applicable to the 1D wedge problem. The study did not compare with experimental values, only corrected Darcy's law with slip-flow effects. This publication claimed, "The slip flow postulation, as well as Darcy's law, is valid only in a dense porous medium of large thickness, so that the variation of velocity in it can be neglected and the flow is depicted by the Darcy equation". Thickness varied from 0.5% to 40% of the film clearance and was not always equal for each side. This disagreed with previous theory that of low flows the effects of inertia represented by the Brinkman extension were not necessary for accurate representation for the velocity and geometry of the slider bearing which differs from the unwrapped journal bearing.

Li [26] derived a modified Reynolds equation using Brinkman-extended Darcy model with stress jump boundary conditions to account for viscous shear effects. The porous medium and fluid film were connected by equating velocities of the fluid at the interface. There was a no slip boundary condition at the outer radius of the porous medium in contact with an impermeable casing. The stress jump condition was used because of the difference in between the porous layer and the clearance. Conclusions were drawn after varying four parameters. Large interfacial velocity resulted if there was a small viscosity ratio, large stress jump parameter, large permeability, or large boundary velocity. Large load capacity was achieved for small values of the stress jump parameter, small permeability, large film thickness if the stress jump parameter is less than 0.8, or a large viscosity ratio if the stress jump parameter was less than 1. It was concluded that the stress jump parameter significantly affected the velocity distribution and bearing performance.

Elsharkawy [27] began with the simplified Navier Stokes equations, deriving modified Reynolds equations for the fluid film and the porous regions. A stress jump parameter was used as the boundary condition for the fluid film-porous medium interface. The numerical model successfully predicted the experimental results previously published for porous journal bearings. The stress jump parameter had little effect on the load carrying capacity up to an eccentricity of 0.9; above this value the load capacities deviated from experimental results. Elsharkawy included the effects of dimensionless permeability parameter and

stress jump parameter on performance parameters such as load carrying capacity, side leakage, friction factor, and attitude angle. The author's conclusion that a stress jump boundary condition only affects high eccentricity (above 0.9) cases is relevant for the current work.

Van Buuren [6] utilized the dimensionless form of finite Reynolds equation for porous bearing and suggested that boundary conditions do not have to change even though the no slip condition is clearly not applicable physically. The pressure distribution and the bearing dynamics were found by integration. Van Buuren used Galerkin's method to solve and demonstrated the computational cost saved. Galerkin's method converted the continuous differential problem to a discrete problem determined by a finite set of basic functions. The relevant takeaway for present work is that a no slip condition does not affect the results of the bearing even though physically it is not accurate. The additional computational costs of a different boundary condition do not appear worthwhile.

1.2.4 Porous Bushing Model

While the porous bushing is typically modeled with the Laplace equation to represent 3D flow of fluid, differences arise in the simplifications made for this Laplace equation. While Rhodes [28] used the modified Reynolds equation connected to the LaPlace equation in the porous media by conservation of mass, some simplifications were made that differentiate it from the study presented here. One such simplification was the narrow bearing approximation, which

neglected the variation of the pressure in the circumferential direction. The approximation was applied in the bearing as well as the porous media. The ends of the bearing were sealed, whereas the axial boundary conditions presented in the current work are open to atmospheric pressure. Darcy's law was used to represent the injection of fluid into the bearing from the porous media. A product solution was used for the 2D pressure. Garlerkin's method was used to obtain the infinite series solution for the pressure. It should be noted that in the formation of the closed-form solution, dimensionless parameters were used.

Rouleau [29] again used a product solution with infinite series to solve the continuity equation that represented the porous medium. A narrow bearing assumption limited the continuity equation to two dimensions. The homogeneous boundary conditions required for the product solution were a symmetry in the axial direction and a press-fit porous bushing. The pressure at the axial ends of the bearing was equated to ambient pressure.

Kaneko [30] used a 3D continuity equation in the porous medium that was solved numerically in dimensionless form simultaneously with the modified Reynolds equation. End leakage was accounted for in the conservation of mass between the porous medium and the fluid film. The outer boundary of the porous medium was split into two parts, one where the boundary was a press-fitted section against the solid housing and the other a circumferential groove in the housing where the pressure was given by an equation specified in the paper. Continuity via pressure was maintained between the porous matrix and oil film.

In another investigation, Kaneko [31] investigated an improved boundary condition between the convergent and divergent sections of the fluid. The proposed boundary condition aimed to improve upon the quasi-Reynolds boundary condition as well as the continuity equation based on a balance between oil fed into the clearance through the porous matrix and that lost from the ends through the clearance gap. The quasi-Reynolds boundary condition produced all positive pressures, neglecting cavitation while the new proposed boundary condition accounts for negative pressure values. The effects of changing the Sommerfeld number and dimensionless oil-feed pressure on the angular extend of oil film qualitatively agreed with the experimental data, however there was a quantitative difference. The location of the trailing end in experimental results moved towards the downstream region as compared to that in the computed results. Experimental results also showed the pressure being negative right before the trailing end of the oil-film region; this was not predicted by the Reynolds or quasi-Reynolds condition. The proposed momentum theorem was applied to the oil-film region in the clearance gap of the porous journal bearing to obtain the circumferential boundary condition for the oil-film pressure. Applying Darcy's law to the 3D continuity equation gave the equation for flow in the porous medium. After solving the equations numerically, the proposed momentum boundary condition in the circumferential direction was shown to improve the numerical prediction. The negative pressure before the trailing end was present and the location of the trailing end is moved downward as seen in

experimental results. The solution was obtained by simultaneously solving the Reynolds and continuity equations with an over-relaxation scheme.

Meurisse [32] stated in the introduction of 'A 3D conservative model for self-lubricated porous journal bearings in a hydrodynamic steady state' that porous bearings have a lower load capacity than their solid counterparts. Elrod's cavitation model, described further in Chapter 1, was included along with the Reynolds equation and Darcy term for the injection velocity. A thorough explanation of model assumptions and how to prevent outside leakage so that a steady state dynamic model is possible was included. The porous medium while represented by 3D Laplace equation, as others have, was solved with a substitution method unique to Meurisse [32]. The effect of pore closure on the behavior of the model was a focus of the work. Three main influences on the life of the bearing were summarized: cavitation pressure must be less than atmospheric pressure, diameter of the pores (at least at the barrier layer) must be small enough to prevent air from entering, and the rate of pore obstruction in pressure zone (obstruction limits the oil leakage at the outer surface of the bearing).

Air bearings present a stepping stone to the self-circulating bearing, discussed further in the validation of the self-circulating porous bushing. Unlike typical porous bearings which are press fit into a sleeve so that the outer boundary condition of the porous bushing is homogeneous boundary condition preventing flow through the sleeve, air bearings often have a constant supply

pressure surrounding the porous bushing. The supply pressure and lack of cavitation lend to a convenient validation of the porous bushing model before accounting for a changing supply pressure. Lee [33] and Majumdar [34] both validated with results from Sun's experiments [35] which were also used to validate the porous bushing model presented here. The main advantage the air bearing validation is the exclusion of cavitation effects that may occur in liquid lubricated bearings.

While recent literature agrees there is need for a 3D representation of the porous bushing, the avenue to solve that distribution remains unsettled. Some investigators have simplified the bearing geometry overall, some benefited from a press fit, and others used a product or substitution method to tackle the three-dimensional pressure solution. This review identified a clear need for an efficient, standardized three-dimensional solution for the porous bushing.

1.3 Cavitation Literature

The cavitation literature was organized by the stage of development. Initial models reflect the start of a new field as well as computational limitations. Experiments that assisted in the development of the understanding of cavitation are outlined in sequential order. Models started with the assumption of a single-phase working fluid. Developments within this phase focused on the representation of tensile pressure in the fluid. The next two phases approach a two-phase working fluid from either a Navier Stokes or Reynolds origin. A

Reynolds origin neglects the inertial terms of the fluid and the third dimension of both the fluid and cavities present within. The two-phase approaches allowed for improvement on the film rupture and reformation boundaries. Most recently, the improvements have focused on numerical stability.

1.3.1 Types of Cavitation and Tensile Stress in Fluids

Cavitation treatment has been studied since initial works by Reynolds and Sommerfeld [36-37]. The depth of knowledge and cavitation have continued as technology improved. The Sommerfeld model provided for liquid to withstand negative pressure equal in magnitude to the positive pressure. While liquid can withstand some level of tensile forces, the magnitude has since been found to be lower than this initial model. Sub-atmospheric or sub-cavity pressures are referred to as ‘negative pressures’. Under certain circumstances, a fluid can sustain rather significant tensile stresses. Temperly [38] presented experimental work in addition to theoretical developments in which fluids were shown to sustain significant levels of tension when there is (a) static application of tension, (b) ‘once-only’ pulse tension, or (c) oscillating tension through acoustic means. Previously, Temperly had studied tension within water and found that considerable differences were seen when using different methods such as those modeled by Bertholet [39] and Reynolds [36]. Temperly experimentally found that the concentration of air within the fluid would also present vastly different tolerance to sustaining tension within the fluid. Fisher [40] affirmed that a liquid

under tension is in a metastable state where vapor bubbles appear spontaneously and continue to grow until the system's pressure achieves the equilibrium vapor pressure.

Experimental cavitation investigations continued with Natsumeda and Someya [41] using a rotating pressure transducer. In 2006, Adiletta and Della Pietra [42] used bushing mounted piezo and strain gauge pressure transducers in a squeeze film damper to register 'spikes' in pressure preceding film rupture. They associated these tensile stresses with sub-cavity pressure and conditions of rupture due to vapor cavitation.

Liquid cavitation has three forms: gaseous, pseudo, and vaporous cavitation. The definitions for these types of cavitation in this works were defined by Braun et al. [43].

1. 'Gaseous cavitation' generally contains one or more gas species dissolved in the fluid and occurs as the pressure falls below the saturation pressure of the particular gas component.

2. 'Pseudo-cavitation' is a form of gaseous cavitation during which the gas bubble expands on account of depressurization without further gas mass diffusion from the liquid to the gas phase.

3. 'Vaporous cavitation' is the result of a thermodynamic non-equilibrium event when the pressure falls below the vapour pressure of the liquid at the prevalent temperature.

Henricks et al. [44] presented an analogy between cavitation and fracture mechanics, proposing that the role impurities play in the formation, concentration and propagation of tensile stresses causing the growth of a crack in solids, embody the same effect as an initial bubble plays in fracturing a fluid and the subsequent growth of a cavitation zone. Photographs were presented to support the thesis between crack propagation in solids and the onset of cavitation in bearings.

Floberg [45-46] found that for a fixed-mass gas bubble in an equilibrium-state condition in a fluid under adiabatic conditions, the fluid pressure is related to the bubble starting equilibrium pressure and surface tension. Floberg showed that expansion will increase the diameter of the bubble as the fluid pressure decreases. (This is an example of pseudo-cavitation since there is no additional gas diffusion or evaporation into the bubble.) Gaseous cavitation begins as the fluid pressure falls below the dissolved gas saturation pressure and the additional mass of non-condensable gases diffuse from the liquid phase into the existing gaseous bubble nucleus. Thus, the nucleus of the gaseous bubble serves as a nucleus for fluid rupture with ensuing ‘cracks’ fueling cavitation through diffusion. Bubble growth due to lowering of fluid pressure without mass addition or due to the lowering of the fluid pressure below the gas saturation pressure are both covered by pseudo- and gaseous cavitation.

Fracture by phase change is represented by vaporous cavitation. This takes place when the pressure of the liquid falls below that saturation pressure at

the current thermodynamic conditions ($T = T_{sat} = f(P_{sat})$. Vaporous cavitation differs from the other cavitation types discussed in the driving force and composition of the bubble within the fluid.

1.3.2 Cavitation Based on Single Phase Reynolds Equation

The discontinuity in the fluid that cavitation creates provides a challenge in the context of a solution to the Reynolds equation. The full Sommerfeld solution allowed for negative pressures, even when the magnitudes were quite large. Gumbel in 1914 was first to account for the film rupture [47]. His theory set the pressure to a constant P_{cav} at a predetermined location near the minimum film thickness and held that pressure for the duration of the divergent region (Figure 1-6a). Gumbel's model is often referred to as the 'half-Sommerfeld' model since there was no effect on the positive pressure side of the bearing. This approach did not account for film reformation nor respect mass continuity but was an important step in recognizing the physics of film rupture.

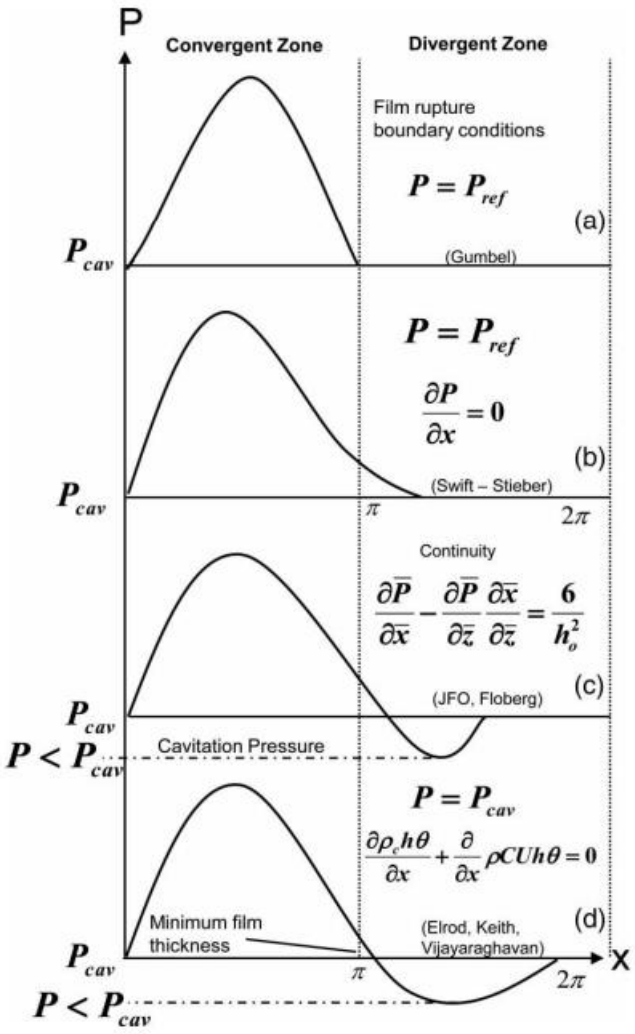

Figure 1-6: Circumferential pressure development based on film rupture theories: (a) Gumbel [45]; (b) Swift-Stieber [46,47]; (c) JFO and Floberg; and (d) Elrod [50], and Vijayaraghavan and Keith [52] figure shared from [41].

Swift and Stieber [48,49] worked independently but arrived at the same conclusion for cavitation formation: a new boundary condition that became known as the Swift-Stieber condition (Figure1-6b). The condition maintains

constant pressure throughout the cavitation zone which does not allow for existence of subcavitational pressures. Brewe et al. [50] cautioned that the Swift-Steiber conditions work reasonably well for the development of the cavitation zone but do not predict the film reformation satisfactorily.

Floberg [51] presented one of the first models that attempted to move away from the Swift-Steiber cavitation model by modelling the formation of cavitation and sub-cavity pressures. The model conserved mass throughout the cavitation zone and postulated the existence of sub-cavity pressures. The Jackson-Floberg-Olsen (JFO) model, figure 1-6c, assumed the flow a striated flow where liquid was transported in-between gas fingers that extended fully across the fluid film clearance. The conservation of mass across the entire bearing based on the Reynolds equation model proved pivotal in the numerical implementation of cavitation.

Elrod [52] provided a numerical contribution that eased implementation of the physical assumptions presented by the JFO model with the use of a flagging system based on a new dimensionless density variable. The flag used with the switch function allowed for the Reynolds equation to be written in terms of the dimensionless density variable and solved with a finite difference method. Vijayaraghavan and Keith [53] further refined the Elrod algorithm for computational efficiency with the same JFO concept with an automatic switch of the scheme dependent on the velocity direction.

1.3.3 Cavitation Based on Two-Phase Homogeneous Navier Stokes

While a single-phase fluid can account for the tensile stress in the fluid, a two-phase fluid promotes accountability for the properties of the ruptured fluid and is more physically accurate. The improvements in computational ability allowed the next step after work on the rupture and reformation of fluid within bearings: the introduction of the Navier-Stokes equations (NS) as a computational engine for the solution of flow in bearings. Finite volume methods allowed for three dimensional computations that accounted for effects of inertia. Singhal et al. [54] proposed a new cavitation model with NS that accounted for gaseous and/or vaporous cavitation in a homogeneous, Newtonian, two-phase mixture. The vaporous cavitation was modelled with a constant bubble density and driven by the pressure differential. The Rayleigh-Plesset equation was used to calculate the temporal change in the bubble radius. The result is the computation of the density for a homogeneous two-phase mixture with small, non-coalesced bubbles dispersed within the liquid. The Rayleigh-Plesset equation, Equation 1.5, is given in terms of those bubble radii. The Rayleigh-Plesset equation was used in conjunction with the Reynolds equation to provide an accurate picture of the two-phase fluid properties at each point during simulation.

$$R\ddot{R} + \frac{3}{2}\dot{R}^2 = \frac{P_R - P_\infty}{\rho_L} \qquad 1.5$$

Zwart et al. [55] independently produced a similar model in commercial software, FLUENT. Density was assumed constant within the bubble and instantaneous mass transfer. This eliminated the need for coupling with an energy equation (for vaporous cavitation) or a diffusion equation (for gaseous cavitation). Zhou [56] applied the Zwart-Gerber-Belamri cavitation model to explore the effect of two-phase flow in squeeze film dampers. Zwart-Gerber-Belarmi presented a CFD methodology for 3D flows with cavitation with mass transfer. The mass transfer used a simplified Rayliegh-Plesset model which appeared as source and sink terms in the liquid and vapor continuity equations [55]. The 3D computation flow dynamic (CFD) analysis demonstrated that the temperature of the oil film was closely related to the oil dynamic viscosity. This started a chain reaction leading to decreased oil-film damping which enlarged the vaporization level and range, as well as how much air was vaporized.

Liu et al. [57] first successfully applied the Reynolds boundary condition to the NS model. In the name of balancing complexity and efficiency, no film reformation was realized in this work. It was given as an alternative to other cavitation models. Hydrodynamic region was similar to previous results but the cavitation region resulted in a constant zero Pascal pressure while the Rayleigh-Plesset model captured the negative pressure in the cavitation zone.

1.3.4 Cavitation based on two-phase homogeneous Reynolds equation

The first homogeneous two-phase lubricating film used with Reynolds equation was in 1982 by Zuber and Dougherty [58]. They started with a modified continuity equation with a source term, $\Gamma_f = \Gamma_f(p,t)$, which represented a constitutive equation of evaporation or condensation [58]. The authors recognized that the success of this model relied on having a proper methodology for obtaining Γ_f , which had little research at the time.

Natsumeda and Someya [59] developed a hydrodynamic theory embodied by a two-phase homogeneous fluid which accounted for sub-cavity pressures preceding the cavitation zone and a generation of void through the Rayleigh-Plesset. This theory was based on experimental results that demonstrated sub-cavity pressures within the bearing by means of a pressure transducer. The calculated void fraction was essentially the previously under-researched Γ_f. The surface dilatational viscosity was included in the Rayleigh-Plesset equation. Many, including Ida et al. [60], Someya [61], and Pierson [62], have since shown the importance of the surface dilatational viscosity in its role in numerical stability and the motion of small bubbles within the fluid. The exclusion of the inertia terms within the Rayleigh-Plesset equation has been shown to be justified through order of magnitude analysis for squeeze film dampers [63] and journal bearings [62].

Snyder [64] and Pierson [62] expanded on the coupling of the Reynolds and Rayleigh-Plesset equations from squeeze film dampers, where most of the work had occurred, to journal bearings. This required the inclusion of void advection. Previously, Natsumeda and Someya [59] and Someya [61] had applied the Reynolds and Rayleigh-Plesset equations to journal bearings but limited their advection to only the circumferential direction and only to one-half of the journal velocity. Snyder and Pierson added full advection (in circumferential and axial directions) and studied results on the variation of surface dilatational viscosity on the extent of the cavitation zone.

The Reynolds-Rayleigh-Plesset cavitation model's numerical stability was assessed and improved by Jaramillo [65, 66]. The suggested improvement increased stability by solving the new radius and surrounding pressure in one step opposed to two steps as was previously done [62, 64].

1.4 Scope of Research

The objectives of this dissertation are grounded in a strong foundation of thermal fluids and numerical methods. They are the following:

1. Develop a self-circulating bearing model to capture the two-dimensional fluid flow within the bearing clearance.
2. Apply a pseudo cavitation model to a self-circulating bearing.

To complete objective one, a closed form analytical solution for the three-dimensional flow within the porous bushing will be coupled with the two-

dimensional Reynolds equation. Validation of this model will be achieved with published experimental air bearings to avoid errors from omitting cavitation. The unique three-dimensional solution for the porous bushing is novel as is its application to a self-circulating bearing.

A previously developed Rayliegh-Plesset-Scriven (RPS) cavitation theory will be coded and applied to the self-circulating bearing case to complete objective two. The cavitation model will be independently validated with published experimental results from a solid bearing. The cavitation model will allow for the calculation of a void fraction used to determine the bulk properties of the two-phase homogeneous fluid. The inclusion of cavitation will provide a more accurate model for improved development of the self-circulating bearing.

1.4.1 Details of Completion

The numerical models were be constructed in MATLAB. The foundation of the behavior of the bearing's fluid film was the Reynolds equation. The two-dimensional equation is a standard throughout the literature for representing journal bearings as unwrapped. The cavitation model was state-of-the-art for models developed from the Rayleigh-Plesset equation. There was literature that based cavitation on the Navier-Stokes equations, but there were limits to the film reformation within that system of equations. The Rayleigh-Plesset-Scriven equation allowed for the modeling of film rupture and reconstruction of a two-phase homogeneous fluid. The Rayleigh-Plesset-Scriven model allowed for an

accurate representation of all forces acting on the bubble, including surface dilatational viscosity.

- Self-Circulating Bearing Porous Bushing Model
  - Review of current porous bushing solutions.
  - Analytical solution for three-dimensional fluid flow within porous bushing.
  - Validation of the porous bushing solution.
  - Evaluate trends of varying bearing parameters on the bearing load capacity.
- Self-Circulating Bearing Pseudo Cavitation Model
  - Review of current cavitation models.
  - Outline homogeneous two-phase fluid cavitation model.
  - MATLAB cavitation model of two-phase fluid for solid bearing.
  - Adapt the pseudo-cavitation model to the self-circulating bearing.
  - Evaluate trends of varying bearing parameters on the bearing load capacity.

1.4.2 Questions Answered

Through completion of the tasks discussed above, answers to the following questions were addressed.

- Does the three-dimensional solution for the porous bushing fluid flow produce a more accurate injection velocity than a linear assumption?

- What permeability ranges for the porous bushing within a self-circulating bearing promote self-circulation? How does changing the permeability parameter affect bearing load capacity?
- How does the thickness of the porous bushing affect bearing load capacity?
- How does the inclusion of pseudo-cavitation affect the outcomes of the self-circulating model?
- Do trends for varying bearing parameters (eccentricity, speed, L/D) change with the inclusion of pseudo cavitation?
- How is the cavitation zone affected by the self-circulation within the bearing?
- Does speed affect the self-circulating bearing's cavitation zone and load capacity?

1.5 Statement of Novelty

The presented work is novel in multiple aspects. A new solution to porous bushing was presented in the literature on porous journal bearings. Applying the porous bushing solution to the self-circulating bearing was a novel addition to the literature, with previous authors using commercial software for self-circulating bearing models. Including the state-of-the-art pseudo-cavitation model in the self-circulating model is another novel addition to the literature on a self-circulating bearing.

CHAPTER II

SELF-CIRCULATING BEARING

2.1 Passive Reservoir

The passive reservoir was represented as a supply pressure surrounding the outer radius of the bushing. The decision for the magnitude of the supply pressure was made based on previous work [67]. Within Balasoiu's dissertation, a deep and shallow reservoir were explored for surrounding the self-circulating bearing. The deep reservoir maintained a nearly constant pressure distribution circumferentially, which decreased slightly with increased speed. The circumferential pressure within the shallow reservoir was sinusoidal and increased somewhat with increased speed. At the start of the experiments [67], a set amount of fluid was deposited within the system. A slight pressure of 13.8 kPa was applied to prevent contact between the shaft and the bushing. That initial pressure was subtracted during analysis of the operating pressure developed within the system. In the conclusions of that work [67], it was noted that for a higher permeability range ($1x10^{-12}\ m^2$ and $1x10^{-11}\ m^2$) that the depth of the reservoir played an essential role in the maximum pressure of the active

space. The active space was effectively enlarged due to the ease of flow between the clearance and the reservoir. However, in low permeability ranges ($1x10^{-12}\ m^2$ and $1x10^{-13}\ m^2$) where the flow was restricted, the depth of the reservoir had less effect.

Early investigations with the model showed that the supply pressure significantly affected the bearing characteristics. The reservoir pressure was held constant for all parameter groups to eliminate the effect of the reservoir behavior on parametric studies. A sample distribution of the supply pressure is included for reference in Figure 2-1 based on Balasiou's work [67].

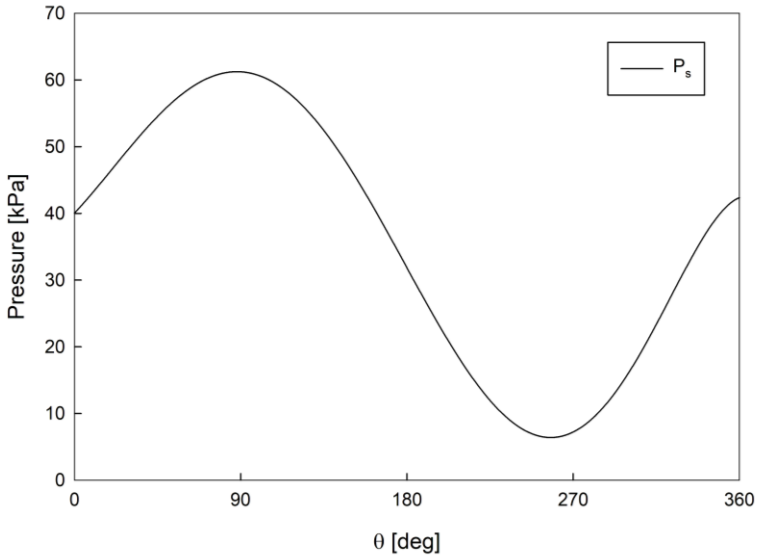

Figure 2-1: Sample supply pressure for self-circulating bearing [65].

2.2 Porous Bushing

The porous bushing pressure, P, was represented by the 3D Laplace equation, which accounted for fluid flow in the axial (z), circumferential (θ), and radial directions (r). The porous bushing permeability was assumed to be constant in all directions and thus was cancelled out of the 3D Laplace equation.

$$\frac{1}{r}\frac{\partial}{\partial r}r\frac{\partial P}{\partial r}+\frac{1}{r^2}\frac{\partial^2 P}{\partial \theta^2}+\frac{\partial^2 P}{\partial z^2}=0 \tag{2.1}$$

The equation's unique closed form solution began with a change of variable that subtracted atmospheric pressure from all pressures to create the working pressure variable. Then, superposition was used to create two problems, each with a homogeneous direction. The homogeneous direction allowed for a Bessel-type solution to each problem. Figure 2-2a represented the first problem in which the supply pressure, P_s, was the original boundary condition at the external bushing radius (R_o) and the inner radius boundary condition set to zero Pa. The inner boundary condition, where pressure at the inner radius, R_i, of the porous bushing was kept and the external radius pressure set to zero Pa.

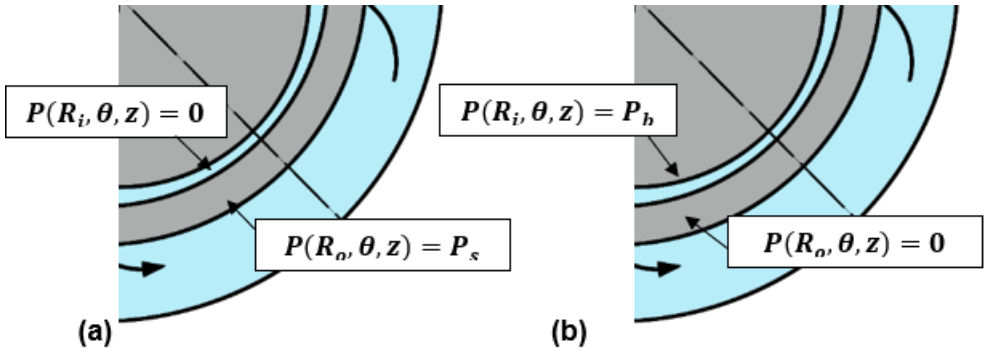

Figure 2-2: Depiction of separated boundary conditions for the closed-form solution representing the porous bushing.

Within each superposition problem (Figure 2-2a and b), a product solution was used to separate the three directions. The details of this work are found in Appendix B. The recomposed expression, Equation 2.2, for the first pressure solution is below where $\lambda_n = \frac{n\pi}{L}$ and L was the bearing's axial length.

$$P_1 = \sum_{n=1}^{\infty} a_{no}\left[I_0(\lambda_n r) - \frac{I_o(\lambda_n R_i)}{K_o(\lambda_n R_i)} K_o(\lambda_n r)\right] \sin(\lambda_n z) + \sum_{n=1}^{\infty}\sum_{m=1}^{\infty} (a_{mn}\cos(m\theta) + b_{nm}\sin(m\theta))[I_\mu(\lambda_n r) - \frac{I_\mu(\lambda_n R_i)}{K_\mu(\lambda_n R_i)} K_\mu(\lambda_n r)] \sin(\lambda_n z) \quad 2.2$$

The first of the three coefficients was defined using the boundary condition, $P(R_o, \theta, z) = P_s$, which represents the passive reservoir surrounding

the porous bushing. Using orthogonality, the double Fourier series was first assumed to be a series in only the circumferential direction. Then, orthogonality was applied in the axial direction over *n* = 1 to infinity. This led to a complete definition for the initial coefficient, as seen below in Equation 2.3.

$$a_{no}\left[I_0(\lambda R_o) - \frac{I_o(\lambda_n R_i)}{K_o(\lambda_n R_i)} K_o(\lambda R_o)\right] = \frac{P_s\left(\frac{-1}{\lambda_n}\right)\cos(\lambda_n z)\,|_0^L}{\int_0^L sin^2(\lambda_n z)dz} = \frac{-2P_s}{\lambda_n L}(\cos(n\pi - 1)) \tag{2.3}$$

The same process with orthogonality in both directions was performed to find that the remaining coefficients, a_{mn} and b_{mn} , for the first pressure solution are equal to zero. The resulting solution for P_1 was Equation 2.4.

$$P_1 = \sum_{n=0}^{\infty} \frac{-2P_s(\cos(n\pi - 1))}{\lambda_n L} \frac{\left[I_0(\lambda r) - \frac{I_o(\lambda_n R_i)}{K_o(\lambda_n R_i)} K_o(\lambda r)\right]}{\left[I_0(\lambda R_o) - \frac{I_o(\lambda_n R_i)}{K_o(\lambda_n R_i)} K_o(\lambda R_o)\right]} sin(\lambda_n z) \tag{2.4}$$

The second superposition was then solved for P_2. Again, separation of variables was used to obtain individual solutions in each direction that were later combined. These equations were the same as in problem one for the axial and circumferential directions since the only difference in boundary conditions occurs

in the radial direction. The radial direction solution for the new boundary condition is below in Equation 2.5.

$$R(r) = E[I_\mu(\lambda_n r) - \frac{I_\mu(\lambda_n R_o)}{K_\mu(\lambda_n R_o)} K_\mu(\lambda_n r)] \quad 2.5$$

Again, the solutions for each direction were multiplied, resulting in many coefficients that were combined to form three final coefficients: $a_{no}, a_{mn}, \text{and } b_{nm}$.

$$\begin{aligned} P_2 = \sum_{n=1}^{\infty} a_{no} \left[I_0(\lambda_n r) - \frac{I_o(\lambda_n R_o)}{K_o(\lambda_n R_o)} K_o(\lambda_n r) \right] \sin(\lambda_n z) \\ + \sum_{n=1}^{\infty} \sum_{m=1}^{\infty} (a_{mn} \cos(m\theta) + b_{nm} \sin(m\theta)) [I_\mu(\lambda_n r) \\ - \frac{I_\mu(\lambda_n R_o)}{K_\mu(\lambda_n R_o)} K_\mu(\lambda_n r)] \sin(\lambda_n z) \end{aligned} \quad 2.6$$

The last boundary condition, $P_2(r = R_i, \theta, z) = P_b$, was used to solve for the coefficients. Orthogonality was applied in both the axial and circumferential directions. The expressions greatly simplify if orthogonality of trigonometric functions with integer arguments can be used. Thus, the value of omega was limited to being equal to one in the formation of the Fourier fit. This also introduces another simplification in terms of the infinite series; since there are integer arguments, the only nonzero terms will be produced when $m\varphi = iw\varphi$. The Fourier series is limited to 8 terms (MATLAB), so the infinite series will also be limited to *m = 8*. All terms after this would be equal to zero since θ is equal

and iw has a maximum value of 8. The Fourier series at each axial location for the circumferential pressure was given by Equation 2.7.

$$P_b(\theta) = f_0 + \sum_{k=1}^{8} f_k \cos(k\omega\theta) + g_k \sin(k\omega\theta) \tag{2.7}$$

The first constant defined is when *m = 0*, Equation 2.8.

$$\left[I_\mu(\lambda_n R_i) - \frac{I_\mu(\lambda_n R_o)}{K_\mu(\lambda_n R_o)} K_\mu(\lambda_n R_i)\right] a_{no} \sin \lambda_n z \int_0^{2\pi} \cos m\theta \, \mathrm{d}\theta = \int_0^{2\pi} P_b(\theta, z) \cos(m\theta) \, \mathrm{d}\theta \tag{2.8}$$

After the pressure at the outside radius is set equal to the bearing pressure, each side is multiplied by $\cos m\theta$ and integrated from 0 to 2π. The integral of the bearing pressure can be expanded for each of the types of Fourier terms as the following.

$$\int_0^{2\pi} P_b(\theta) \, \mathrm{d}\theta = \int_0^{2\pi} f_0 \, \mathrm{d}\theta + \int_0^{2\pi} f_k \cos(k\omega x) \, \mathrm{d}\theta + \int_0^{2\pi} g_k \sin(k\omega x) \, \mathrm{d}\theta \tag{2.9}$$

$$\int_0^{2\pi} P_b(\theta) \, \mathrm{d}\theta = 2\pi \left(\sum_{k=0}^{8} f_k + \sum_{k=1}^{8} g_k \right) \tag{2.10}$$

Orthogonality in the axial direction continues:

$$a_{no}[I_\mu(\lambda_n R_i) - \frac{I_\mu(\lambda_n R_o)}{K_\mu(\lambda_n R_o)} K_\mu(\lambda_n R_i)] \int_0^L sin^2(\lambda_n z)\,\mathrm{d}z$$

$$= \int_0^L 2\pi \left(\sum_{k=0}^{8} f_k + \sum_{k=1}^{8} g_k \right) sin(\lambda_n z)\, dz \qquad 2.11$$

This leads to the final expression for a_{no} as Equation 2.12 where the summations represent the multiple terms from the Fourier series.

$$a_{no} = \frac{2}{L} \frac{\int_0^L (\sum_{k=0}^{8} f_k + \sum_{k=1}^{8} g_k)\, sin(\lambda_n z)\, dz}{[I_\mu(\lambda_n R_i) - \frac{I_\mu(\lambda_n R_o)}{K_\mu(\lambda_n R_o)} K_\mu(\lambda_n R_i)]} \qquad 2.12$$

The integral is integrated using the trapezoid method. Each axial location will have different coefficients (from the piecewise Fourier curve fit at each axial location representing P_b).

The second constant solved for, a_{mn}, also used the orthogonality properties for trigonometric functions in both the circumferential and axial direction. The boundary condition has been applied at the bearing-porous interface, and both sides have been multiplied by $cos\, m\theta$ and integrated from 0 to 2π.

$$\int_0^{2\pi} P_b(\theta, z)\, cos(m\theta)\, \mathrm{d}\theta$$

$$= \sum_{n=1}^{\infty} a_{mn}[I_\mu(\lambda_n R_i) - \frac{I_\mu(\lambda_n R_o)}{K_\mu(\lambda_n R_o)} K_\mu(\lambda_n R_i)]\, sin(\lambda_n z) \int_0^{2\pi} cos^2(m\theta)\, \mathrm{d}\theta \tag{2.13}$$

For the case when the arguments are equal, orthogonality in the axial direction is applied next. This results in multiplication by $\int_0^L sin(\lambda_n z)\, dz$ on both sides.

$$a_{nm}[I_\mu(\lambda_n R_i) - \frac{I_\mu(\lambda_n R_o)}{K_\mu(\lambda_n R_o)} K_\mu(\lambda_n R_i)] \int_0^L sin(\lambda_n z)\, \mathrm{d}z = \frac{1}{\pi} \int_0^L f_k \pi\, sin(\lambda_n z)\, \mathrm{d}z \tag{2.14}$$

The integral from zero to *L* is evaluated for each term of the Fourier series remaining from orthogonality in the circumferential direction, represented by f_k.

$$a_{nm} = \frac{2}{L} \frac{1}{[I_\mu(\lambda_n R_i) - \frac{I_\mu(\lambda_n R_o)}{K_\mu(\lambda_n R_o)} K_\mu(\lambda_n R_i)]} \int_0^L f_k\, sin(\lambda_n z)\, \mathrm{d}z \tag{2.15}$$

Equation 2.15 is the final expression for a_{nm}. Constant b_{nm} is solved for using the same methods as a_{nm}.

$$\int_0^{2\pi} P_b(\theta, z)\, sin(m\theta)\, \mathrm{d}\theta$$

$$= \sum_{n=1}^{\infty} b_{nm}[I_\mu(\lambda_n R_i) - \frac{I_\mu(\lambda_n R_o)}{K_\mu(\lambda_n R_o)} K_\mu(\lambda_n R_i)]\, sin(\lambda_n z) \int_0^{2\pi} sin^2(m\theta)\, \mathrm{d}\theta \qquad 2.16$$

Expansion of the left-hand side integral is shown for each type of term in the Fourier series.

$$\int_0^{2\pi} P_b(\theta, z)\, sin(m\theta)\, \mathrm{d}\theta$$

$$= \int_0^{2\pi} f_0\, sin(m\theta)\, \mathrm{d}\theta + \int_0^{2\pi} f_k\, cos(k\omega\theta)\, sin(m\theta)\, \mathrm{d}\theta + \int_0^{2\pi} g_k sin(\mathrm{k}\omega\theta) sin(m\theta)\, \mathrm{d}\theta \qquad 2.17$$

Again, using trigonometric orthogonality, the second integral equals zero since arguments have been limited to integers, and the first integral is always zero. The third integral is only non-zero when the arguments are equal.

If the arguments are equal, the next step in solving for b_{mn} is to use orthogonality in the axial direction.

$$b_{mn}[I_\mu(\lambda_n R_i) - \frac{I_\mu(\lambda_n R_o)}{K_\mu(\lambda_n R_o)} K_\mu(\lambda_n R_i)] \int_0^L sin^2\, \lambda_n z \, \mathrm{d}z = \frac{1}{\pi} \int_0^L P_b(z)\, sin(\lambda_n z)\, \mathrm{d}z \tag{2.18}$$

The final expression for b_{nm} is expressed in Equation 2.19. The integral from zero to *L* is evaluated for each term of the Fourier series remaining from orthogonality in the circumferential direction, represented by g_k.

$$b_{nm} = \frac{2}{L} \frac{1}{[I_\mu(\lambda_n R_i) - \frac{I_\mu(\lambda_n R_o)}{K_\mu(\lambda_n R_o)} K_\mu(\lambda_n R_i)]} \int_0^L g_k\, sin(\lambda_n z)\, \mathrm{d}z \tag{2.19}$$

The resulting closed-form solution for the pressure within the porous bushing is shown below by adding P_1 and P_2 in Equation 2.20.

$$P(r,\theta,z)$$

$$= \sum_{n=0}^{\infty} \frac{-2P_s(\cos(n\pi - 1))}{\lambda_n L} \frac{\left[I_0(\lambda_n r) - \frac{I_o(\lambda_n R_i)}{K_o(\lambda_n R_i)} K_o(\lambda_n r)\right]}{\left[I_0(\lambda_n R_o) - \frac{I_o(\lambda_n R_i)}{K_o(\lambda_n R_i)} K_o(\lambda_n R_o)\right]} sin(\lambda_n z)$$

$$+ \sum_{n=1}^{\infty} a_{no} \left[I_0(\lambda_n r) - \frac{I_o(\lambda_n R_o)}{K_o(\lambda_n R_o)} K_o(\lambda_n r)\right] \sin(\lambda_n z) \qquad 2.20$$

$$+ \sum_{n=1}^{\infty} \sum_{m=1}^{\infty} (a_{mn} \cos(m\theta) + b_{nm} \sin(m\theta))[I_\mu(\lambda r)$$

$$- \frac{I_\mu(\lambda_n R_o)}{K_\mu(\lambda_n R_o)} K_\mu(\lambda_n r)] \sin(\lambda_n z)$$

Where,

$$a_{no} = \frac{1}{\pi L} \frac{\int_0^L (\sum_{k=0}^{8} f_k + \sum_{k=1}^{8} g_k)\, sin(\lambda_n z)\, dz}{[I_\mu(\lambda_n R_i) - \frac{I_\mu(\lambda_n R_o)}{K_\mu(\lambda_n R_o)} K_\mu(\lambda_n R_i)]} \qquad 2.20a$$

$$a_{nm} = \frac{2}{L} \frac{\int_0^L f_k\, sin(\lambda_n z)\, \mathrm{d}z}{[I_\mu(\lambda_n R_i) - \frac{I_\mu(\lambda_n R_o)}{K_\mu(\lambda_n R_o)} K_\mu(\lambda_n R_i)]} \qquad 2.20b$$

$$b_{nm} = \frac{2}{L} \frac{\int_0^L g_k\, sin(\lambda_n z)\, \mathrm{d}z}{[I_\mu(\lambda_n R_i) - \frac{I_\mu(\lambda_n R_o)}{K_\mu(\lambda_n R_o)} K_\mu(\lambda_n R_i)]} \qquad 2.20c$$

2.2.1 Representation of the fluid film pressure for use by the porous bushing solution

The accuracy of the injection velocity is affected by the equation used (Darcy), the accuracy of the pressure differential (discussed in Chapter 4), and the accuracy of the bearing pressure representation within the closed-form solution. The Curve Fitting Toolbox™ from MATLAB was used to determine the most accurate and efficient fit for the bearing pressure.

An exponential equation that is a function of both θ and z can be used to describe the entire pressure distribution if the eccentricity is of 0.3 or lower. This saves computational time. However, if a piecewise Fourier series is used instead, all eccentricities can be represented by one curve fit. The Fourier series equations sufficiently (r-squared value of at least 0.95) described the pressure in the bearing film. Each axial location used an eight-term Fourier series, Equation 2.21, to handle the nonlinearity at the cavitation point within the pressure distribution.

$$P = a_0 + \sum_{k=1}^{8} a_k \cos(kwx) + b_k \sin(kwx) \qquad 2.21$$

The coefficients within this Fourier series approximation of the pressure were stored in a coefficient matrix. The coefficients were then called upon within the closed form solution to calculate the pressure at each axial location.

The flow chart in Figure 2-3 below outlines the steps to calculate the injection velocity for one point in the 3D porous matrix. The simulation begins with the Reynolds equation to find the converged bearing pressure. This pressure was then transformed into a matrix of coefficients through MATLAB's Curve Fitting Toolbox™, which was used in each of the separated solutions, P_1 and P_2, which combined to form the pressure distribution within the bushing. This pressure distribution provides the radial differential used in Darcy's law in the Reynolds equation that starts the next global iteration.

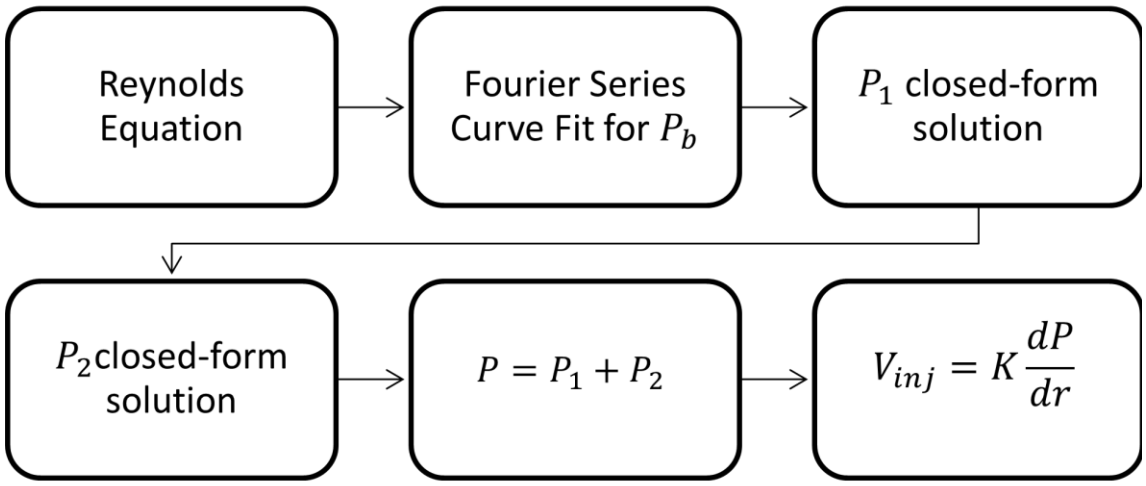

Figure 2-3: Flowchart for calculating injection velocity for a single grid point.

The numerical flowchart shows that the injection velocity calculated from the porous media is then used to find the new pressure in the modified Reynolds equation. This process continues until the pressure distribution from the modified

Reynolds equation is less than 1% different than the previous iteration post-porous medium.

2.2.2 Validation of the porous bushing solution

The analytical solution for the porous bushing was validated against published work on porous air journal bearings. This selection prevented errors from cavitation assumptions required in a fluid porous journal bearing. The same supply pressure and ideal gas assumptions for the air were used. Deviations between the models were attributed to differing axial boundary conditions. The current work used a Dirichlet boundary approach condition in which the axial edges of the bearing were equal to atmospheric pressure. In contrast, the referenced work set the axial direction pressure gradient equal to zero. The Dirichlet boundary condition was more realistic as it allowed for side leakage, which is highly probable in a self-circulating bearing.

The x-axis in Figure 2-4 is the feeding parameter, a common dimensionless term within literature defined as a ratio of the permeability and geometry factors of the bearing. Equation 2.22 uses the bearing permeability, *K*, the shaft radius, r, the bearing clearance, c, and the porous medium thickness, *H*.

$$\lambda = \frac{12Kr^2}{c^3 H} \tag{2.22}$$

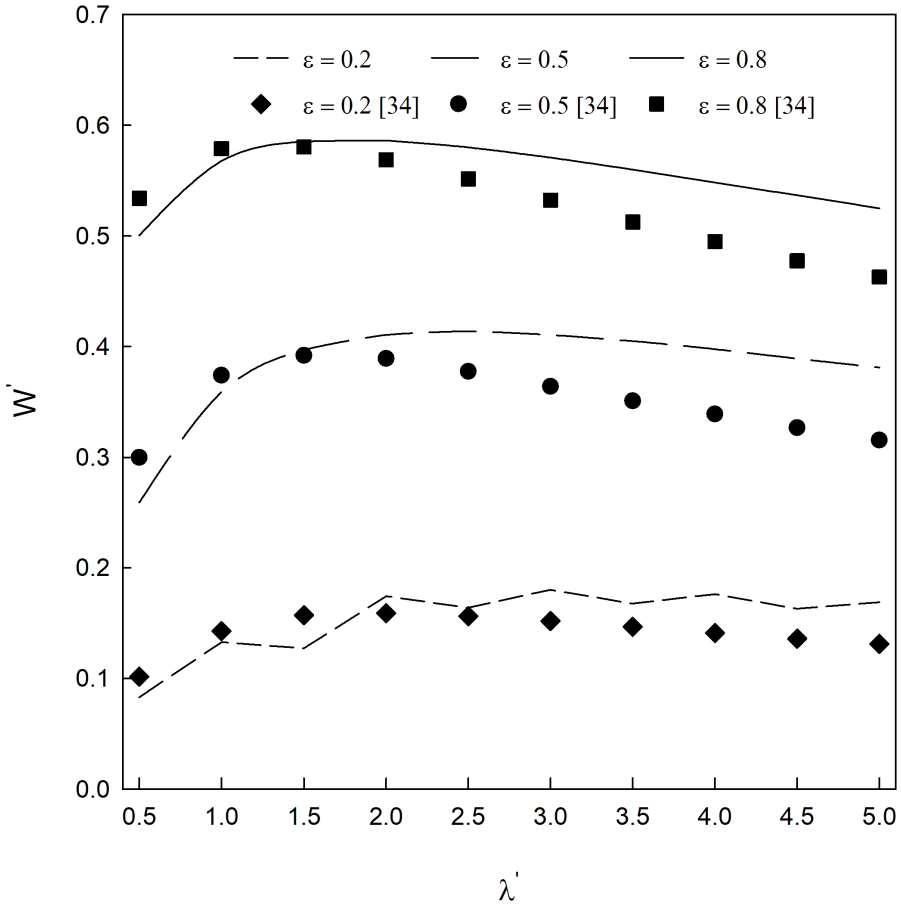

Figure 2-4: Validation of Porous Model with Madjumar [34].

2.3 Fluid film representation

The Reynolds equation represented the fluid film; the mathematical details are found in Appendix A. A finite element approach was employed to assess the forces present within the fluid film of the bearing. There were nine initial assumptions used to formulate the Reynolds equation which were outlined

below. A foundational assumption in the formation of this approach is that the fluid film thickness is relatively small compared with the width and circumference of the bearing (1). This assumption let to the following assumptions:

- (2) The viscosity and the pressure were constant across the film, commonly referred to as a lumped condition in the radial direction.
- (3) All rotational motion can be approximated with translational motion.
- (4) The curvature of the bearing can be neglected.

The last of these assumptions allowed for the bearing to be analyzed as 'unwrapped,' meaning that the curvature of the surfaces were ignored and the bearing represented as two surfaces inclined to each other. The small film thickness was assumed to result in a Reynold's number in the laminar region, which was later confirmed with the numerical settings used (5).

Newton's second law applied to the fluid element in the circumferential and axial directions was simplified by neglecting inertia forces due to their small magnitude in comparison to the viscous forces and pressure induced forces (6). This assumption in addition to the fluid being Newtonian, which allowed for substitution of the fluid's viscosity, μ, in place of the shear term, τ_x, (7), led to Equations 2.23 and 2.24 which were used to define the circumferential and axial velocities (u and v respectively).

$$\frac{\partial P}{\partial x} = \frac{\partial \tau_x}{\partial y} = \mu \frac{\partial^2 u}{\partial y^2} \quad 2.23$$

$$\frac{\partial P}{\partial z} = \frac{\partial \tau_x}{\partial y} = \mu \frac{\partial^2 v}{\partial y^2} \quad 2.24$$

Viscosity was assumed constant across the fluid film while the expressions above were integrated across the fluid to determine the velocity's definition.

$$u = \frac{1}{2\mu}\frac{\partial P}{\partial x} z^2 + c_1 z + c_2 \quad 2.25$$

$$v = \frac{1}{2\mu}\frac{\partial P}{\partial y} z^2 + c_3 z + c_4 \quad 2.26$$

The velocity in the circumferential direction accounted for both Poiseuille and Couette flow, while the axial direction only had Poiseuille effects. The boundary conditions at the boundaries of the fluid film demonstrated the movement of the top and bottom surface and the constant length of the bearing. Thus, the fully defined velocities for a fluid film with applied boundary conditions were represented by Equations 2.27 and 2.28 which used h as the fluid film thickness, U_1 as the velocity of the bushing in the x-direction, and U_2 as the velocity of the shaft in the x-direction.

$$u = \frac{1}{2\mu}\frac{\partial P}{\partial x} z(z-h) + \frac{h-z}{h} U_1 + \frac{z}{h} U_2 \quad 2.27$$

$$v = \frac{1}{2\mu}\frac{\partial P}{\partial y}z(z-h) \tag{2.28}$$

The continuity equation was utilized to look at mass conservation. It is assumed that the density of the fluid does not change with time (8). The expressions for velocity are used in addition to boundary conditions so that there was no fluid lost to the journal and there was an injection velocity from the bushing. Leibnitz's rule was used to perform the integration, which resulted in Equation 2.28 where $V_1 \text{ and } V_2$ represented the velocity normal to the shaft and bushing surface. A no-slip boundary condition was assumed at both fluid-solid interfaces (9).

$$h\frac{\partial \rho}{\partial t} + \frac{\partial}{\partial x}\left(\frac{-\rho h^3}{12\mu}\frac{\partial P}{\partial x} + \frac{\rho h}{2}U_1 + \frac{\rho h}{2}U_2\right) - \rho U_2\frac{dh}{dx} + \frac{\partial}{\partial y}\left(\frac{-\rho h^3}{12\mu}\frac{\partial P}{\partial y}\right) + \rho V_2 - \rho V_1 = 0 \tag{2.28}$$

This equation is more commonly seen as follows,

$$\frac{\partial}{\partial x}\left(\frac{\rho h^3}{12\mu}\frac{\partial P}{\partial x}\right) + \frac{\partial}{\partial y}\left(\frac{\rho h^3}{12\mu}\frac{\partial P}{\partial y}\right) = h\frac{\partial \rho}{\partial t} + \frac{\partial}{\partial x}\left(\rho h\frac{U_1 + U_2}{2}\right) - \rho U_2\frac{dh}{dx} + \rho V_2 - \rho V_{inj} \tag{2.29}$$

For specific application to a journal bearing, the velocities were adjusted to account for the rotational velocity and the shaft motion. The details of the

modification are found in Appendix A. The small angle of the tangential velocity allows the cosine of the angle to be approximated as one. It was assumed that the bushing does not have motion, making $U_2 = 0$ and $U_1 = U$. The Reynolds equation for a solid bearing accounting for the velocity assumptions was represented in Equation 2.30 where V_{inj} is the injection velocity of fluid into the clearance and ρ is the density of the fluid.

$$\frac{\partial}{\partial x}\left(\frac{\rho h^3}{12\mu}\frac{\partial P}{\partial x}\right) + \frac{\partial}{\partial y}\left(\frac{\rho h^3}{12\mu}\frac{\partial P}{\partial y}\right) = \frac{\partial(\rho h)}{\partial t} + \frac{\partial}{\partial x}\left(\frac{\rho h U}{2}\right) - \rho V_{inj} \tag{2.30}$$

Neglecting the fluid inertia drove the decision to use Darcy's law to represent the injection velocity of fluid from the porous bushing into the fluid film. The pressure solution of the porous bushing was used to calculate the change in pressure across the radius of the bushing, which, along with the permeability of the bushing and viscosity of the fluid, determined the injection velocity from the porous bushing.

$$V_{inj} = \frac{-dP}{dr}\frac{K}{\mu} \tag{2.31}$$

The complete Reynolds equation used within the self-circulating bearing of this work is given in Equation 2.32, where the injection velocity from the porous bushing is included, and a no-slip boundary condition between the fluid film and the journal was assumed.

$$\frac{\partial}{\partial x}\left(\frac{\rho h^3}{12\mu}\frac{\partial P}{\partial x}\right)+\frac{\partial}{\partial y}\left(\frac{\rho h^3}{12\mu}\frac{\partial P}{\partial y}\right)=\frac{\partial(\rho h)}{\partial t}+\frac{\partial}{\partial x}\left(\frac{\rho h U}{2}\right)+\rho\frac{dP}{dr}\frac{K}{\mu} \quad 2.32$$

2.3.1 Numerical solution of the Reynolds equation

The numerical solution of the Reynolds equation started with a simplification of constants for each iteration, $M=\frac{\rho h^3}{12\mu}$.

$$M\frac{\partial^2 P}{\partial x^2}+M\frac{\partial^2 P}{\partial y^2}+\frac{\partial M}{\partial x}\left(\frac{\partial P}{\partial x}\right)+\frac{\partial M}{\partial y}\left(\frac{\partial P}{\partial y}\right)=\frac{U}{2}\frac{\partial(\rho h)}{\partial x}+\frac{\partial(\rho h)}{\partial t} \quad 2.33$$

Each second-order derivative was numerically expanded using a second-order central method. The first order in time used a forward discretization, and the first order in space used a central discretization.

$$\begin{aligned} M_{i,j}^{n+1}\frac{P_{i+1,j}^{n+1}-2P_{i,j}^{n+1}+P_{i-1,j}^{n+1}}{(\Delta x)^2}+M_{i,j}^{n+1}\frac{P_{i,j+1}^{n}-2P_{i,j}^{n+1}+P_{i,j-1}^{n+1}}{(\Delta y)^2} \\ +\frac{M_{i+1,j}^{n+1}-M_{i-1,j}^{n+1}}{\Delta x}\frac{P_{i+1,j}^{n+1}-P_{i-1,j}^{n+1}}{\Delta x} \\ +\frac{M_{i,j+1}^{n+1}-M_{i,j-1}^{n+1}}{\Delta \mathrm{y}}\frac{P_{i,j+1}^{n}-P_{i,j-1}^{n+1}}{\Delta y} \\ =\frac{U}{2}\frac{(\rho h)_{i+1,j}^{n+1}-(\rho h)_{i-1,j}^{n+1}}{\Delta x}+\frac{(\rho h)_{i,j}^{n+1}-(\rho h)_{i,j}^{n}}{\Delta t} \end{aligned} \quad 2.34$$

The terms were then grouped based on the pressure coefficient, which leads to the tridiagonal form shown in Equation 2.35; the coefficients are defined in Equations 2.36-2.39 below.

$$A_{i,j}P_{i-1,j} + B_{i,j}P_{i,j} + C_{i,j}P_{i+1,j} = D_{i,j} \tag{2.35}$$

$$A_{i,j} = \frac{M_{i,j}^{n+1}}{(\Delta x)^2} - \frac{M_{i+1,j}^{n+1} - M_{i-1,j}^{n+1}}{4(\Delta x)^2} \tag{2.36}$$

$$B_{i,j} = \frac{-2M_{i,j}^{n+1}}{\Delta x} - \frac{-2M_{i,j}^{n+1}}{\Delta y} \tag{2.37}$$

$$C_{i,j} = \frac{M_{i,j}^{n+1}}{(\Delta x)^2} + \frac{M_{i+1,j}^{n+1} - M_{i-1,j}^{n+1}}{4(\Delta x)^2} \tag{2.38}$$

$$D_{i,j} = \frac{U}{2}\frac{(\rho h)_{i+1,j}^{n+1} - (\rho h)_{i-1,j}^{n+1}}{2\Delta x} + \frac{(\rho h)_{i,j}^{n+1} - (\rho h)_{i,j}^{n}}{\Delta t} - P_{i,j+1}^{n}\left(\frac{M_{i,j}^{n+1}}{(\Delta y)^2} + \frac{M_{i,j+1}^{n+1} - M_{i,j-1}^{n+1}}{4(\Delta y)^2}\right) \tag{2.39}$$

Periodic boundary conditions in the circumferential direction were applied (Equation 2.40). Numerically, these conditions resulted in Equation 2.41 when a forward discretization was used at the end derivative and the backward discretization was applied at the zero position.

$$\left(\frac{\partial P}{\partial x}\right)_0 = \left(\frac{\partial P}{\partial x}\right)_{2\pi};\ \ P_0 = P_{2\pi} \tag{2.40}$$

$$0.5\left(P_{2,j} + P_{N_x-1,j}\right) - P_{N_x,j} = 0;\ \ P_1 - P_{N_x,j} = 0 \tag{2.41}$$

The axial boundary conditions were applied in Dirichlet form outside of the matrix. The tridiagonal matrix is solved in implicit form, where the updated pressure values are used within the solution as it progresses. The matrix does

not solve the axial ends of the bearing; these are reserved for the Dirichlet boundary condition, which in this case is pressure equal to atmospheric pressure.

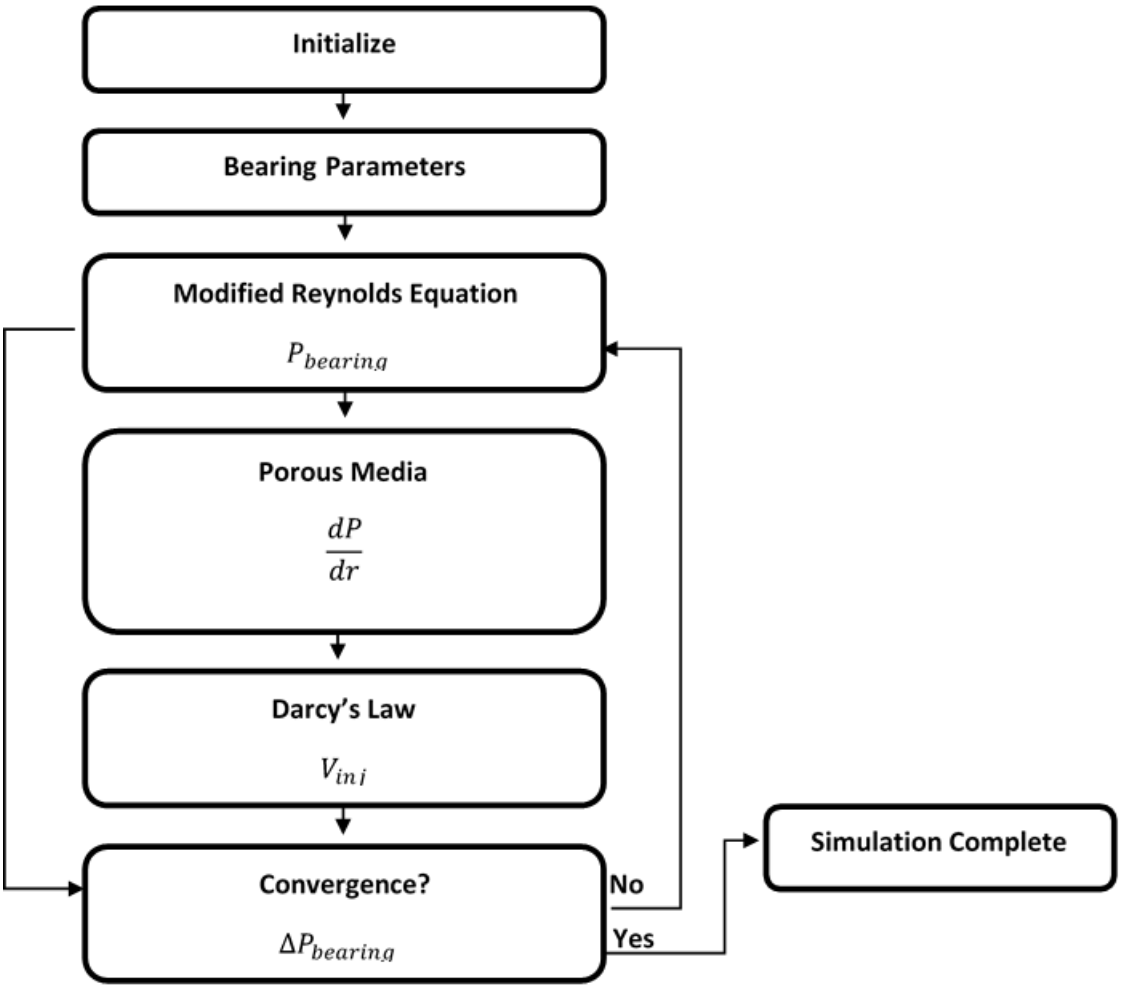

Figure 2-5: Numerical flowchart for a self-circulating journal bearing with Gumbel cavitation.

The numerical flowchart, Figure 2-5, describes the calculation process for the pressure within the fluid film when Gumbel cavitation is applied. The user

defined bearing parameters, and the fluid film's pressure was initialized as atmospheric. The implicit solution of the tridiagonal matrix was executed, and the pressure was used as the boundary condition for the porous bushing pressure solution. Once the porous bushing pressure field was defined, the injection velocity was calculated for each point in the fluid film. The injection velocity was utilized in the next iteration of the tridiagonal matrix solution. Before the next iteration of the Reynolds equation, the convergence on the pressure field was evaluated through comparison of the current fluid film pressure and the previous iteration's fluid film pressure.

2.4 Analysis Parameters

A few common values used for comparison of bearing performance were used in the results section. The first is the bearing load capacity, a function of the fluid film pressure. The bearing load capacity in the radial and tangential direction (w_r and w_t respectively) were determined with Equations 2.42 and 2.43. These were combined to give the overall bearing load capacity.

$$w_t = \int_0^L \int_0^{2\pi} P\, R cos(\theta) d\theta dz \tag{2.42}$$

$$w_r = \int_0^L \int_0^{2\pi} P\, R sin(\theta) d\theta dz \tag{2.43}$$

$$w = \sqrt{{w_t}^2 + {w_r}^2} \tag{2.44}$$

The tangential and radial components of the load were used to calculate the steady-state angle of the line of centers from the bearing's positive x-axis. The attitude angle, ϕ, indicated the bearing's stability (Equation 2.45). A larger attitude angle represents a larger difference between these forces which would result in instability of the journal. More in-depth investigations into the rotordynamics of journal bearings support that there is increased stability from a lower attitude angle [62].

$$\phi = \tan^{-1}(-\frac{w_r}{w_t}) \quad 2.45$$

While the load capacity and attitude angle were results of the behavior of the bearing, the final parameter needed for results analysis was a result of the inputs to the model. The Reynolds number for bearings was based on the bearing concentric clearance. Equation 2.46 demonstrated the calculation using the lubricant density,(ρ), rotational speed(ω), shaft radius(r), clearance(c), and lubricant viscosity, μ.

$$Re_c = \frac{\rho(\omega r)c}{\mu} \quad 2.46$$

CHAPTER III

CAVITATION DEVELOPMENT

3.1 Gumbel Cavitation

Gumbel cavitation was a preliminary cavitation model that does not permit negative pressure, or tensile stresses, within the fluid. All negative pressure were set to equal atmospheric pressure for the film rupture region. For initial renditions of the self-circulating bearing, the Gumbel cavitation model was used.

3.2 Rayleigh-Plesset Equation

The Rayleigh-Plesset equation was used to represent the growth and decay of bubbles within the two-phase fluid film. The derivation of the Rayleigh-Plesset equation came from the conservation of mass and momentum within the radial flow of incompressible, Newtonian liquid. This representation of cavitation did not account for evaporation or condensation, only what is considered pseudo-cavitation. The initialization of the fluid placed bubble nuclei within each computational cell, with the ambient temperature and pressure of the computation cell.

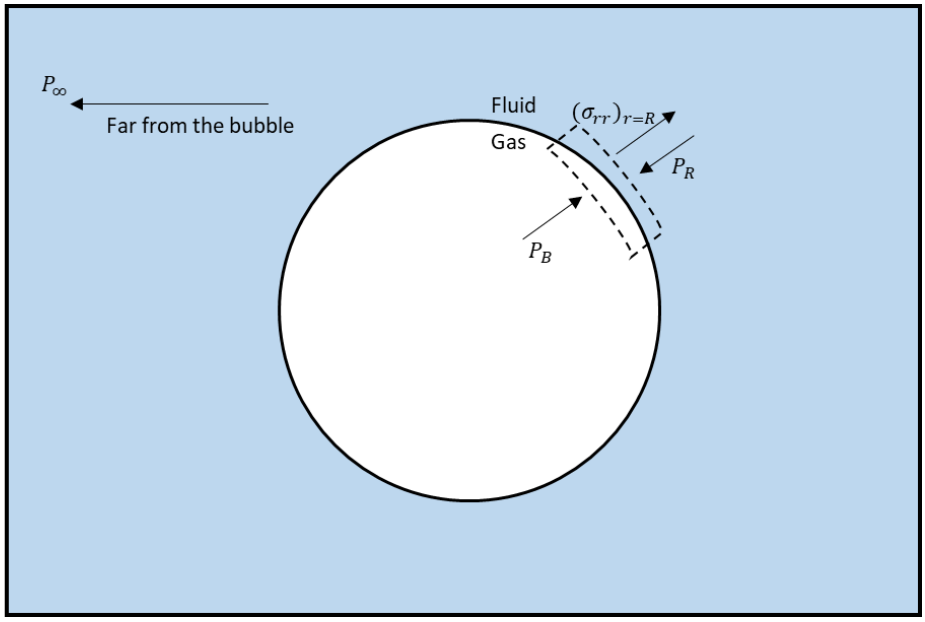

Figure 3-1: The spherical Rayleigh bubble within an infinite liquid.

In Figure 3-1, r was the radial coordinate, R was the radius of the bubble, P_R was the pressure of the liquid just outside the bubble, P_∞ was the pressure of the liquid far from the bubble, P_B was the pressure of the gas within the bubble, P was the pressure of the liquid as a function of the radial coordinate and u the radially outward velocity. The representation of the bubble within the "infinite" lubricant surrounding it set the stage for bubble growth/decay.

$$R\ddot{R} + \frac{3}{2}\dot{R}^2 = \frac{P_R - P_\infty}{\rho_L} \qquad 1.5$$

The Rayleigh bubble dynamics equation was given by Equation 1.5, where P_R is the pressure at the outer radius of the bubble. There was a need to relate the pressure just outside the bubble and the pressure within the bubble, which was done by including the stress at the bubble's surface in Equation 3.1 and Figure 3.2. The stresses which made up $(\sigma_{rr})_{r=R}$ are surface tension, $\sigma_{T,R}$, and dynamic viscosity, $\sigma_{\mu,R}$, terms. The pressure inside the bubble was related to the pressure outside the bubble by Equation 3.1.

$$P_B + (\sigma_{rr})_{r=R} - P_R = 0 \qquad 3.1$$

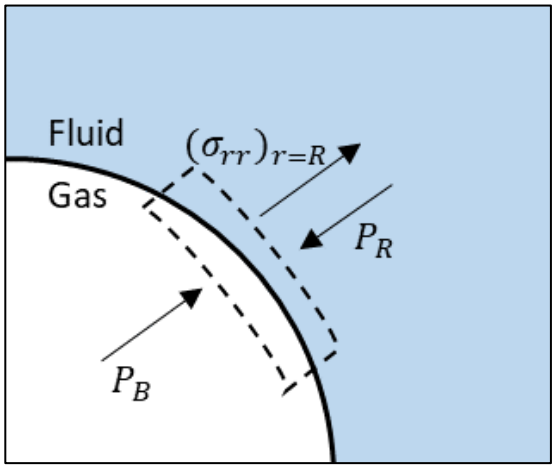

Figure 3-2: Pressure inside and immediately outside the bubble and the stress acting on the surface. The dotted line shows the control surface.

The stresses that made up the bubble surface stress required further investigation. The dynamic viscosity term was first included in the bubble

dynamic equation by Poritsky [68], who noted that “while it is true that the effect of viscosity vanishes in the equations of motion so that the resultant of the viscosity stresses vanish, this is not necessarily the case with the stresses themselves”. The viscous stress acting in the radial direction at any point in the liquid was defined by the viscous stress tensor in the radial direction, $\sigma_{rr,visc} = 2\mu\frac{\partial u}{\partial r}$. The viscous stress tensor, $\sigma_{rr,visc} = 2\mu\frac{\partial u}{\partial r}$, defined the viscous stress acting in the radial direction at any point in the fluid; this required computation of the velocity of the fluid at the surface of the bubble. In the derivation of the Rayleigh equation, the velocity of the liquid is defined by Equation 3.2.

$$u = \frac{R^2}{r^2}\dot{R} \tag{3.2}$$

Executing the derivative in the stress tensor for the radial direction and setting the value of r to the bubble’s radius R, yields the viscous component of the surface stresses, $\sigma_{\mu,R}$, in Equation 3.3.

$$\sigma_{\mu,R} = -\frac{4\mu_L}{R}\dot{R} \tag{3.3}$$

The inclusion of the surface tension term was first accomplished by Plesset in his study on the dynamics of cavitation bubbles [69]. The surface tension component of the radial stress $(\sigma_{rr})_{r=R}$ is written below in Equation 3.4.

$$\sigma_{T,R} = -\frac{2T}{R} \tag{3.4}$$

In equation 3.4, *T* is the surface tension of the bubble. The inclusion of static tension in the Rayleigh equation resulted in the well-known Rayleigh-Plesset equation. The inclusion of the dynamic portion of surface tension, known as surface dilatation, was first introduced by Scriven [68] and is the bubble surface's resistance to changing shape. The magnitude of this resistance was inverse to the surface area and thus grew larger as the bubble became smaller. The surface tension term, including static surface tension and surface dilatation, was defined by Equation 3.5 where γ is static surface tension, κ^s is surface dilatational viscosity, and *A* is the area of the surface of the bubble [70]. The surface dilation term served as a damper to the bubble changing shape because of the stress it exercised on the bubble's surface.

$$T = \gamma + \kappa^s \frac{1}{A}\frac{dA}{dt} = \gamma + \frac{2\kappa^s}{R^2}\dot{R} \tag{3.5}$$

Rewriting Equation 3.5 in terms of bubble radius and replacing surface tension *T* with both its static and dynamic components resulted in the full expression for the bubble's surface tension, Equation 3.6.

$$\sigma_{T,R} = -\frac{2\gamma}{R} - \frac{4\kappa^s}{R^2}\dot{R} \tag{3.6}$$

Equations 3.5 and 3.6 provide the fully defined relationship between P_R and P_B in Equation 3.7. Figure 3.3 shows the pressures and stresses acting on the bubble's surface.

$$P_R = P_B - 4\frac{\mu_L \dot{R}}{R} - \frac{2\gamma}{R} - \frac{4\kappa^s \dot{R}}{R^2} \tag{3.7}$$

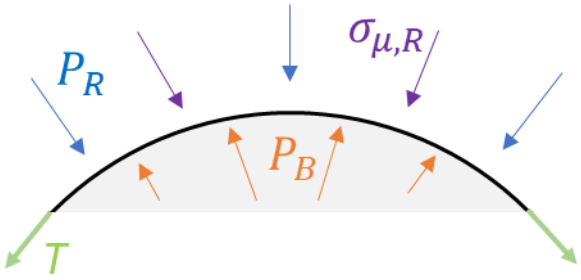

Figure 3-3: Pressures and surface stress for the surface of a spherical bubble.

Introducing the fully defined surface stress into the Rayleigh equation produces the Rayleigh-Plesset-Scriven equation, Equation 3.8.

$$\underbrace{\rho_L\left(R\ddot{R} + \frac{3}{2}\dot{R}^2\right)}_{\text{Interia}} + \underbrace{\frac{4\mu_L \dot{R}}{R}}_{\substack{\text{Dynamic}\\ \text{Viscosity}}} + \underbrace{\frac{2\gamma}{R}}_{\substack{\text{Static Surf}\\ \text{Tension}}} + \underbrace{\frac{4\kappa^s \dot{R}}{R^2}}_{\substack{\text{Surface}\\ \text{Dilatation}}} = \underbrace{P_B - P_\infty}_{\text{Pressure Diff.}} \tag{3.8}$$

An order of magnitude analysis completed by Pierson [62] applied a sinusoidal pressure to the Rayliegh-Plesset-Scriven equation to evaluate the behavior of the individual terms. The sinusoidal pressure was a realistic representation of the pressure a bubble would see as it traveled around the circumference of the bearing. The dynamic viscosity and inertia terms were many

orders of magnitude smaller than the pressure difference, surface dilatation, and static surface tension. Surface dilatation was the second largest term, highlighting Scriven's significant contribution to the initial inclusion of this stress on the bubble. To balance efficiency with accuracy, the inertial term was removed. At the same time, the dynamic viscosity remained as the dynamic viscosity did not add difficulty to the discretization as the inertia term did [62]. The result of the order of magnitude analysis is Equation 3.10.

$$4\frac{\mu_L \dot{R}}{R} + \frac{2\gamma}{R} + \frac{4\kappa^s \dot{R}}{R^2} = P_B - P_\infty \tag{3.10}$$

The Reynolds equation and Rayleigh-Plesset-Scriven equation were coupled through the pressure within the fluid film, P_{fluid} in addition to the bulk properties of the fluid which were affected by the void fraction, α. The fluid pressure, P_{fluid}, found from the Reynolds equation, is also P_∞ in the Rayleigh-Plesset-Scriven equation since both represent the pressure of the fluid within the cell. The fluid started as a homogeneous two-phase fluid, where all cells had a bubble nucleus included at initialization.

The motion of the bubbles was represented with an Eulerian approach where the full definition of the changing radius was Equation 3.11.

$$\frac{DR}{Dt} = \frac{\partial R}{\partial t} + \bar{u}\frac{\partial R}{\partial x} + \bar{v}\frac{\partial R}{\partial y} \tag{3.11}$$

The velocities within the fluid were defined in Equations 3.12 and 3.13; they assumed fully laminar flow. The mean velocity of the oil film was taken across the

film thickness, $y = 0$ to $y = h$, where the pressure gradient was based on the solution of the Reynolds equation.

$$\bar{u} = \frac{1}{h}\int_0^h u\, dz = \frac{u_0}{2} - \left(\frac{dP}{dx}\right)\frac{h^2}{12\mu} \tag{3.12}$$

$$\bar{v} = \frac{1}{h}\int_0^h v\, dz = -\left(\frac{dP}{dy}\right)\frac{h^2}{12\mu} \tag{3.13}$$

Including the full definition for the radius change into the Rayleigh-Plesset-Scriven equation resulted in Equation 3.14. When the pressure from the Reynolds solution, P_{RE}, was less than the difference between the bubble pressure and the surface tension, the bubble grew. Conversely, the bubble shrank when the surrounding pressure was less than the difference between the bubble pressure and surface tension. The model allowed the bubble to collapse to smaller than its starting size, but it was always assumed to exist.

$$\frac{\partial R}{\partial t} + \bar{u}\frac{\partial R}{\partial t} + \bar{v}\frac{\partial R}{\partial t} = \left(\frac{4\mu_l}{R} + \frac{4\kappa^s}{R^2}\right)^{-1}\left(P_B - \frac{2\gamma}{R} - P_{RE}\right) \tag{3.14}$$

The pressure within the bubble used the ideal gas law to calculate changes. The process was assumed to be isothermal and did not permit mass transfer across the bubble's boundary; only the volume change affected the pressure. The initial pressure put the bubble in equilibrium with the initial pressure of the film.

$$P_B = P_{B0}\frac{T}{T_0}\left(\frac{R}{R_0}\right)^3 \; ; T_0 = T_{init,oil} \tag{3.15}$$

The local void fraction, α, was defined as a ratio of the volume of the bubble over the volume of the cell in which it resided. While unrealistic, especially in a shearing environment, the bubble was assumed to be spherical. This assumption became more unlikely as the bubble grows, but remained for lack of a practical alternative.

$$\alpha = \frac{\frac{4}{3}\pi R^3}{V_{cell}} \tag{3.16}$$

The no mass transfer assumption allowed the definition of density to drive the changing density of the bubble gas. The definition of density and its rearrangement for mass, Equation 3.17, demonstrated how the density at a current time step was found based on the original density and bubble radius, Equation 3.18. Throughout the simulation, the fluid properties remained constant.

$$\rho_G = \frac{m}{V} \rightarrow \rho_G V = m \tag{3.17}$$

$$\rho_{G0} V_0 = \rho_G V \rightarrow \rho_G = \rho_{G0} \frac{R_0^3}{R^3} \tag{3.18}$$

3.2.1 Modified Rayleigh-Plesset-Scriven Equation, Void Transport

It is well known that a grid-independent solution is desirable for numerical computations. The Rayleigh-Plesset-Scriven equation above is inherently

dependent on the grid size. The initialization process requires an initial void fraction and an initial bubble radius. Suppose the void fraction is held constant ($\alpha_{init} = Const.$), then the initial radius, R_{init} (Equation 3.19), depends on Δx and Δy because the void fraction is dependent on the volume of the cell. If R_{init} is held constant, then α_{init} will vary because the volume of the cells changes around the bearing, significantly at a high eccentricity since $h(x, y)$.

$$R_{init} = \sqrt[3]{\frac{3V_{cell}\alpha_{init}}{4\pi}};\ V_{cell} = \Delta x \cdot \Delta y \cdot h(x, y) \tag{3.19}$$

It is clear that R_{init} and α_{init} are related through volume. The first step in the development is the introduction of the following two variables:

R_{char} – characteristic bubble radius of the initial field of bubbles

C_B – bubble concentration factor.

The goal of C_B is to maintain bubble size by changing the number of bubbles in bigger cells. The application of C_B is demonstrated in Equations 3.20 and 3.21. The initial void fraction as previously defined, and the initial void fraction as currently defined with C_B, R_{char} are set equal.

$$\alpha_{init,1} = \frac{4\pi R_{init}^3}{3V_{cell}};\quad \alpha_{init,2} = C_B \frac{4\pi R_{char}^3}{3V_{cell}}; \tag{3.20}$$

$$\alpha_{init,1} = \alpha_{init,2} \tag{3.21}$$

Simplifying this leads to the definition of the bubble concentration factor as the cubed ratio of the initial bubble radius over the characteristic bubble radius. Figure 3.4 demonstrates the concept of the void fraction of cells of different sizes with and without the bubble concentration factor. The bubble concentration factor allows the initial void fraction and the initial radius to be the same for volumes of different sizes.

$$C_B = \left(\frac{R_{init}}{R_{char}}\right)^3 \tag{3.22}$$

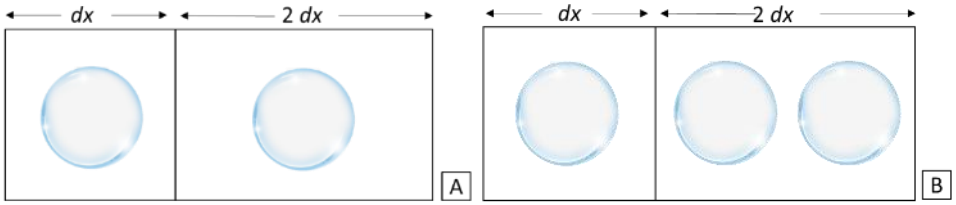

Figure 3-4: Comparison of void fraction without C_B (A) and void fraction calculation with C_B(B).

The introduction of constant *A* presents a direct relationship between the bubble's radius and the void fraction. However, C_B is still dependent on the cell size. To be genuinely grid independent, C_B must be eliminated.

$$\alpha = C_B \frac{4\pi R^3}{3V_{cell}} \rightarrow R = \sqrt[3]{\frac{3V_{cell}\alpha}{4\pi C_B}} = A\alpha^{1/3} \tag{3.23}$$

The Rayleigh-Plesset-Scriven equation was rewritten regarding the void fraction, Equation 3.24, which included the bubble concentration factor.

$$\frac{\partial R}{\partial \alpha}\frac{\partial \alpha}{\partial t} + u\frac{\partial R}{\partial \alpha}\frac{\partial \alpha}{\partial x} + v\frac{\partial R}{\partial \alpha}\frac{\partial \alpha}{\partial x} = \left(\frac{4\mu_l}{R} + \frac{4\kappa^s}{R^2}\right)^{-1}\left(P_B - \frac{2\gamma}{R} - P_{RE}\right) \tag{3.24}$$

Considering an alternate form of the definition for the bubble concentration factor and writing R_{init}^3 in terms of the variables α_{init} and V_{cell} from the initialization procedure (Equation 3.25), will allow removal of the bubble concentration factor in the definition of *A.*

$$C_B = \frac{R_{init}^3}{R_{char}^3}; \quad R_{init}^3 = \frac{3V_{cell}\alpha_{init}}{4\pi}; \; C_B = \frac{\frac{3V_{cell}\alpha_{init}}{4\pi}}{R_{char}^3} = \frac{3V_{cell}\alpha_{init}}{4\pi R_{char}^3} \tag{3.25}$$

$$A = \sqrt[3]{\frac{3V_{cell}}{4\pi C_B}} = \sqrt[3]{\frac{3V_{cell}}{4\pi\frac{3V_{cell}\alpha_{init}}{4\pi R_{char}^3}}} = \frac{R_{char}}{\sqrt[3]{\alpha_{init}}} \tag{3.26}$$

With the use of the alternative definitions, the last dependence on grid cell size was removed. The value of A set by these two parameters played a role in the resistance to bubble growth and collapse since it was used to determine the representative value of R and $\frac{\partial R}{\partial \alpha}$.

$$R = A\alpha^{1/3};\ \text{and}\ \frac{\partial R}{\partial \alpha} = \frac{A}{3\alpha^{2/3}};\ \text{where}\ A = \frac{R_{char}}{\sqrt[3]{\alpha_{init}}} \tag{3.27}$$

The final form of the Rayleigh-Plesset-Scriven, in terms of α, was given in Equation 3.28 and was used in the numerical simulation for cavitation within the working fluid.

$$\frac{\partial \alpha}{\partial t} + \bar{u}\frac{\partial \alpha}{\partial x} + \bar{v}\frac{\partial \alpha}{\partial x} = \frac{3\alpha^{2/3}}{A}\left(\frac{4\mu_l}{A\alpha^{1/3}} + \frac{4\kappa^s}{A^2\,\alpha^{2/3}}\right)^{-1}\left(P_B - \frac{2\gamma}{A\alpha^{1/3}} - P_{\mathrm{RE}}\right) \tag{3.28}$$

In Equation 3.28, $\bar{u}$ and $\bar{v}$ represented the average circumferential and axial velocities, respectively, calculated across the film thickness by Equations 3.12 and 3.13. The bubble pressure, P_B, was calculated by Equation 3.29 using the representative bubble radius (Equation 3.17) along with the ideal gas law. The bubble's initial pressure was the oil's initial pressure plus the surface tension.

$$P_B = P_{B0}\frac{T}{T_0}\left(\frac{R_{char}}{A\alpha^{1/3}}\right)^3;\ \ P_{B0} = P_{init,oil} + 2\frac{\gamma}{R_{char}} \tag{3.29}$$

The density of the bubble remained based on the ideal gas law as in Equation 3.17.

$$\rho_G = \rho_{G0}\left(\frac{R_{char}}{A\alpha^{1/3}}\right)^3 \tag{3.30}$$

The initial void fraction, α_{init}, characteristic bubble radius, R_{char}, and the dilatational viscosity, κ^s, are considered cavitation model settings and should be held constant for the extent of cohesive studies.

3.2.2 Discretization of the Rayleigh-Plesset-Scriven Equation

The void fraction at each location in the film is found with Equation 3.31.

$$\alpha_{i,j} = \frac{\frac{4}{3}\pi R_{i,j}^3}{(V_{cell})_{i,j}} \tag{3.31}$$

The grid-independent Rayleigh-Plesset-Scriven Equation, 3.28, is discretized using first-order time integration and a first-order upwind scheme for convective terms. Equation 3.32 resulted after this discretization procedure was applied to every term.

$$\frac{\alpha^{n+1} - \alpha^n}{\Delta t} + \bar{u}\frac{\alpha_{i,j}^n - \alpha_{i-1,j}^n}{\Delta x} + \bar{v}\frac{\alpha_{i,j}^n - \alpha_{i,j-1}^n}{\Delta y} = \frac{3\alpha^{2/3}}{A}\left(\frac{4\mu_l}{A\alpha^{1/3}} + \frac{4\kappa^s}{A^2\,\alpha^{2/3}}\right)^{-1}\left(P_B - \frac{2\gamma}{A\alpha^{1/3}} - P_{\mathrm{RE}}\right) \tag{3.32}$$

This equation was rearranged to determine the bubble radius for the next time step, $\alpha_{i,j}^{n+1}$.

$$\alpha_{i,j}^{n+1} = \alpha_{i,j}^{n} + \Delta t \left(\frac{3\alpha^{2/3}}{A} \left(\frac{4\mu_l}{A\alpha_{i,j}^{1/3}} + \frac{4\kappa^s}{A^2\alpha_{i,j}^{1/3}} \right)^{-1} \left(P_{B,i,j} - \frac{2\gamma}{\alpha_{i,j}} - P_{RE,i,j} \right) - \bar{u}\frac{d\alpha_{i,j}^{n}}{dx} - \bar{v}\frac{d\alpha_{i,j}^{n}}{dx} \right) \quad 3.33$$

The velocity terms were discretized with a first-order central discretization.

$$\bar{u} = \frac{u_0}{2} + \left(\frac{P_{i+1,j}^{n} - P_{i-1,j}^{n}}{\Delta x} \right) \frac{(h^2)_{i,j}}{12\mu_{i,j}} \quad 3.34$$

$$\bar{v} = \left(\frac{P_{i,j+1}^{n} - P_{i,j-1}^{n}}{\Delta y} \right) \frac{(h^2)_{i,j}}{12\mu_{i,j}} \quad 3.35$$

The direction, or sign of the velocity term at each location determined whether the upwind or downwind derivative was used for the coefficient of the velocity in Equation 3.36.

$$\begin{aligned} \frac{d\alpha_{i,j}^{n}}{dx} &\approx \frac{\alpha_{i,j}^{n} - \alpha_{i-1,j}^{n}}{\Delta x} \quad \text{if } \bar{u} > 0 \\ \frac{d\alpha_{i,j}^{n}}{dx} &\approx \frac{\alpha_{i+1,j}^{n} - \alpha_{i,j}^{n}}{\Delta x} \quad \text{if } \bar{u} < 0 \\ \frac{d\alpha_{i,j}^{n}}{dy} &\approx \frac{\alpha_{i,j}^{n} - \alpha_{i,j-1}^{n}}{\Delta y} \quad \text{if } \bar{v} > 0 \\ \frac{d\alpha_{i,j}^{n}}{dy} &\approx \frac{\alpha_{i,j+1}^{n} - \alpha_{i,j}^{n}}{\Delta y} \quad \text{if } \bar{v} < 0 \end{aligned} \quad 3.36$$

3.2.3 Fukamatsu Experiment Comparison

The experiments done by Fukamatsu [72] have previously been used by Someya [73] to characterize the ability of bubble theory to depict the negative

pressure within a bearing. The shaft had a diameter of 99.80 mm with a clearance ratio of $2.2\ x\ 10^{-3}$ as shown in Figure 3.5. A supply groove at the axial centerline was 22.50 mm from the edge of the bearing and had an absolute pressure of 300 kPa. A constant rotational speed was used to develop pressure supporting four different load scenarios. A flush-mounted pressure transducer (on the rotating shaft) measured the pressure distribution within the bearing clearance.

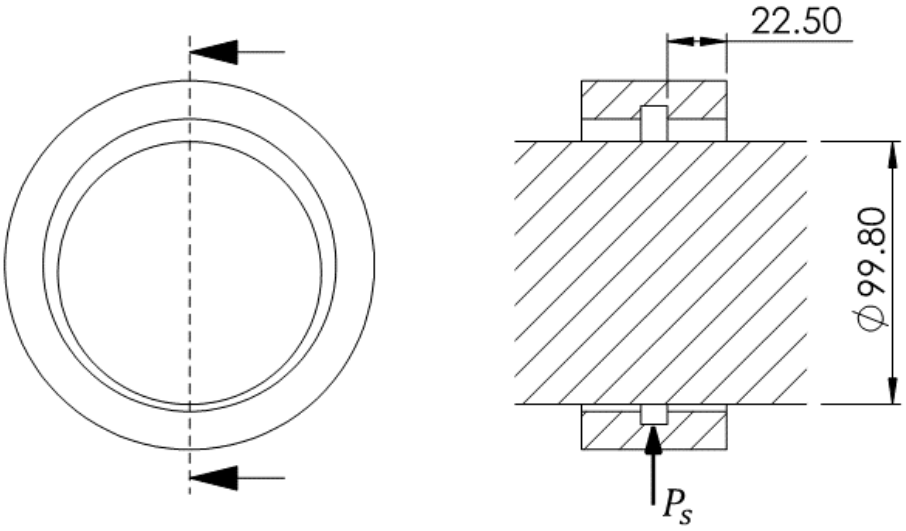

Figure 3-5: Solid journal bearing used in experiments [72].

The material properties are detailed in Table 3.1. The supplied oil was single-grade SAE#20W at 50ºC. The viscosity was 0.02996 Pa·s, and density was 879.7 $\frac{\mathrm{kg}}{\mathrm{m}^3}$. The initial void and dilatational viscosity have been shown to significantly affect the results of the cavitated portion of the fluid [62]. These

parameters were determined by locating those that best reproduced Fukamatsu's results. The parameters were kept constant for the remainder of the cavitation investigations.

Table 3-1: Bearing parameters used to validate the cavitation model.

Bearing Specifications	
Length [mm]	22.5
Radius [mm]	49.9
Clearance (c) [mm]	0.1098
Material Properties of Oil and Air	
Oil Density (ρ_L) [$\frac{\mathrm{kg}}{\mathrm{m}^3}$]	879.7
Air Density for initial bubble size (ρ_{G0}) [$\frac{\mathrm{kg}}{\mathrm{m}^3}$]	0.9996
Oil Viscosity (μ_L) [$\mathrm{Pa} \cdot \mathrm{s}$]	0.02996
Air Viscosity (μ_G) [$\mathrm{Pa} \cdot \mathrm{s}$]	$2.12 \cdot 10^{-5}$
Operating Conditions	
Load (W) [kN]	1.4, 2.8. 4.2 and 5.6
Rotational Velocity (ω) [RPM]	1500
Supply Pressure (P_s) [kPa]	300
Cavitation Settings	
Dilatational Viscosity (κ^s) [Ns/m]	$3.75 \cdot 10^{-4}$
Initial Void Fraction (α_{init})	0.01
Characteristic Bubble Radius [m]	$3.0 \cdot 10^{-6}$

While in practice, the code uses a set eccentricity and speed and outputs a load, for the experimental comparison, the input criteria were the speed and load, and the simulation iterated on eccentricity until Fukamatsu's [72] load was achieved within 5%. Figure 3-6 demonstrates the Rayleigh-Plesset-Scriven model's ability to capture the negative pressure when the bearing reaches the

adequate load. The numerical result somewhat overpredicted the maximum pressure compared to the experimental results as is common to bubble theory simulations [62,73]. Figure 3-6 depicts the case with an external load of 56 kN. The bubble theory models are all able to capture the negative pressure present in the experimental results. The negative pressures demonstrate the advantage of using bubble dynamics, in this case the Rayleigh-Plesset-Scriven equation, over the Gumbel cavitation model which is unable to exhibit the negative pressures present in the experiment.

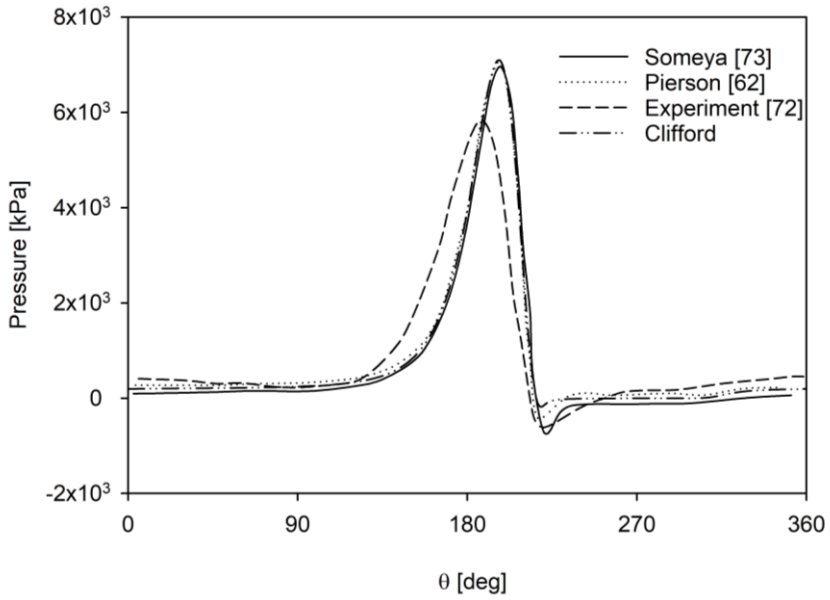

Figure 3-6: Characterization of the tensile capabilities of bubble theory cavitation models [62, 72, 73].

3.3 Thin film energy equation

Overall, the derivation was similar to the Reynolds equation, as shown in the development. The derivation of the thin film energy equation began slightly differently from the Reynolds equation development, with the initial control volume spanning the film thickness. The assumptions from the Reynolds equation derivation (1-9) also applied to this derivation in addition to two others:

- The heat generation due to velocity gradients of u and v in the z direction dominates while all other terms are neglected. This is because the velocity gradient across the radial direction is much larger than in other directions.
- The circumferential direction has much more energy advection than dissipation. In the axial direction, advection may be small in some locations, so only conduction is considered in the axial direction.

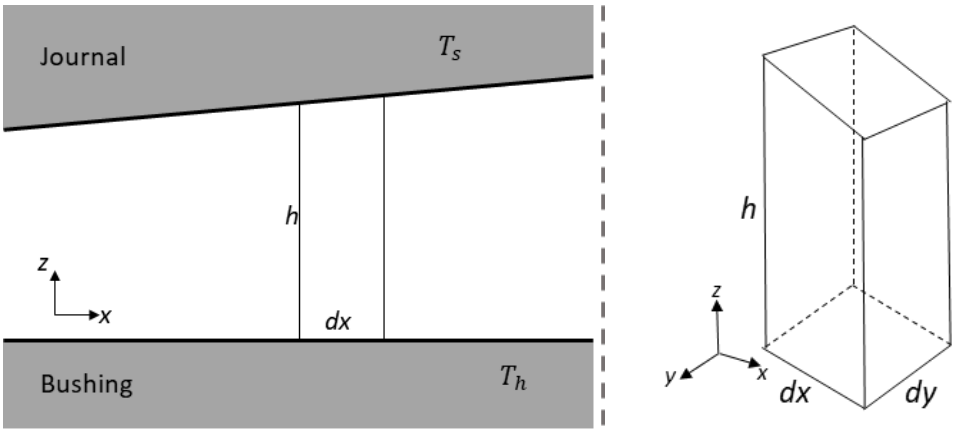

Figure 3-7: The control volume for the development of the thin film energy equation. The initial control volume is drawn across the entire thickness of the film.

Using the energy conservation form of the Reynolds Transport Theorem, the control volume shown above was used to move toward a differential equation. The velocities utilized are average velocities across the height of the differential element.

$$\dot{Q} = \frac{\partial}{\partial t}\iiint_V \rho c T dV + \iint_S \rho c T(\vec{v}\cdot\vec{n})dS \qquad 3.37$$

The left-hand side of the equation represented the internal energy generation through viscous dissipation and heat transfer through convection and conduction in the axial direction. The transient term described energy storage within the control volume over time where t is time, ρ is density, c is specific heat, T is temperature, and V is volume. Lastly, the second integral represented the energy flux, or energy carried via advection into and out of the control volume

where $\vec{v}$ is the vector of velocity, $\vec{n}$ is a vector normal to a given surface and S is the area of the surface. Figure 3-8 below showed the fluxes due to advection in each direction and the energy stored in the representative control volume.

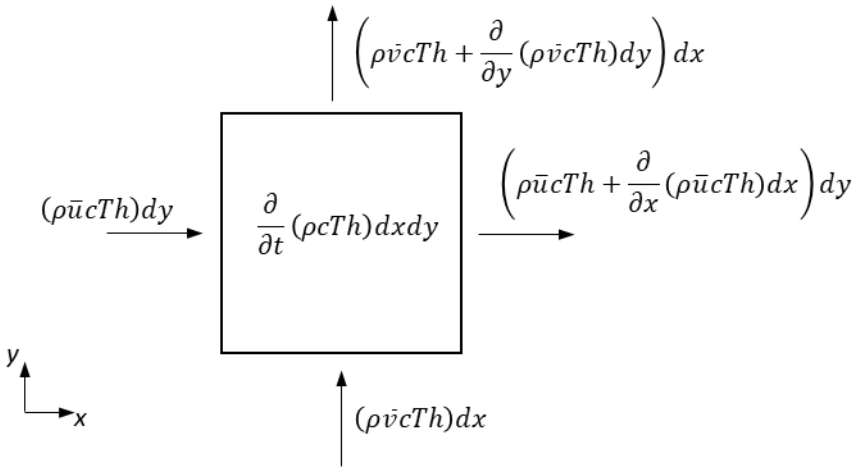

Figure 3-8: Energy advection and storage for thin film energy equation.

Collecting these fluxes evaluated in their respective integrals resulted in Equation 3.38 as the new right-hand side of Equation 3.38, simplified to Equation 3.39.

$$\begin{aligned}\frac{\partial}{\partial t}\iiint_V \rho cT dV + \iint_S \rho cT(\vec{v}\cdot\vec{n})dS \\ = \frac{\partial(\rho cTh)}{\partial t}dxdy - (\rho\bar{u}cTh)dy \\ + \left(\rho\bar{u}cTh + \frac{\partial(\rho\bar{u}cTh)}{\partial x}dx\right) - (\rho\bar{u}cTh)dx \\ + \left(\rho\bar{v}cTh + \frac{\partial(\rho\bar{v}cTh)}{\partial y}dy\right)dx\end{aligned} \quad 3.38$$

$$\dot{Q} = \frac{\partial(\rho cTh)}{\partial t}dxdy + \frac{\partial(\rho \bar{u} cTh)}{\partial x}dxdy + \frac{\partial(\rho \bar{v} cTh)}{\partial y}dxdy \quad 3.39$$

The left-hand side term represented the generated energy (q_{gen}), conduction in the axial direction $(q_{y,cond})$ and convection at the surface of the housing (q_o) and shaft (q_h) of the bearing is shown below in Figure 3-9. Evaluation of these components resulted in Equation 3.40.

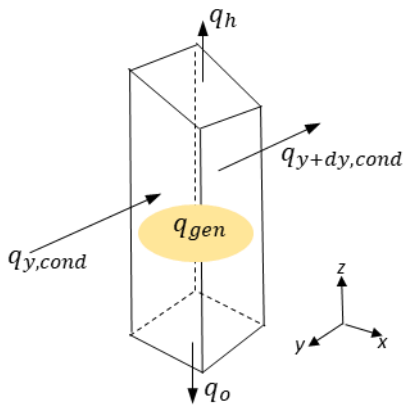

Figure 3-9: Energy transfer and generation through convection, conduction, and viscous dissipation.

$$\dot{Q} = \left(q_{cond,y} - q_{cond,y+\Delta y}\right)hdx + \left(q_{gen} - q_h - q_0\right)dxdy \quad 3.40$$

The convection terms were treated using convective heat transfer coefficients (HTC) for the housing and the shaft. In Equation 3-41, T was the oil film temperature, h_s was the HTC for the shaft, T_s was the shaft temperature, h_h was the HTC for the housing and T_h was the housing temperature. Cooling occurred from heat loss to the shaft/porous bushing through convection and

advection of cool liquid from the axial boundaries and fluid exchange with the porous bushing.

$$q_h = h_s(T - T_s);\ \ q_0 = h_h(T - T_h) \tag{3.41}$$

The complete viscous dissipation terms caused by various viscous stresses for a compressible fluid were given in Equation 3.42 [74]. Due to the small bearing clearance (radial velocity gradient being considerable compared to the other directions), only the terms created through shear across the radial direction of the bearing were retained in Equation 3.43. It was assumed that the heat generation due to velocity gradients of *u and v* in the *z* direction was more significant than in other directions, so all other viscous dissipation terms were neglected.

$$\begin{aligned}\Phi = 2\mu\left[\left(\frac{\partial u}{\partial x}\right)^2 + \left(\frac{\partial v}{\partial y}\right)^2 + \left(\frac{\partial w}{\partial z}\right)^2\right] \\ + \mu\left[\left(\frac{\partial u}{\partial y} + \frac{\partial v}{\partial x}\right)^2 + \left(\underbrace{\frac{\partial u}{\partial z}}_{retained} + \frac{\partial w}{\partial x}\right)^2\right. \\ \left. + \left(\frac{\partial w}{\partial y} + \underbrace{\frac{\partial v}{\partial z}}_{retained}\right)^2\right] + \lambda\left(\frac{\partial u}{\partial x} + \frac{\partial v}{\partial y} + \frac{\partial w}{\partial z}\right)^2\end{aligned} \tag{3.42}$$

Viscous dissipation created heat generation. The heat generation for the differential volume considered the assumed velocity profiles used in the Reynolds equation (Equations 2.25 and 2.26). After executing the derivatives $\left(\frac{\partial u}{\partial z}\right.$ and $\left.\frac{\partial v}{\partial z}\right)$, the viscous dissipation terms were integrated across the height of

the control volume to produce Equation 3.43, which was the thin film viscous dissipation term, q_{gen}.

$$q_{gen} = \int_0^h \left(\left(\frac{\partial u}{\partial z}\right)^2 + \left(\frac{\partial v}{\partial z}\right)^2 \right) dz = \mu \frac{u_0^2}{h} + \frac{h^3}{12\mu} \left(\left(\frac{dp}{dx}\right)^2 + \left(\frac{dp}{dy}\right)^2 \right) \quad 3.43$$

Updating Equation 3.40 with the further defined $q_h, q_0, and\ q_{gen}$ gave Equation 3.44.

$$\frac{\partial q_{y,cond}}{\partial y} h + \left(q_{gen} - q_h - q_0\right) = \frac{\partial(\rho c T h)}{\partial t} + \frac{\partial(\rho \bar{u} c T h)}{\partial x} + \frac{\partial(\rho \bar{v} c T h)}{\partial y} \quad 3.44$$

The right-hand side of Equation 3.44 was further simplified by considering the continuity equation of the thin film.

$$\frac{\partial(\rho h)}{\partial t} + \frac{\partial(\rho \bar{u} h)}{\partial x} + \frac{\partial(\rho \bar{v} h)}{\partial y} = 0 \quad 3.45$$

The thin film continuity equation was present in Equation 3.44 when the constant cT was factored out of the right-hand side terms. This allowed for a simplification since continuity stated those terms equaled zero.

$$\text{LHS} = \underbrace{cT \left(\frac{\partial(\rho h)}{\partial t} + \frac{\partial(\rho \bar{u} h)}{\partial x} + \frac{\partial(\rho \bar{v} h)}{\partial y} \right)}_{=0} + \rho h \frac{\partial(cT)}{\partial t} + \rho \bar{u} h \frac{\partial(cT)}{\partial x} + \rho \bar{v} h \frac{\partial(cT)}{\partial y} \quad 3.46$$

The final form of the energy equation for the thin film, Equation 3.47 was obtained after applying Fourier's law [75] to the conduction term and k and c were assumed constant values.

$$\frac{\partial(T)}{\partial t} = \frac{k}{\rho c}\frac{\partial^2 T}{\partial y^2} - \bar{u}\frac{\partial(T)}{\partial x} - \bar{v}\frac{\partial(T)}{\partial y} + \frac{1}{\rho c h}\left(\mu\frac{u_0^2}{h} + \frac{h^3}{12\mu}\left(\left(\frac{dP}{dx}\right)^2 + \left(\frac{dP}{dy}\right)^2\right) - h_s(T - T_s) - h_h(T - T_h)\right) \quad 3.47$$

3.3.1 Geometry and Material Properties

Including the thin film energy equation introduced a temperature dependence of the material properties. The oil properties, density, and viscosity were altered based on empirical models from a tribology handbook. For the bubbles, gas, the change in viscosity was a direct function of temperature based on Sutherland's law. In pseudo cavitation, it was assumed that there was no mass transfer to the bubble; it grew only due to a decrease in pressure. Since the fluid properties alter the pressure, the growth of the bubble accounted for temperature changes, but the properties of the air bubble were not directly tied to the temperature. The bubble's pressure was controlled by the ideal gas law, where density was temperature dependent. The fluid and gas were tied to temperature from both sides of the bubble boundary. When the temperature increased, the bubble

pressure increased, resulting in a larger bubble size and smaller densities through the Rayleigh-Plesset-Scriven equation.

The model continued to use ISO VG 32 oil for thermal simulations. The empirical equations below were used for the oil's density and viscosity based on temperature from the Handbook of Lubrication Vol II, Second Edition [76].

$$\rho_L = 889.5 - 0.6097T \tag{3.48}$$

$$\mu_L = 5.85 \cdot 10^{-5} \exp\left(\frac{911.03}{T + 109.15}\right) \tag{3.49}$$

Sutherland's law [77] calculated the viscosity of the gas bubble in units of Kelvin. In the equation above, the temperature had units of degrees Celsius.

$$\mu_G = \frac{C_1 T^{3/2}}{T + S};\ S = 110.4\ \mathrm{K}; C_1 = 1.458 \cdot 10^{-6}\ \frac{\mathrm{kg}}{\mathrm{m} \cdot \mathrm{s}\sqrt{\mathrm{K}}} \tag{3.50}$$

The same grid and computational domain were employed for the temperature field. An additional convergence criterion was added to the global loop for temperature.

$$\text{Converged when: } \frac{\sum T_{i,j}^{n+1} - \sum T_{i,j}^{n}}{\sum T_{i,j}^{n+1}} < 10^{-8} \tag{3.51}$$

The numerical flowchart in Figure 3-10 demonstrates the flow of computation and interaction of the convergence criteria used.

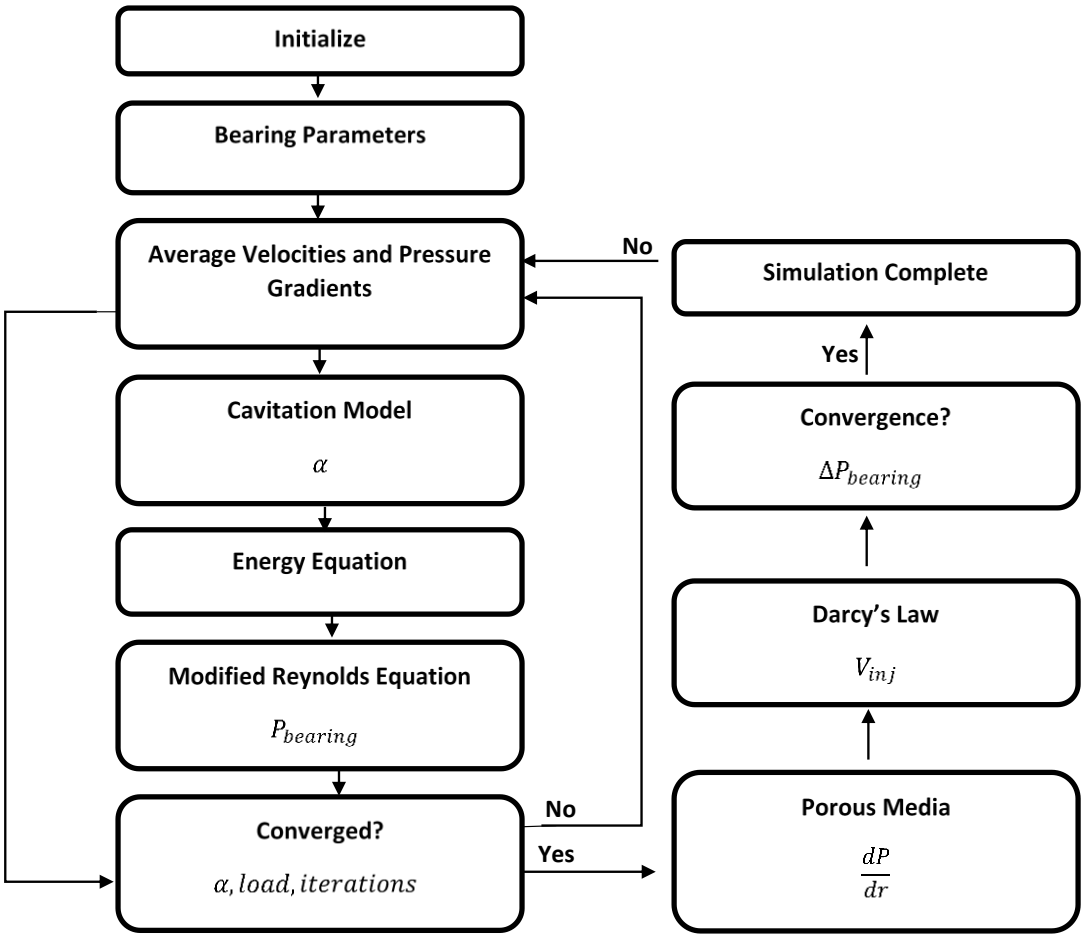

Figure 3-10: Numerical Flowchart coupling the Rayleigh-Plesset-Scriven, Reynolds, energy, and porous bushing equations.

CHAPTER IV

RESULTS AND DISCUSSION

Figure 4-1 shows the pressure distribution within the fluid film for the self-circulating bearing. The pressure profile resembles a typical journal bearing: a half Sommerfeld curve for the positive pressure and the tensile stresses (negative pressure) in the divergent region of the bearing. The injection velocity from the porous bushing was small enough as to not significantly change the pressure profile within the fluid film.

The expected pressure curve drove the selection of the grid for the numerical simulations. The profile in the circumferential direction called for a minimum of five points to define: the boundaries, maximum, inflection point, and minimum pressure. The grid in the circumferential direction consisted of divisions in multiples of five to ensure proper characterization of the pressure curve. The axial direction pressure was parabolic and thus required a minimum of three points to characterize so a multiple of three was used for the grid divisions in the axial location. Table 4-1 demonstrated the grid independence created by the bubble concentration factor in the Rayleigh-Plesset-Scriven derivation [62]. Three sample grids were tested, and the bearing load capacity varied less than 1% for each grid size. There was not a large time consequence for the simulations

presented and since a denser grid allowed for a more accurate curve fitting for the pressure representation in the bushing solution, a grid of 200x45 was used for the results discussed.

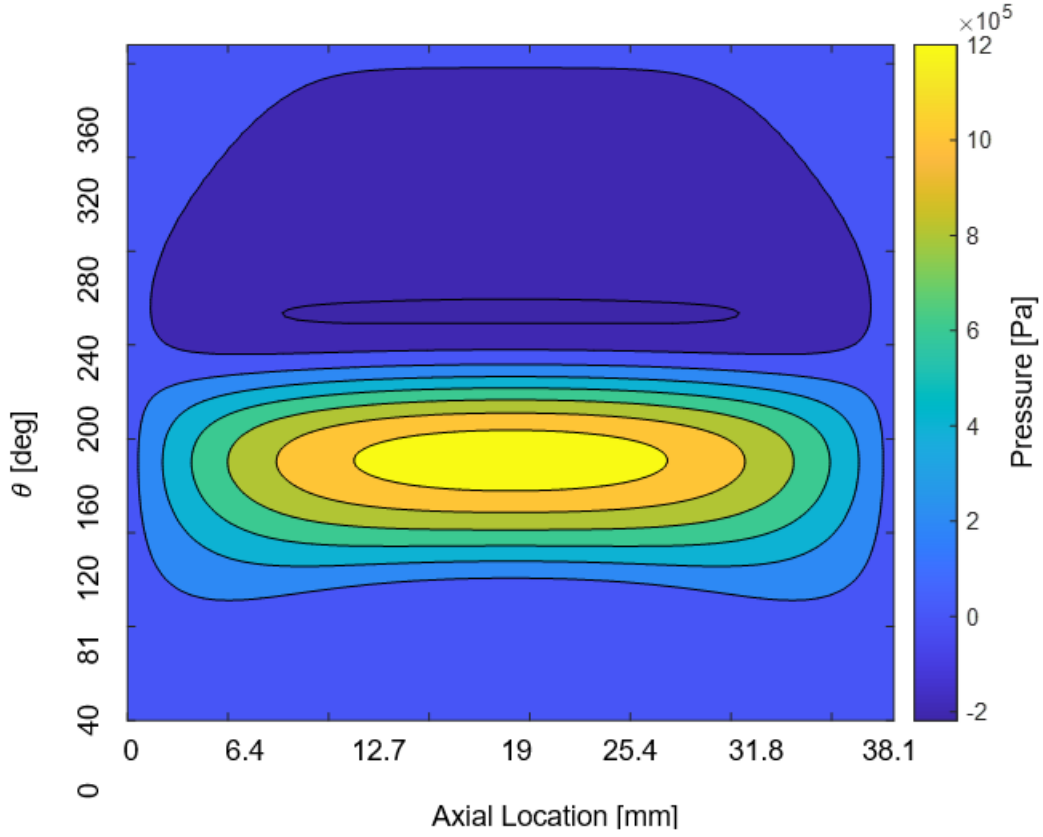

Figure 4-1: Pressure contour within the fluid film.

Table 4-1: Load results for varying grid sizes.

Grid	Load [N]
75x27	712
100x30	708
200x45	708

The time step was selected based on a convergence study as well which is presented in Table 4-2. The rapid bubble growth and collapse required a small time step for the forward time derivatives. A time step of 1e-6 was used for the simulations to ensure proper capture of bubble collapse.

Table 4-2: Load results for varying time steps.

Time Step [s]	Load [N]
1e-4	585.2
1e-5	585.3
1e-6	585.4

4.1 Effect of Bushing Pressure Representation

Darcy's law was used to calculate the injection velocity, which used a pressure differential in the radial direction to determine the velocity of fluid entering/exiting the fluid film. A first-order differential for the change in pressure in the radial distribution implied a linear pressure distribution assumption within the porous bushing which is shown in Equation 4.1. Equation 4.2 is a second-order differential, representing the change in pressure to be used when V_{inj} was calculated within the current work.

$$\frac{dP}{dr} = \frac{P_s - P_b}{r_o - r_i} \tag{4.1}$$

In the current work, it was noted during early simulations that, dependent on the eccentricity, speed, and supply pressure, the radial pressure distribution

varied significantly throughout the porous bushing. A linear assumption was reasonable in some cases, but others had a low correlation to a linear fit. With the goal of a robust model in mind, a second-order forward numerical derivative was utilized (Equation 4.2).

$$\frac{dP}{dr} = \frac{-3P(1,\theta,z) + 4P(2,\theta,z) - P(3,\theta,z)}{2\Delta r} \qquad 4.2$$

Figure 4-1 demonstrates how the bushing's radial pressure distribution changed with axial/circumferential location. Node 1 was located at the axial boundary condition at L = 0. The axial ends of the bearing were the areas of non-linear pressure. Upon further investigation, approximately 15% of the axial locations from each end remain non-linear with various parameter changes, as shown in the pressure distributions of node 2 to 8. Thus, using the numerical derivative improved the representation of the porous bushing for approximately 30% of the bearing's length.

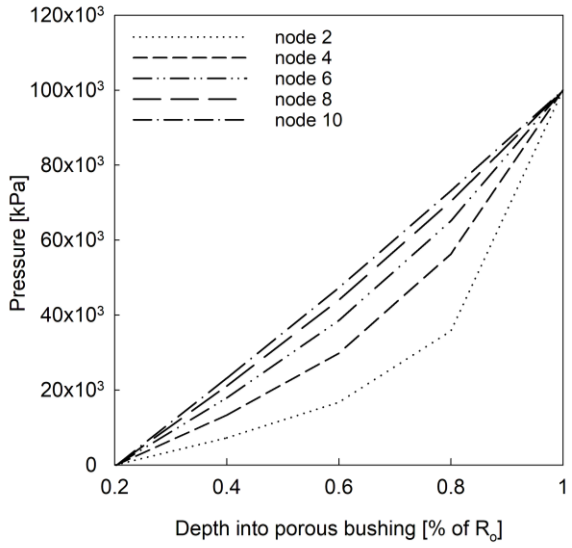

Figure 4-2: Pressure distribution in porous bushing (H = 0.2 · R; $\omega = 5000$).

4.2 Isothermal with Gumbel Cavitation

For this portion of the results, the model settings described in Table 4-3 were utilized to investigate the effect of changing parameters on the bearing's load, stability, and self-circulation. The range of permeabilities resulted in a feeding parameter spanning 4.55 to 455, with each change in permeability resulting in an order of magnitude change in the feeding parameter (Equation 2.21). The range for the porous bushing thickness was narrow, ranging from 22 to 90, to explore the effects of more minor feeding changes on the bearing. Gumbel cavitation assumes that the working fluid cannot support tensile

stresses. Therefore, any pressure that is negative, indicative of a tensile stress, was set equal to zero Pa.

It has been shown previously [78] that the trends for changing parameters were affected regardless of the permeability if the supply pressure was high enough. For example, a pressure within an order of magnitude of the maximum pressure promoted a higher load with decreased resistance to flow through the porous bushing regardless of speed or eccentricity. The low permeability range and passive reservoir representation of a shallow reservoir were selected for this work based on previous investigation results [67,78]. The passive reservoir was represented as a constant pressure surrounding the outer circumference of the bearing with a magnitude of 4 kPa for the Gumbel cavitation investigations which is characteristic of a deep reservoir surrounding the bearing.

Table 4-3: Isothermal model settings for self-circulating bearing.

Bearing Specifications	
Length [mm]	38.1
Radius [mm]	12.426
Clearance (C) [mm]	0.0254
Eccentricity (ε)	$0.1, 0.3, 0.5, 0.7$ and 0.9
Rotational Velocity (ω) [RPM]	$3{,}000$
Material Properties of Oil and Air	
Oil Density (ρ_L) [$\frac{\text{kg}}{\text{m}^3}$]	840.724
Air Density for initial bubble size (ρ_{G0}) [$\frac{\text{kg}}{\text{m}^3}$]	0.9996
Oil Viscosity (μ_L) [$\text{Pa} \cdot \text{s}$]	.00689
Air Viscosity (μ_G) [$\text{Pa} \cdot s$]	2.123 x 10^{-5}
Porous Bushing Settings	
Permeability [m^2]	5 x 10^{-13}
Thickness of the Bushing [m]	0.1*r
Passive Reservoir Representation [Pa]	4000 at all locations
Cavitation Model	
Gumbel	$P < 0; P = 0$

4.2.1 Injection Velocity

Figures 4-2 and 4-3 showed a decrease in the maximum injection velocity when the feeding parameter increased. The midplane pressure injection velocity showed how the injection velocity varies circumferentially around the bearing, with 0 and 360º representing the point of separation for the unwrapped bearing and 180º the center. These results differ from the constant supply pressure of $1x10^8$ Pa of earlier work [78] where the maximum injection velocity increased

when the feeding parameter increased. The direct correlation between injection velocity and feeding parameter was because of the unrealistically large supply pressure that was larger than the maximum pressure within the bearing clearance. To achieve an increase in the injection velocity magnitude, a shallower reservoir should be used, or the physical load on the system should be increased. In application, the pressure of the passive reservoir results from the initial charge of fluid, depth of the reservoir, and bearing operation (e.g. speed, load, eccentricity). The specific demands of the application will determine the speed and load on the bearing so designers would alter the initial charge of fluid and depth of the reservoir to control the pressure within the passive reservoir.

Experimental work [67] demonstrated a $V_{inj}$of at least $10^{-3}\ m/s$ was sufficient to circulate fluid between the working zone and passive reservoir. As shown in Figure 4-3, porous bushing thicknesses of 0.2r or greater were needed to generate an injection velocity large enough to exchange fluid between the clearance and passive reservoir. A permeability of $1x10^{-11}$ was too small; a feeding parameter of less than 100 was needed to achieve sufficient circulation of fluid between the working zone and passive reservoir.

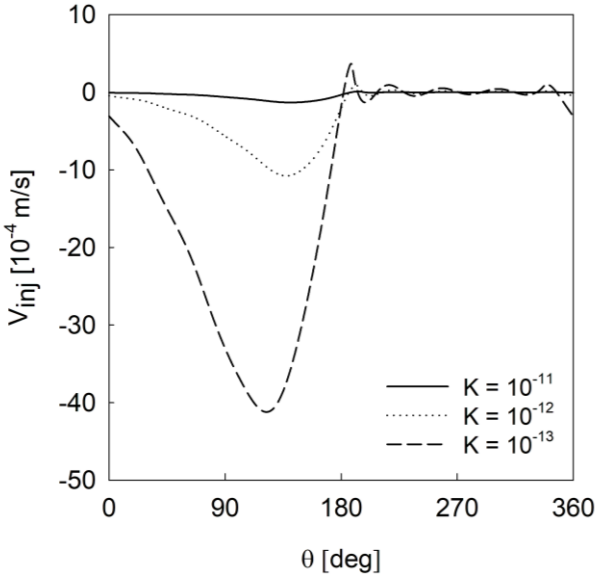

Figure 4-3: Effect of changing permeability on midplane injection velocity.

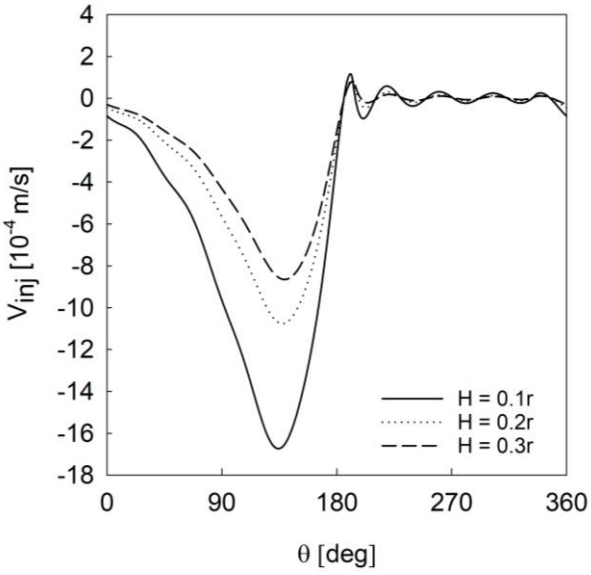

Figure 4-4: Midplane injection velocity for changing bushing thickness.

4.2.2 Permeability

Closely related to the injection velocity was the fluid film pressure. Previous works on a porous slider bearing showed increased permeability decreased the fluid pressure [10]. This effect was not replicated in the journal bearing Figure 4-4 results. All eccentricities produce nearly identical maximum pressure at the lowest permeability, $1\ x\ 10^{-13}\ m^2$. The highest eccentricity bearing showed a near constant trend for higher permeabilities. Lower eccentricities qualitatively showed the same behavior, with a dramatic increase in pressure from $1\ x\ 10^{-13}$ to $1\ x\ 10^{-12}\ m^2$ after which an increase in pressure continues with an increase in permeability but at a lower magnitude. For the permeabilities plotted in Figure 4-2, none were significantly large to obtain an injection velocity greater than 10^{-3}. As the eccentricity of the bearing increased, the fluid was more sensitive to a change in permeability. A higher eccentricity bearing would result from a high load on the bearing. In a high-loading case, one should be cautioned that a change has a more dramatic effect than at a lower eccentricity bearing. A clear linear relationship between the permeability and the maximum pressure also existed. This type of relationship was observed within slider bearings when the speed was varied [10]. Trends like this discovered in the numerical modeling can drastically improve the design rate of a bearing.

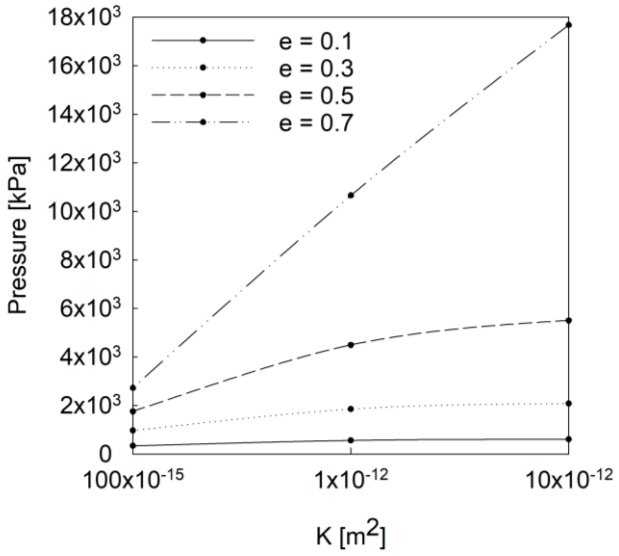

Figure 4-5: Maximum pressure for changing eccentricity at each permeability.

As the permeability increased (higher feeding parameter), the load capacity of the bearing increased, as seen in Figure 4-5. The increase in eccentricity caused a larger increase in load capacity than changing the permeability. In application the eccentricity is normally a product of the geometry and loading of the bearing instead of an input as it was numerically. At a low eccentricity setting, the change in permeability has a low effect on the load capacity and stability.

A high eccentricity bearing had a dramatic change in load capacity and stability for each permeability change but is a less likely scenario in application because of the major instability that accompanied the large load capacity. The sub-figure in the upper right hand corner of Figure 4-5 demonstrated the increase in stability that accompanied the increase in load capacity. While the magnitude

of the stability changes varied, as the load had, the trend remained consistent for all settings.

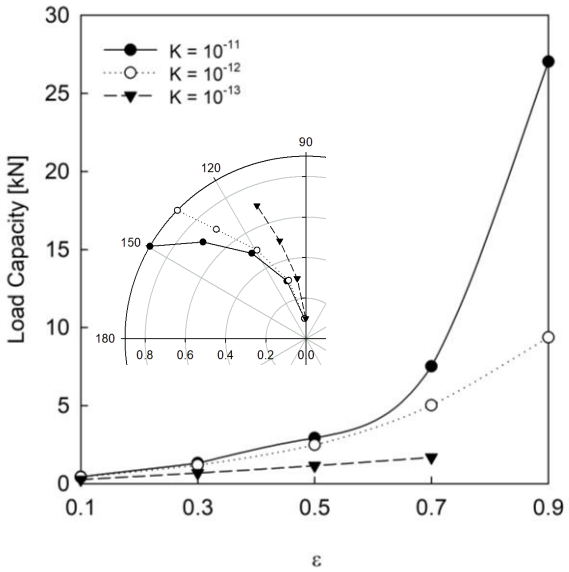

Figure 4-6: Load and stability analysis for changing permeability.

Figure 4-7 demonstrated the velocity vectors of the fluid film at each axial and circumferential location. The direction of rotation is from 0 to 360 degrees; shown with the vertical arrow. The convergent region of the bearing (0 to 120º), the area of high pressure, exhibited flow toward the axial ends of the bearing. Side leakage was observed and would indicate lubricant leaking out of the ends of the bearing. The velocity plot demonstrated this phenomenon during operation of the self-circulating bearing. In application, seals would be needed to prevent major fluid losses or a fluid with large viscosity that would pull fluid back to the centerline as it cooled near the edges of the bearing. In the divergent region of

the bearing (240 to 320º) the inverse was seen, where the cooler fluid followed the velocity vectors toward the center of the bearing.

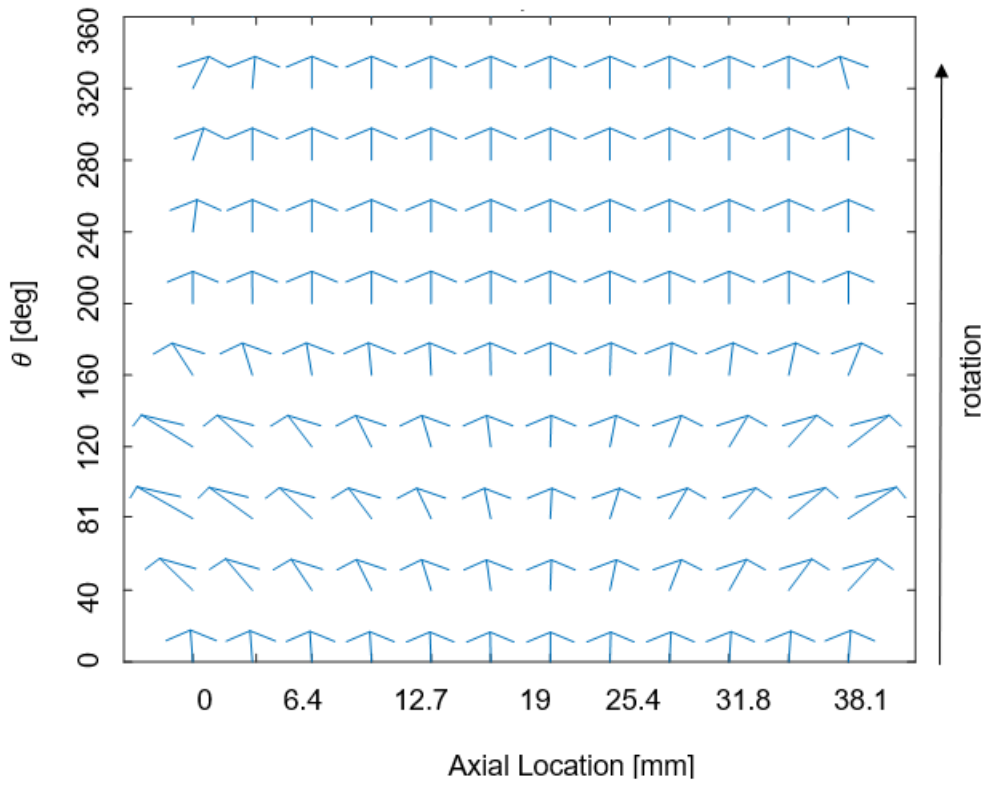

Figure 4-7: Velocity field for self-circulating bearing.

4.2.3 Effects of bushing thickness

For various porous bushing thicknesses, up to 20% of the bearing radius provided sufficient fluid flow to achieve an injection velocity of $10^{-3}\ m/s$, shown in Figure 4-4. While a thinner porous bushing led to a larger V_{inj}, it resulted in a lower pressure overall. The lower overall pressure indicated that flow occurred both into and out of the bearing clearance. If lubricant only flowed into the

bearing clearance, as in previous works [78], the increase in V_{inj} would directly correlate with increased pressure and thus load capacity. The lower pressure from a larger V_{inj} indicated proper function of the self-circulating bearing.

Figure 4-8 demonstrated that a thicker porous bushing maintained a larger load capacity. This was a result of the reservoir pressure's relationship to the fluid film pressure. Within the range of bushing thicknesses that delivered sufficient flow exchange (for temperature considerations), there was a significant gain in load capacity from 0.1r to 0.2r. Interestingly, there were not equal changes in load capacity for identical step increases in the porous bushing thickness (Figure 4-6) which indicated diminishing returns.

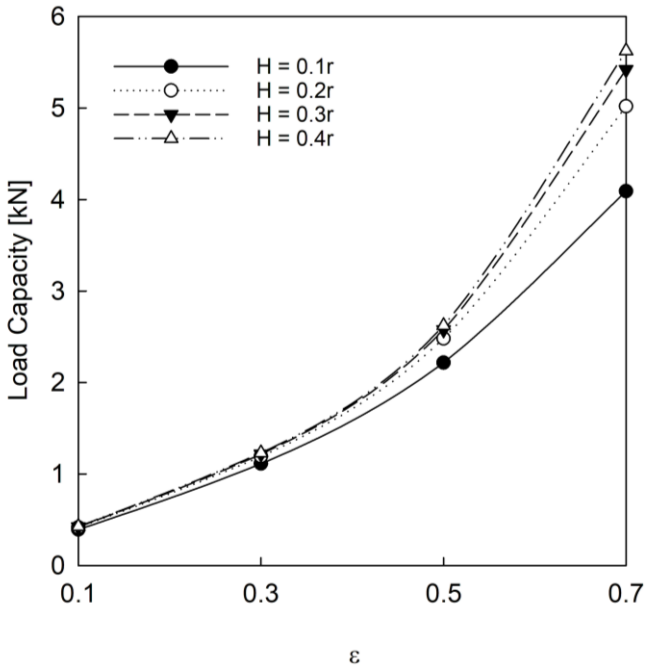

Figure 4-8: Load capacity as a function of eccentricity for various busing thicknesses.

Like shown with permeability, as the load capacity of the bearing increased, the attitude angle of the bearing increased, as shown in Figure 4-9. The change in both load and stability were less significant for the tested thicknesses than the permeabilities (Figure 4-7 and 4-6 respectively). The magnitude of changes correlated to a smaller change in feeding parameter for the bushing thicknesses compared to the feeding parameters for the permeability variations.

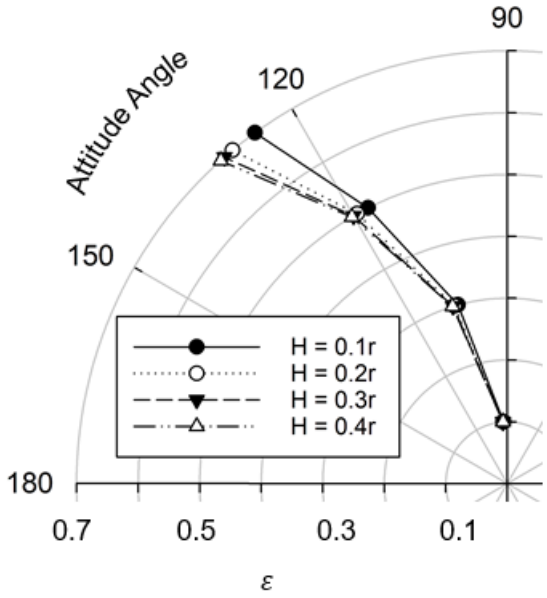

Figure 4-9: Attitude angle for changing the thickness of the porous bushing.

Different eccentricities produced different magnitudes of pressure. Figure 4-10 showed the lack of a direct correlation between an incremental increase in the thickness of the porous bushing and the increase in maximum pressure within the fluid film. The curves' qualitative behavior was comparable in this

demonstration because of the difference in magnitudes. However, it was evident in all cases that the increase from 0.1r to 0.2r caused a more significant increase in pressure than the increase at any other step.

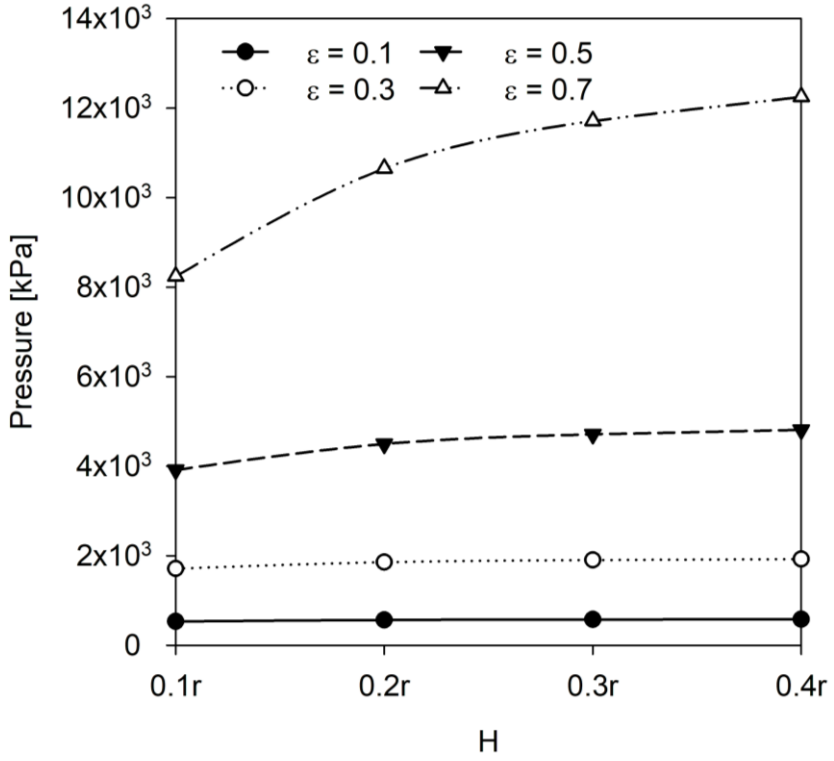

Figure 4-10: Maximum pressure values for various bushing thicknesses.

4.3 Isothermal Investigations with Pseudo Cavitation

4.3.1 Comparison of cavitation models

This section investigated the effect of including pseudo cavitation compared to Gumbel cavitation. For all settings investigated, the Reynolds number was 385.12. Following Szizi [79], this value indicates a laminar flow of

the working fluid since it is below the threshold of 2000. The model settings and bearing parameters used in comparing the models are given in Table 4-4. The passive reservoir used for the pseudo cavitation scenarios is that of Figure 2-2 which represents the pressure distribution of a shallow reservoir.

Table 4-4: Isothermal model settings for self-circulating bearing with

Bearing Specifications	
Length [mm]	38.1
Radius [mm]	12.426
Clearance (C) [mm]	0.0254
Eccentricity (ε)	0.1, 0.3, 0.5, 0.7 and 0.9
Rotational Velocity (ω) [RPM]	3,000
Material Properties of Oil and Air	
Oil Density (ρ_L) [$\frac{\text{kg}}{\text{m}^3}$]	840.724
Air Density for initial bubble size (ρ_{G0}) [$\frac{\text{kg}}{\text{m}^3}$]	0.9996
Oil Viscosity (μ_L) [Pa · s]	.00689
Air Viscosity (μ_G) [Pa · s]	2.12076x10^{-5}
Porous Bushing Settings	
Permeability [m^2]	5x10^{-13}
Thickness of the Bushing [m]	0.1*r
Passive Reservoir Representation [Pa]	Circumferential Variation 10^4
Cavitation Model	
Dilatational Viscosity (κ^s) [Ns/m]	$3.75 \cdot 10^{-3}$
Characteristic Bubble Radius [m]	$2 \cdot 10^{-5}$
Initial Void Fraction (α_{init})	0.01

In Figure 4-11, the load capacity of the bearing was calculated by integrating the pressure across the fluid film within the bearing. The circles mark the Gumbel cavitation model results, and the triangles represent the pseudo

cavitation results. The load for the Gumbel cavitation was higher, particularly as the eccentricity increased, compared to the load capacity for the model with pseudo cavitation. Gumbel cavitation assumed that the fluid could not support tensile stress. Tensile stress within the fluid presented as pressure below atmospheric; Gumbel cavitation set these pressures to zero (atmospheric) so the load capacity was expected to be less for a pseudo-cavitation model, which allowed for tensile stresses within the fluid. The pseudo-cavitation model was more physically accurate as Temperly's experiments showed that fluid can support tensile stresses [38].

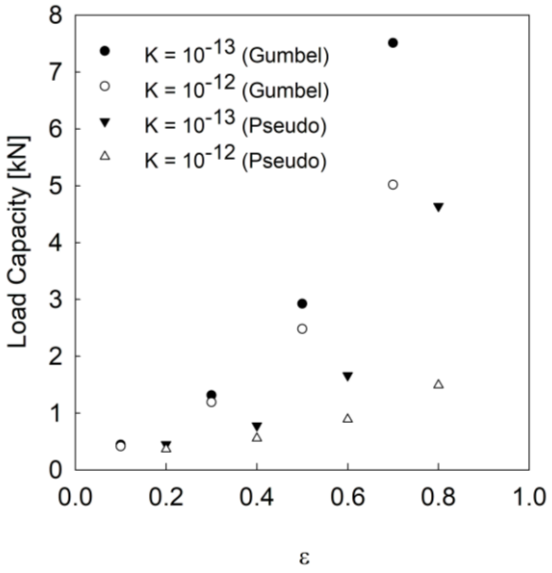

Figure 4-11: Load capacity for changing permeability for each cavitation model.

As the attitude angle increased, the stability of the bearing decreased [64]. With increased eccentricity, the disparity between the stability of the bearing from

each model grows. The pseudo cavitation model returned a larger attitude angle and the delta between the models grew as the eccentricity increased (Figure 4-12). At an eccentricity of 0.5 or lower, the change in the cavitation model does not affect the attitude angle. With an increased attitude angle, it is predicted that a decrease in bearing stability accompanied the pseudo cavitation model. Stability information is important in designing a bearing and the improved cavitation model will more accurately predict the stability.

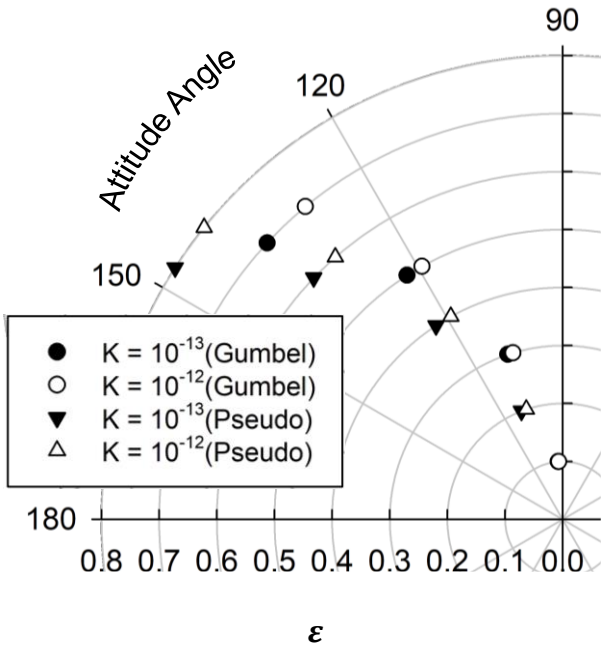

Figure 4-12: Attitude angle for changing permeability for each cavitation model.

Figures 4-13 and 4-14 reinforced the conclusions from the permeability variation in load and stability. The pseudo cavitation model predicted less load capacity and a larger attitude angle at each setting. As the eccentricity increased, the difference in the model predictions increased which indicated an increase in

the cavitation of the fluid at larger eccentricities. In addition to increasing with permeability, the model deltas increased as the thickness of the porous bushing increased. Conversely, the difference in model outputs of attitude angle remained approximately constant for different porous bushing thicknesses (Figure 4-14).

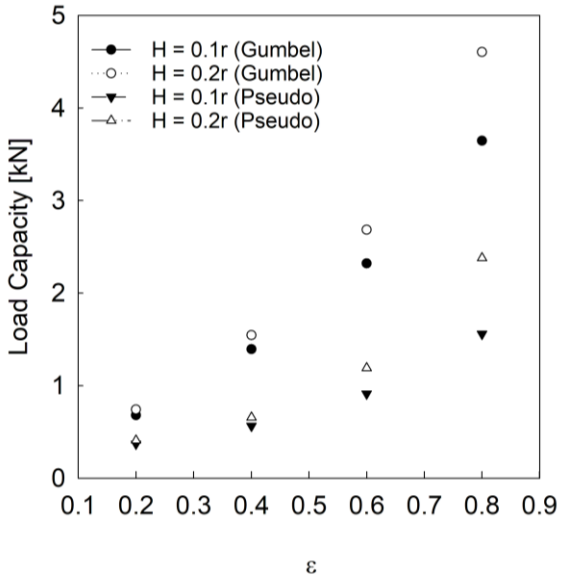

Figure 4-13: Load capacity for changing thickness for each cavitation model.

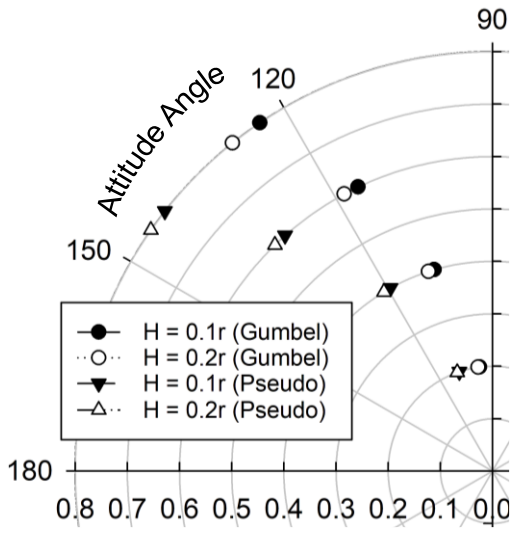

Figure 4-14: Attitude angle comparison of each cavitation model with different bushing thickness.

Inclusion of pseudo cavitation demonstrated the importance of accounting for the tension fluid can withstand and provided a more accurate prediction of the bearing's load capacity. The overall trends remained qualitatively the same because the behavior of the pressure within the bearing was not significantly altered. At lower eccentricities, where the pressure drop from the convergent to divergent region was less, the difference between the models lessened as expected, since there is less cavitation (fluid rupture).

4.3.2 Effect of changing permeability

The inclusion of tensile stresses and their magnitudes led to investigation of the midplane pressure distribution for various parameters. The results

demonstrated a larger effect for permeability variation than variation of the porous bushing thickness. The permeability represented a larger change in feeding parameter so it was expected that the results demonstrated a larger variation. The cavitation zone illuminated whether there was a relation between the feeding parameter and the cavitation zone. The results were analyzed for a low and high eccentricity bearing since they have demonstrated different behavior. The depth of the cavitation zone referred to the magnitude of the fluid film pressure while the width represented the circumferential length along the bearing exhibiting tensile stress.

For a high eccentricity bearing, the cavitation zone decreased in width and increased in depth when the permeability parameter decreased (Figure 4-15). Increasing the permeability reduced the magnitude of the positive and negative pressure peaks. With a lower eccentricity bearing, the results of the changing permeability were less significant. The increase in permeability advanced the cavitation into the convergent zone and narrowed the affected areas of the pressure curve. The high eccentricity bearing's midplane pressure (Figure 4-15b) was altered more by a permeability change than the low eccentricity bearing (Figure 4-15a) with the width and depth of the cavitation zone affected. The lack of change overall in the cavitation zone demonstrated that changing permeability would not be an effective way to reduce cavitation within the bearing.

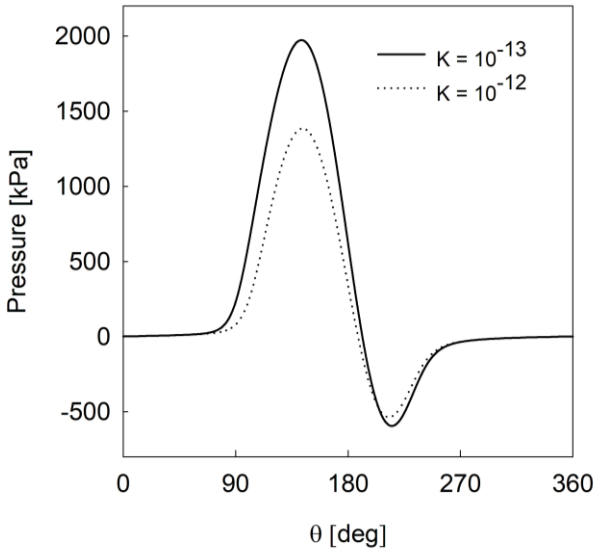

(a)

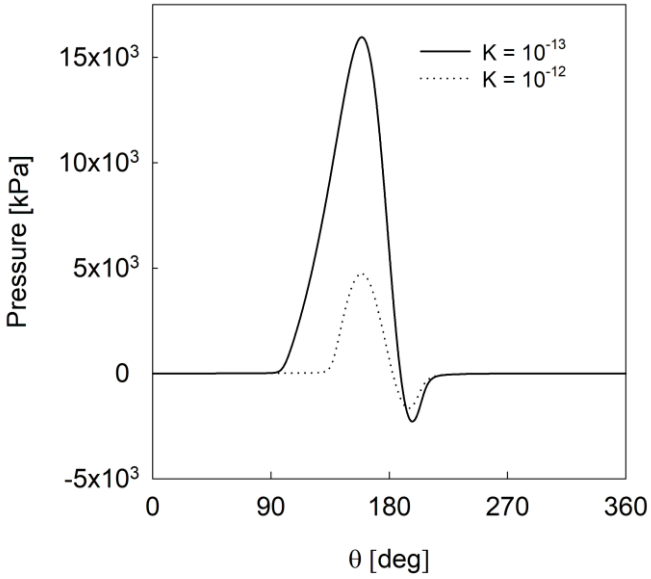

(b)

Figure 4-15: Midplane pressure curves to investigate the cavitation zone for changing permeability in (a) low and (b) high eccentricity bearings.

4.3.2 Effect of changing thickness

As the porous bushing thickness increased, the flow path from the reservoir to the bearing clearance became more challenging. 3D flow and uniform permeability allowed flow to go in the axial and circumferential directions as well as the radial. The pressure differential between the fluid film and the reservoir controlled the inclination of fluid to flow in the radial direction, as the boundary conditions in the axial and circumferential directions were constant. Due to the 3D flow, a thicker porous bushing was expected to have the lowest injection velocity, leading to a lower pressure and thus load capacity. The opposite results were obtained for a high eccentricity bearing (Figure 4-16b). As the porous bushing thickness decreased, the midplane pressure increased. This indicated that the reservoir pressure was lower than the fluid film pressure which caused fluid to flow out of the clearance more than into the clearance. With this scenario, the restriction to radial flow through the porous bushing kept more fluid in the clearance zone which created a higher pressure and load capacity. The cavitation zone advanced into the convergent zone in the plots of Figure 4-16c and d as the porous bushing thickness decreased. The void fraction being larger than zero indicated that the bubble size was larger than the initial kernel. Comparison of Figure 4-16c and 4-16d demonstrated that a higher eccentricity led to larger bubbles (higher void fraction) and a larger cavitation area. The sub-cavity pressures remained approximately equal for all porous bushing thicknesses (Figure 4-16a, b). A low eccentricity bearing was plotted in Figure

4-16a and was less affected by changing porous bushing thickness than the high eccentricity bearing (Figure 4-16b). The same trends at a different magnitude are shown in Figure 4-16a compared to Figure 4-16b.

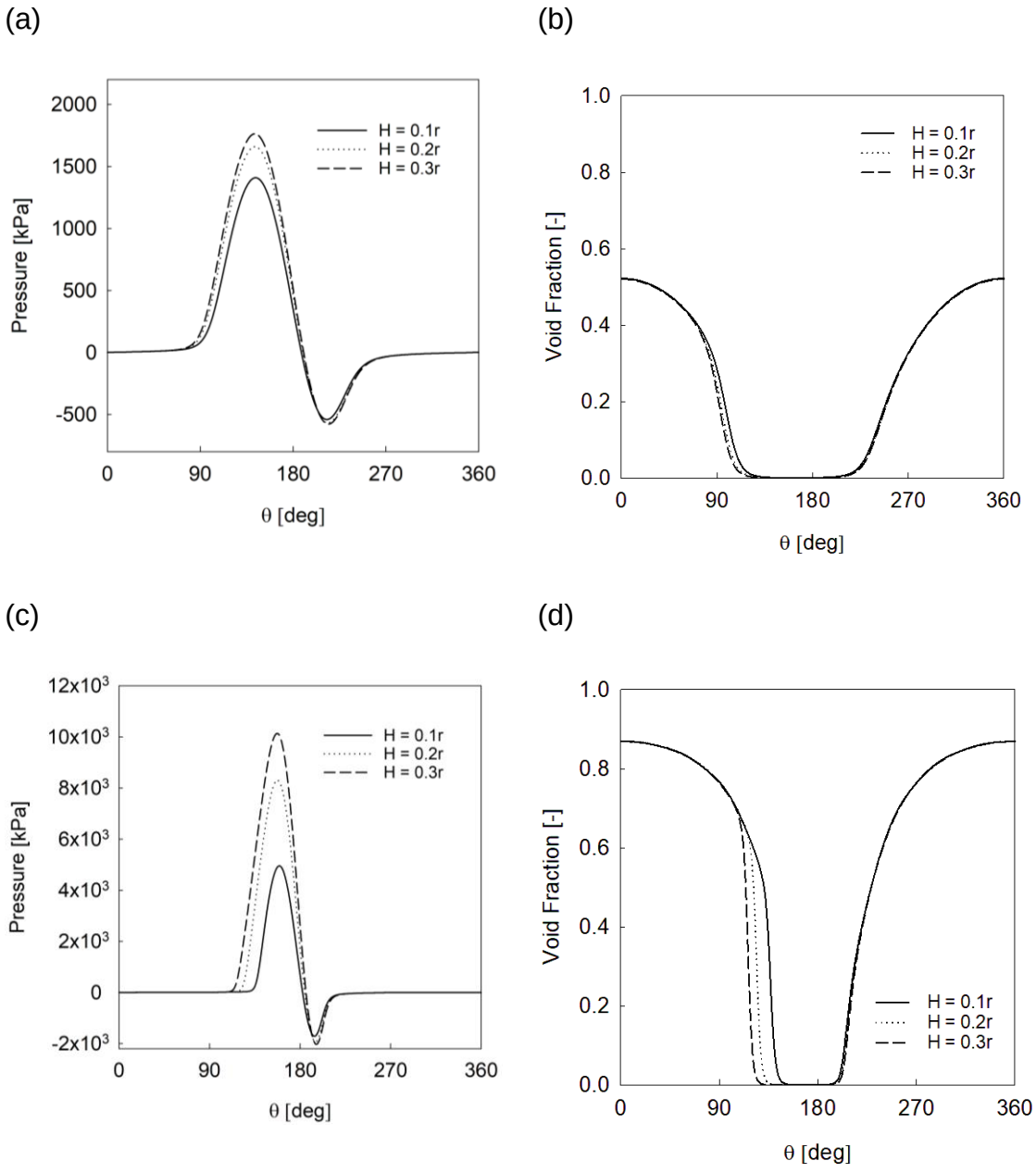

Figure 4-16: Midplane pressure and void curves to investigate the cavitation zone for changing thickness in (a, c) low and (b, d) high eccentricity bearings.

The void fraction had minimal changes for changing porous bushing thickness (Figure 4-16). However, Figure 4-17 demonstrates a large change in void fraction for changing eccentricity at the same busing thickness. It has been demonstrated that changing eccentricity caused a change in the midplane pressure in the previous figures; Figure 4-17 confirmed this pressure change affects the void fraction as well. Not only did the magnitude of the void fraction change, but the cavitation area significantly expanded as the eccentricity increased. The cavitation zone increased from 270-90º, representing half the bearing and the divergent region to ~200-135º for an eccentricity of 0.8. Similar to the pressure, the cavitation was more greatly affected by a change in eccentricity than a change in feeding parameter, specifically the change in bushing thickness.

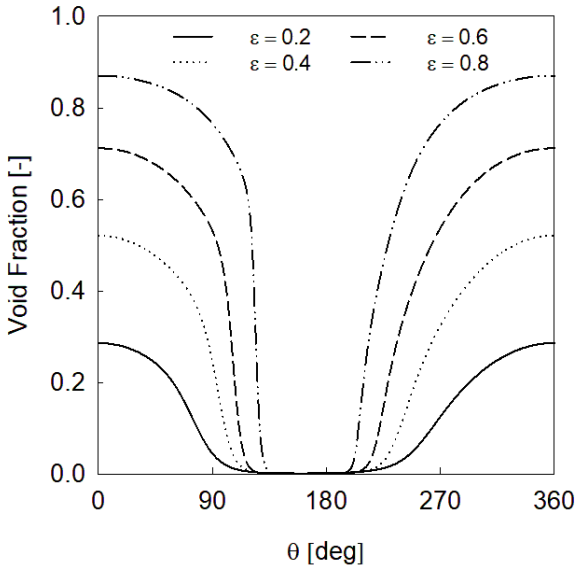

Figure 4-17: Midplane void fraction curves for varying eccentricity at a bushing thickness of 0.2r.

4.3.3 Effect of changing speed

Depending on the application, bearing speed can vary and create higher loads. The speed parameter was varied from 1000, 5000, and 10,000 rpm, which resulted in a clearance-based Reynolds number of 38.51, 192.56, and 385.12, respectively (Equation 2.45). As the bearing speed increased, the maximum pressure increased significantly for the low and high eccentricity bearing (Figure 4-18a, b respectively). The trends for changing speed remained qualitatively similar for the high and low eccentricity bearings (unlike with changing feeding parameter). In Figure 4-18, the cavitation zone was continually pushed into the convergent zone as the speed increased. The increased velocity delaying the increase in pressure due to pushing the cavitation zone into the convergent zone was earlier shown for a solid bearing in Snyder et al. [64]. The effect of increasing speed shown for a solid bearing [64] was also replicated for the self-circulating bearing of Figure 4-18.

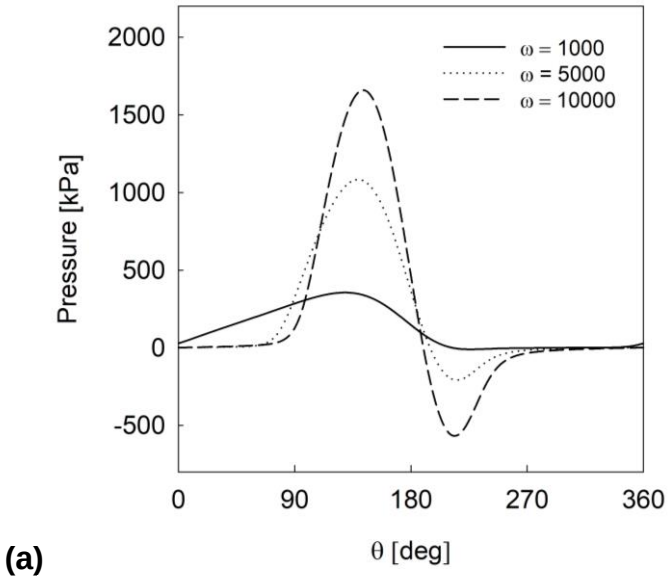

(a)

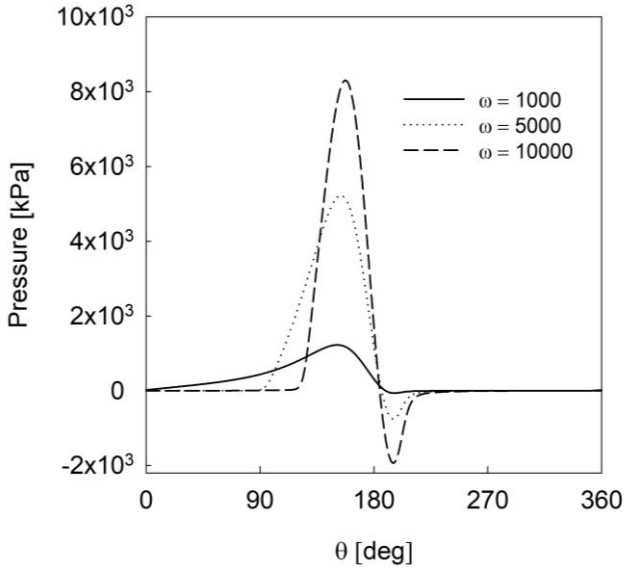

(b)

Figure 4-18: Midplane pressure curves to investigate the cavitation zone for changing speed in (a) low and (b) high eccentricity bearings.

The plot of Figure 4-19 demonstrated that as speed increased, the bearing's load capacity and attitude angle increased. For all changing

parameters, eccentricity and load capacity displayed an exponential relationship. Changing the speed created a larger change in load capacity (Figure 4-19) than did changing the feeding parameter (Figure 4-11, Figure 4-13). The sub-cavity pressures decreased more with speed than with altering the feeding parameter (Figure 4-15 and 4-16). Cavitation appeared to be more dependent on the Reynolds number than the feeding parameter since the changes to the cavitation zone were larger for changing speed than bushing permeability or bushing thickness. The attitude angle results for the parametric studies were similar (Figure 4-12, 4-14 and 4-18), where the high eccentricity, low load scenario showed an attitude of ~125º and the high eccentricity, high load scenario returned an attitude angle of ~145º. The semi-circle curve that connected the low eccentricity attitude angles to the high eccentricity attitude angle results indicated that the attitude angle was unaffected by the changing cavitation zone.

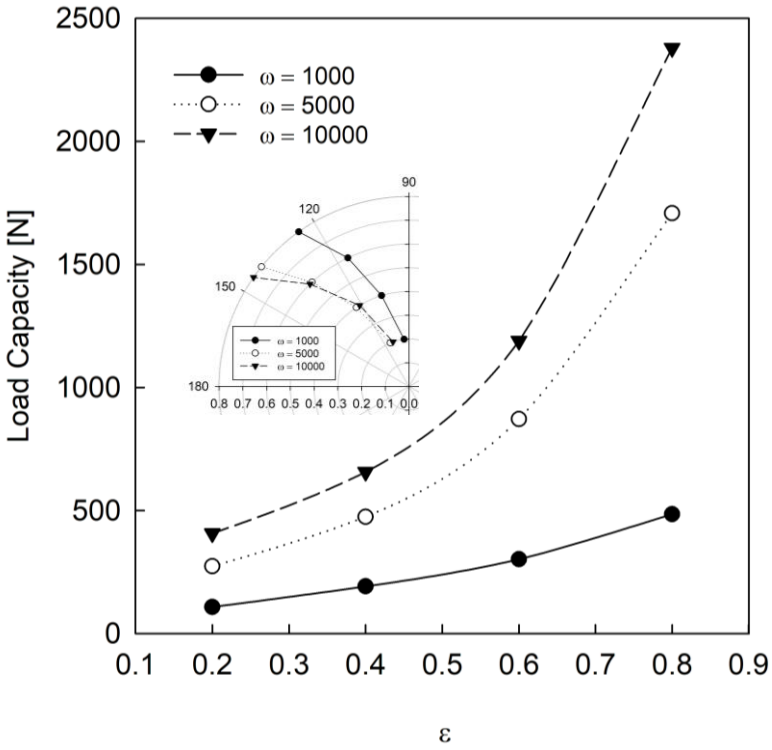

Figure 4-19: Load and stability investigation for changing speed with pseudo cavitation considered.

As speed is increased, the load capacity of the bearing increased. With increased speed, the attitude angle increased in Figure 4-18. This normal and tangential forces ratio representation demonstrated that less stability was obtained with a faster bearing and larger load capacity. The comparison of the effect of permeability, thickness, and speed demonstrated that speed has a much more significant effect on the load capacity of the bearing.

4.4 Thermal investigations

After exiting the fluid film, the temperature and properties of the lubricant remained constant through the bushing, which would not be the case in application. The porous bushing, acting as a heat exchanger, would have a temperature gradient within the bushing that would alter the lubricant properties within. The thickness of the porous bushing was kept thin to negate the effect of the assumption of constant bushing temperature and lubricant properties. The settings in Table 4-4 allowed for investigation of the effect of a self-circulating bearing on the temperature, cavitation, and load compared to a solid journal bearing. Sutherland's law, Equation 3-50, was used to update the lubricant properties from temperature changes.

Table 4-5: Model settings for a thermal model with pseudo cavitation.

Bearing Specifications	
Length [mm]	25.4
Radius [mm]	25.4
Clearance (C) [mm]	0.0254
Eccentricity (ε)	0.2, 0.4, 0.6 and 0.8
Rotational Velocity (ω) [RPM]	5000
Material Properties of Oil and Air	
Oil Density (ρ_L) [$\frac{\mathrm{kg}}{\mathrm{m}^3}$]	840.724
Air Density for initial bubble size (ρ_{G0}) [$\frac{\mathrm{kg}}{\mathrm{m}^3}$]	0.9996
Oil Viscosity (μ_L) [$\mathrm{Pa} \cdot \mathrm{s}$]	.00689
Air Viscosity (μ_G) [$\mathrm{Pa} \cdot \mathrm{s}$]	$2.12 \cdot 10^{-5}$
Cavitation Model Settings	
Dilatational Viscosity (κ^s) [Ns/m]	$3.75 \cdot 10^{-3}$
Characteristic Bubble Radius [m]	$2 \cdot 10^{-5}$
Initial Void Fraction (α_{init})	0.01
Porous Bushing Settings	
Permeability [m^2]	$1 \cdot 10^{-12}$
Thickness of the Bushing [m]	$0.2 \cdot r$
Passive Reservoir Representation [Pa]	Circumferential Variation 10^4
Thermal Model Settings	
Heat Transfer Coefficient bushing and shaft [$\frac{W}{m^2 ℃}$]	100

4.4.1 Solid bearing vs self-circulating bearing

Lubricant supply to the fluid film clearance is important for temperature control. The advantage of the self-circulating bearing is that an external pumping system is not needed. To demonstrate the significant temperature advantage of the self-circulating bearing compared to a solid journal bearing, Figure 4-20 contoured the temperature distribution of the lubricant for a solid bearing (Figure 4-20a) and a self-circulating bearing (Figure 4-20b). Figure 4-20a exhibited a maximum temperature of 123ºC while the self-circulating bearing's highest temperature was 85ºC. This was a clear demonstration that the self-circulating bearing was successful in keeping lubricant temperatures lower than a traditional system without feeding ports. The highest temperature occurred at the minimum clearance point in both bearings (~180º). The ambient temperature of 80℃ was the axial boundary condition for both numerical simulations and was minimally present in the solid bearing compared to the self-circulating bearing.

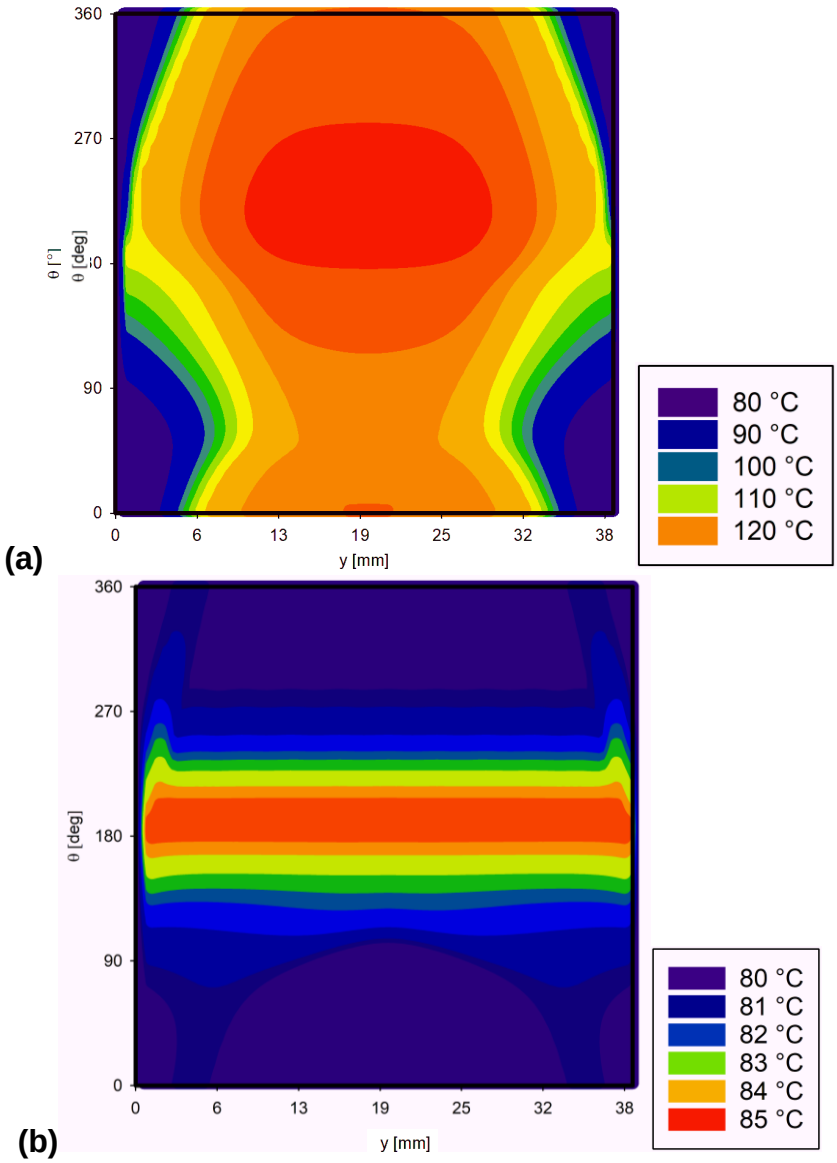

Figure 4-20: Temperature contours for (a) solid and (b) self-circulating bearing.

Figure 4-20 demonstrated that there was a lower temperature within the self-circulating bearing. Thermal management is the second advantage of a self-

circulating bearing, behind the elimination of the external pumping system for fluid delivery. Figure 4-21 further investigated the fluid behavior within a solid and self-circulating bearing for the high eccentricity case of Figure 4-20. The maximum and minimum values of the void fraction remained the same, however the cavitation region was larger in the self-circulating bearing. The high-pressure region was narrower in the self-circulating bearing compared to the solid bearing, which agreed with the cavitation zone extending into the converging region of the bearing. The change in behavior of the pressure and void fraction are symptoms of the pressure driven injection velocity.

While an increase in temperature would encourage an increase in void fraction through a decrease in dynamic viscosity, Figure 4-21 demonstrated that the effect of the fluid pressure had a larger effect on the void fraction. Readers are reminded that the effect of temperature on the fluid properties was accounted for in Sutherland's law which would adjust the viscosity of the liquid. The solid bearing had a larger midplane pressure earlier in the convergent region which caused the void fraction to decrease earlier in the convergent region than in the self-circulating bearing. The bubble theory utilized the bubble pressure and surrounding fluid pressure in addition to the viscosity to determine whether the bubble would grow or shrink. The results of Figure 4-21 are consistent with the order of magnitude analysis conducted by Pierson which demonstrated that the dynamic viscosity was minimal compared to the pressure differential and surface dilatation terms in the Rayleigh-Plesset-Scriven equation [62].

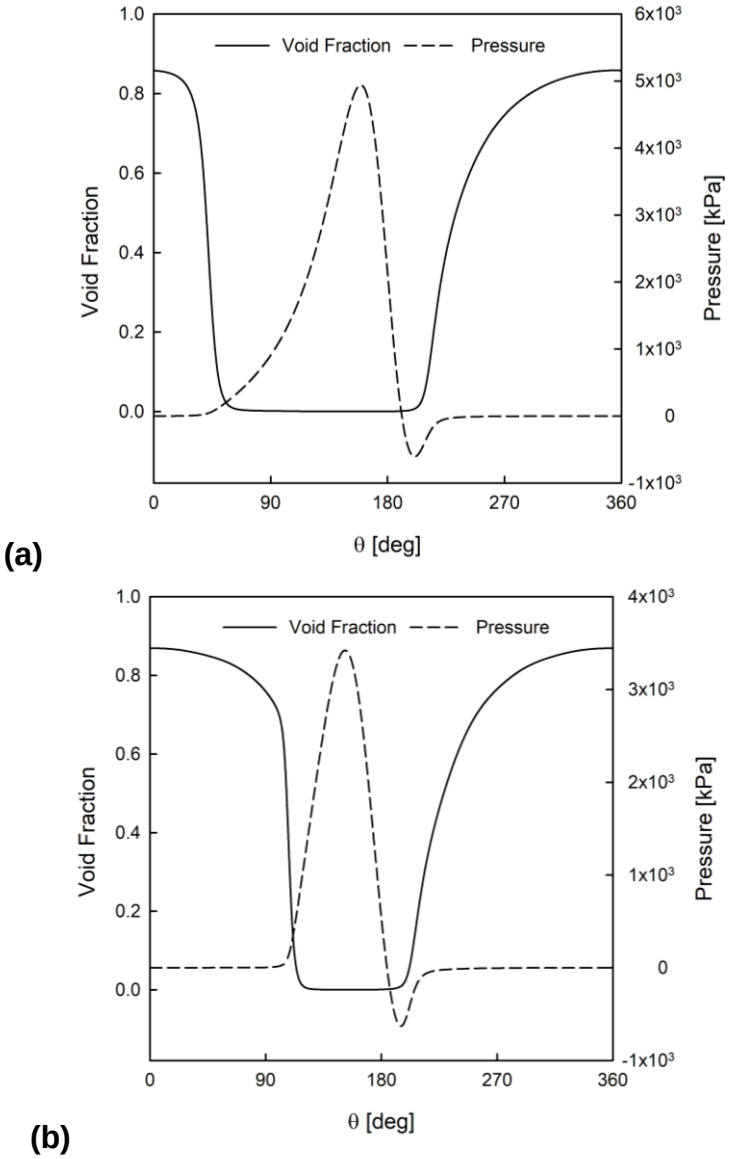

Figure 4-21: Midplane void fraction and pressure comparison for a solid (a) and self-circulating (b) bearing with pseudo cavitation.

Figure 4-22 demonstrated a load comparison for a self-circulating and solid journal bearing. The speed was moderate at 5000 rpm and the self-circulating bearing had a porous bushing with a permeability of $1 \text{ x } 10^{-12} \text{ m}^2$. The solid bearing maintained a larger load capacity at all eccentricities, although the difference was less than 20% for 0.2 and 0.4 eccentricity cases. At 0.6 and 0.8 the load carrying capacity differed by 25 and 36% respectively. The attitude angle for both bearings was similar for all eccentricities. While these results may differ with a scenario where more self-circulation occurs, these results demonstrated that there is little cost to the benefit and simplification a self-circulating bearing brings to applications.

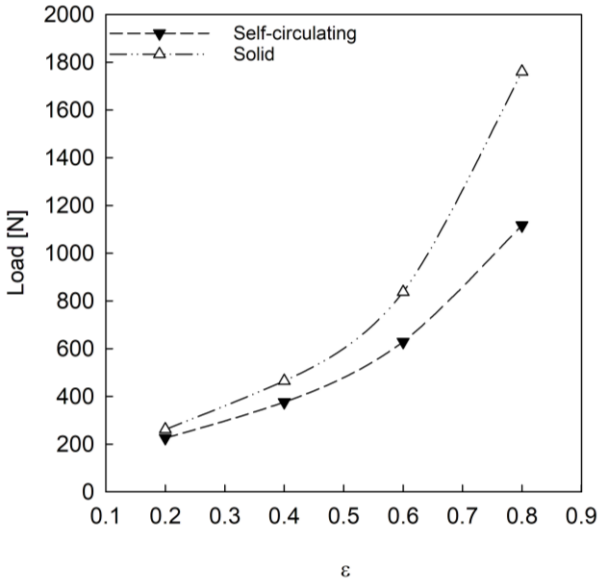

Figure 4-22: Load comparison for a solid and self-circulating bearing with pseudo cavitation with thermal considerations.

CHAPTER V

CONCLUSIONS

This study confirmed the theory and potential operation of a self-circulating bearing. A self-circulating bearing will improve the life expectancy of bearings in complex installations where they are difficult to monitor and replace. The tribological system used the pressure differentials to circulate fluid between the bearing clearance and a passive reservoir. The numerical model utilized an analytical solution for the three-dimensional flow within the porous bushing and accounted for pseudo-cavitation within the fluid film. The flow through the porous bushing and cavitation model were independently characterized with published experimental results. The low permeability range and passive reservoir representation of a shallow reservoir were selected based on previous investigation results [67,78]. The model evaluated the effects on bearing load capacity and attitude angle within a parametric study of porous bushing thickness, permeability, and speed in addition to the evaluation of a pseudo-cavitation model. A thin film energy equation was then incorporated to demonstrate the effects of the self-circulation on the cavitation and temperature of the fluid film.

The increased complexity of the 3D representation of the porous bushing improved the representation of the injection velocity for approximately 30% of the bearing's length. With Gumbel cavitation, which does not permit tensile stress of the lubricant, the effect of the porous bushing thickness and permeability on the self-circulating bearing's injection velocity and bearing load capacity were explored. As shown in Figure 4-3, porous bushing thicknesses of 0.2r or greater were needed to generate an injection velocity large enough to exchange fluid between the clearance and passive reservoir to promote self-circulation. For the permeabilities plotted in Figure 4-2, none were significantly large to obtain an injection velocity greater than 10^{-3}. There was a linear relationship between the maximum pressure and the bushing permeability, particularly for a high eccentricity bearing. Increasing the permeability parameter caused an increase in bearing load capacity as well as an increase in stability. Increasing the porous bushing thickness decreased the bearing load capacity, as expected when 3D flow is permitted throughout the bushing.

The comparison of a Gumbel and pseudo cavitation model showed that the trends for changing parameters remain the same for the inclusion of fluid tension (pseudo cavitation). For both models, a decrease in permeability increased the load capacity. An increase in the bushing thickness also resulted in an increased load capacity for both models. Whether by increasing permeability or decreasing bushing thickness, a decrease in feeding parameter resulted in an increase in attitude angle.

The cavitation zone, represented by the void fraction, was observed for changing parameters. Comparing a low and high eccentricity bearing demonstrated that a higher eccentricity led to larger void fractions and a larger cavitation area. In contrast, changing the bushing thickness had minimal effect on the cavitation field. Changing permeability did have an effect on the tensile pressure of the fluid but again was minimal compared to an eccentricity change. In addition to eccentricity, speed also had a large effect on the bearing's cavitation zone which led to large fluctuations in the load capacity for different speeds. A higher speed led to larger positive and negative pressures while maintaining an increased load capacity compared to lower speeds.

Application of the thin film energy equation allowed for a temperature comparison of the models. Sutherland's law was used to update lubricant properties due to changes in temperature. The solid bearing had temperatures exceeding 120ºF while the self-circulating bearing barely exceeded the atmospheric temperature of 80ºF. The cavitation zone was affected by the self-circulating bearing, the area of cavitation was increased. The self-circulating bearing cavitation zone pushed into the convergent region of the bearing which was not seen in the solid bearing. It was shown that the load capacity was greater for the solid bearing than for the self-circulating bearing, but the attitude angles were similar.

Self-circulating bearings will prolong life expectancy for bearings in installations where monitoring and repairs are difficult. Self-circulating bearings also improved the thermal management compared to a solid bearing. The model

developed will allow for more accurate predictions of self-circulating performance which improves the design process and eventual performance of bearings in application. In comparison to a solid bearing, there was only a slight loss in bearing load carrying capacity which could be mitigated with changes to the permeability, bushing thickness, or the reservoir pressure.

BIBLIOGRAPHY

[1] Jiayu G., Kun L., Yong Z., Fanming M., Thermal-elastohydrodynamic lubrication study of misaligned journal bearing in wind turbine gearbox, Tribology International, Volume 188,2023,108887,ISSN 0301679X, doi:10.1016/j.triboint.2023.108887.

[2] Balasoiu, A. M., Braun, M. J., & Moldovan, S. I. (2013). A parametric study of a porous self-circulating hydrodynamic bearing. Tribology International, 61, 176–193. doi:10.1016/j.triboint.2012.12.015

[3] Braun, M., Balasoiu, A., Moldovan, S., Young, G., Johnston, J. (2008). Self-acting self-circulating fluid system without external pressure source and use in bearing system. (U.S. Patent No. US8453665B2). U.S. Patent and Trademark Office.

[4] Scheidegger, A. E. (1963). *The physics of flow through porous media.* University of Toledo Press.

[5] Bear. J. (1988). *Dynamics of fluids in porous media.* Dover Publications, Inc.

[6] Van Buuren, S. W., Hetzler, H., Hinterkausen, M., & Seemann, W. (2012). Novel approach to solve the dynamical porous journal bearing problem. Tribology International, 46(1), 30–40. doi:10.1016/j.triboint.2011.03.017

[7] Boubendir, S., Larbi, S., & Bennacer, R. (2010). *A Contribution to the Analysis of the Thermo-Hydrodynamic Lubrication of Porous Self-Lubricating Journal Bearings. Defect and Diffusion Forum, 297-301, 618–623.* doi:10.4028/www.scientific.net/ddf.297-301.618

[8] Johnston, J. D., Braun, M. J., & Young, G. W. (2007). Modeling a Porous Slider Bearing With an External Reservoir. ASME/STLE 2007 International Joint Tribology Conference, Parts A and B. doi:10.1115/ijtc2007-44299

[9] Cameron, A., Morgan, V. T., & Stainsby, A. E. (1962). Critical conditions for hydrodynamic lubrication of porous metal bearings. Lubrication and Wear Group, 176(28), 761-770. 10.1243/PIME_PROC_1962_176_061_02

[10] Rhodes, C. A., & Rouleau, W. T. (1965) Hydrodynamic lubrication of narrow porous metal bearings with sealed ends. Wear, 8(6), 474-486. doi:10.1016/0043-1648(65)90140-7

[11] Shir, C. C., &Joseph, D. D. (1966). Lubrication of a Porous Bearing-Reynolds' Solution. Journal of Applied Mechanics, 33(4), 761. Doi: 10.1115?1.3625179

[12] Murti, P. R. K. (1971). Hydrodynamic lubrication of long porous bearings. *Wear,* 18(6), 449–460. doi:10.1016/0043-1648(71)90169-4

[13] Cusano, C. (1972). Lubrication of Porous Journal Bearings. Journal of Lubrication Technology, 94(1), 69. doi:10.1115/1.3451638

[14] Neale, G., & Nader, W. (1974). Practical significance of brinkman's extension of darcy's law: Coupled parallel flows within a channel and a bounding

porous medium. *The Canadian Journal of Chemical Engineering, 52(4), 475–478.* doi:10.1002/cjce.5450520407

[15] Lin JR, Hwang CC. Lubrication of short porous journal bearings- Use of the Brinkman-extended Darcy model. Wear 1993;161:93–104

[16] Rouleau, W. T. (1963). Hydrodynamic Lubrication of Narrow Pressure Fitted Porous Metal Bearings. Journal of Basic Engineering, 123-128.

[17] Cieslicki, K. (1993). Investigations of the effect of inertia on flow of air through porous bearing sleeves. *Wear,* 172(1), 73-78.

[18] Hwang, C. C., Lin, J.R., & Yang, R. F. (1996). Lubrication of Long Porous Slider Bearings (Use of the Brinkman-Extended Darcy Model). *JSME International Journal,* Series B, 39(1), 141-148.

[19] Neale, G., & Nader, W. (1974). Practical significance of brinkman's extension of darcy's law: Coupled parallel flows within a channel and a bounding porous medium. *The Canadian Journal of Chemical Engineering, 52(4), 475–478.* doi:10.1002/cjce.5450520407

[20] Beavers, G. S., & Joseph, D. D. (1967). Boundary conditions at a naturally permeable wall. *Journal of Fluid Mechanics*, 30(01), 197. doi:10.1017/s0022112067001375

[21] Elsharkawy, A. A. and Guedouar, L. H. (2001). Hydrodynamic lubrication of porous journal bearings using a modified brinkman-extended darcy model. *Tribology International*, 34, 767-777.doi:10.1016/s0301-679x(01)00070-6

[22] Cusano, C. (1972). Lubrication of Porous Journal Bearings. *Journal of Lubrication Technology*, 94(1), 69. doi:10.1115/1.3451638

[23] Murti, P. R. K. (1971). Hydrodynamic lubrication of long porous bearings. *Wear,* 18(6), 449–460. doi:10.1016/0043-1648(71)90169-4

[24] Li, W.L., & Chun, H. -M. (2004). Modified Reynolds equation for coupled stress fluids: a porous media model. *Acta Mechanica,* 174(3-4), 189-202. doi: 10.1007/s00707-004-0123-0

[25] Li, W.-L., & Chun, H. -M. (2004). Modified Reynolds equation for coupled stress fluids: a porous media model. *Acta Mechanica,* 174(3-4), 189-202. doi: 10.1007/s00707-004-0123-0

[26] Li, W. L., (1999). Derivation of modified reynolds equation-a porous media model. *Journal of Tribology,* 121, 823-829.

[27] Elsharkawy, A.A. (2005) Effects of lubricant additives on the performance of hydrodynamically lubricated journal bearings. *Tribol Lett* 18, 63–73. https://doi.org/10.1007/s11249-004-1758-7

[28] Rhodes, C. A., & Rouleau, W. T. (1965) Hydrodynamic lubrication of narrow porous metal bearings with sealed ends. Wear*,* 8(6), 474-486. doi:10.1016/0043-1648(65)90140-7

[29] Rouleau, W. T., & Steiner, L. I. (1974). Hydrodynamic Porous Journal Bearings. Part I—Finite Full Bearings. *Journal of Lubrication Technology*, 96(3), 346. doi:10.1115/1.3451962

[30] Kaneko, S., Ohkawa, Y., & Hashimoto, Y. (1994). A study of the mechanism of lubrication in porous journal bearings: effects of dimensionless oil-feed pressure on static characteristics under hydrodynamic lubrication conditions. *Journal of Tribology,*116, 606-611.

[301] Kaneko, S., Hashimoto, Y., & I, H. (1997). Analysis of Oil-Film Pressure Distribution in Porous Journal Bearings Under Hydrodynamic Lubrication Conditions Using an Improved Boundary Condition. Journal of Tribology*, 119(1), 171.* doi:10.1115/1.2832454

[32] Meurisse, M.H. & Giudicelli, B. (1999) A 3D conservative model for self-lubricated porous journal bearings in a hydrodynamic steady state. Journal of Tribology, 121, 529-537.

[33] Lee, C.-C., & You, H.-I. (2009). Characteristics of Externally Pressurized Porous Gas Bearings Considering Structure Permeability*. Tribology Transactions, 52(6), 768–776.* doi:10.1080/10402000903097403

[34] Majumdar, B.C. (1978). Analytical solution of externally pressurized porous gas journal bearings. Journal of Lubrication Technology-Transactions of the ASME, 100,3,442-444. doi:10.1115/1.3453205

[35] Sun, D. (1973). Stability Analysis of an Externally Pressurized Gas-Lubricated Porous Thrust Bearing. ASME. *J. of Lubrication Tech*. October 1973; 95(4): 457–468. https://doi.org/10.1115/1.3451857

[36] Reynolds, O. On the internal cohesion of liquids and the suspension of a column of mercury to a height more than double that of the barometer.

Manchester Literary and Phil. Soc. Proc (and Manchester Literary and Phil. Soc. Memoirs), 1878 (and 1882), 17 (and 7), 159–175 (and 1– 19).

[37] Sommerfeld, A. Zur hydrodynamische theorie der schmiermittelreibung. Zeit Math. Phys., 1904, 50, 97– 155.

[38] Temperley H, The tensile strength of liquids. In: Proceedings of the 1st LeedsLyon symposium on tribology, cavitation and related phenomena in lubrication. London; 1974.

[39] Bertholet, M. Sur quelques phenomenes de dilation forcée des liquides. Ann Chim Phys 1850;30:232–5.

[40] Fisher, J.C. The fracture of liquids. J. Appl. Phys. 1948;19(11):1062-7

[41] Natsumeda, S. and Someya, T. Paper III(ii) Negative pressures in statically and dynamically loaded journal bearings. In: Proceedings of the 13th Leeds–Lyon symposium of tribology. Leeds: UK; 1987. p. 498–505.

[42] Adiletta G, Della Pietra L. Experimental study of a squeeze film damper with eccentric circular orbits. J Tribol 2006;128(April):365–77.

[43] Braun M, Hannon W. Cavitation formation and modelling for fluid film bearings: a review. Proc Inst Mech Eng J Eng Tribol 2010;224(9):839–63.

[44] Hendricks RC, Mullen RL and Braun MJ, Analogy between cavitation and fracture mechanics. In: Proceedings of the ASME/JSME thermal engineering conference, vol. 1; 1983. p. 35–43 (also NASA Lewis RC, TM 83071/1983 (26 pages).

[45] Floberg L. Sub-cavity pressures and number of oil streamers in cavitation egions with special reference to the infinite journal bearing. Acta Polytech Sc and Mech Eng Ser 1968;37(3):1–31.

[46] Floberg, L. Transactions of machine elements division. Lund, Sweden: Lund Technical University; 1973. p. 1–13.

[47] Gumbel, L., “Das Problem der Lagerreibung,” *Monatsblatter, Berliner Bezirks Verein Deutscher Ingenieure*, vol. 5, pp. 97--104 and 109--120, 1914.

[48] Swift, H.W. The stability of lubricating films in journal bearings. Proc Inst Civil Eng 1932;233:267–88.

[49] Stieber, W. Das schwimmlager: hydrodynamische theorie des gleitlagers. Berlin: V.D.I. Verlag GMBH; 1933.

[50] Brewe, D.E. Theoretical modeling of the vapor cavitation in dynamically loaded journal bearings. J Tribol 1986;108(4):628–38.

[51] Floberg, L. On hydrodynamic lubrication with special reference to sub-cavity pressures and number of streamers in cavitation regions. Acta Polytech Sc and Mech Eng Ser 1965;19:1–35.

[52] Elrod, H. G. “A Cavitation Algorithm,” *Journal of Lubrication Technology*, vol. 103, no. 3, p. 350, 1981.

[53] Vijayaraghavan, D., Keith, Jr TG. An efficient, robust, and time accurate numerical scheme applied to a cavitation algorithm. J Tribol 1990;112(1):44–51.

[54] Singhal, A. K., Athavale , M. M., Li , H., and Jiang, Y. (August 19, 2002). "Mathematical Basis and Validation of the Full Cavitation Model." ASME. *J. Fluids Eng*. September 2002; 124(3): 617-624. https://doi.org/10.1115/1.1486223

[55] Zwart P, Gerber A and Belamri T, A two-phase flow model for predicting cavitation dynamics. In: Proceedings of ICMF international conference on multiphase flow. Paper no. 152. Yokohama, Japan; May 30–June 3, 2004.

[56] Zhou, Hailun & Cao, Gangyi & Chen, Xi & Zhang, Yuqi & Cang, Yangguang. (2023). A Study on the Thermal Properties of Oil-Film Viscosity in Squeeze Film Dampers. Lubricants. 11. 163. 10.3390/lubricants11040163.

[57] Liu, Xu, Chen, X., Kang, R., Shen, X. & Ni, B. (2020). A Coupled Cavitation Model in An Oscillatory Oil Squeeze Film. Computer Modeling in Engineering & Sciences. 123. 129-152. 10.32604/cmes.2020.07836.

[58] Zuber, N., & Dougherty, D. E. (1982). *The Field Equations for Two-Phase Reynolds Film Flow with a Change of Phase. A S L E Transactions, 25(1), 108–116.* doi:10.1080/05698198208983072

[59] Natsumeda, S. and Someya, T., “Paper III(ii) Negative pressures in statically and dynamically loaded journal bearings,” in *Tribology Series*, vol. 11, no. C, 1987, pp. 65–72.

[60] Ida, T., Sugeya, T. Motion of air bubbles in mineral oils subject to sudden change in chamber pressure. Bull JSME 1980;23(181):1132–9.

[61] Someya, T. On the development of negative pressure in oil film and the

characteristics of journal bearing. Meccanica 2003;38:643–58.

[62] Pierson, K. C. (2019). *Multiphysics Cavitation Model with Application to the Dynamic Behavior of Journal Bearings* [Doctoral dissertation, University of Akron]. OhioLINK Electronic Theses and Dissertations Center. http://rave.ohiolink.edu/etdc/view?acc_num=akron1555440702757939

[63] Gehannin, J., Arghir, M., Bonneau, O. Complete squeeze film damper analysis

based on the bulk flow equations. Tribol Trans 2010;53:84–95.

[64] Snyder, T. A., Braun, M. J., and Pierson, K. C. “Two-way coupled Reynolds and Rayleigh-Plesset equations for a fully transient, multiphysics cavitation model with pseudo-cavitation,” *Tribology International*, vol. 93, pp. 429–445, 2016.

[65] Jaramillo, Alfredo & Bayada, Guy & CIUPERCA, IONEL & Jai, Mohammed. (2019). About a cavitation model including bubbles in thin film lubrication: A first mathematical analysis. European Journal of Applied Mathematics. 31. 1-26. 10.1017/S0956792519000287.

[66] Jaramillo, Alfredo & Buscaglia, Gustavo. (2017). A stable numerical strategy for Reynolds-Rayleigh-Plesset coupling. Tribology International. 130. 10.1016/j.triboint.2018.08.022.

[67] Balasoiu, A. M. (2012). *A Self-Circulating Porous Bearing with a Wrapped-Around Reservoir* [Doctoral dissertation, University of Akron]. OhioLINK Electronic Theses and Dissertations Center. http://rave.ohiolink.edu/etdc/view?acc_num=akron1354643325

[68] Poritsky, H., “The Collapse or Growth of a Spherical Bubble or Cavity in a Viscous Fluid,” in *Proceedings of the First U.S. National Conference of Applied Mechanics*, 1951, pp. 813–821.

[69] Plesset, M. S. “The Dynamics of Cavitation Bubbles,” *Journal of Applied Mechanics*, vol. 16, pp. 277–282, 1949

[70] Scriven, L. On the dynamics of the phase growth; letter to the editor. Chem Eng Sci 1962;17:55

[71] Edwards, D., Brenner, H. and Darsh, W., *Interfacial Transport Processes and Rheology*. Butterworth-Heinemann, 1991.

[72] Fukamatsu, T. “A Study on the Oil-film Pressure Distribution in Journal Bearing” (In Japanese), Musashi Institute of Technology, 1997.

[73] Someya, T. On the Development of Negative Pressure in Oil Film and the Characteristics of Journal Bearing. *Meccanica* **38**, 643–658 (2003). https://doi.org/10.1023/A:1025869006693

[74] White F. M., Viscous Fluid Flow. New York: McGraw- Hilll, 1974.

[75] Arpaci, V. S. (1996). *Conduction Heat Transfer.* Addison-Wesley Publishing Company.

[76] DeCamillo, S. and Fabijonas B., “Thrust Bearings,” in Handbook of Lubrication and Tribology: Volume II, 2nd ed., R. Bruce, Ed. Boca Raton: Taylor and Francis, 2012.

[77] Sutherland W., “LII. The viscosity of gases and molecular force,” The London, Edinburgh, and Dublin Philosophical Magazine and Journal of Science, vol. 36, no. 223, pp. 507–531, Dec. 1893.

[78] Clifford, E. J., Daniels, C.C. 2023. Numerical model of a Finite Porous Journal Bearing Considering Cavitation. Presented at the 2023 (77th Annual) STLE Annual Meeting & Exhibition, Long Beach, CA.

[79] Szeri, A., Tribology, friction, lubrication and wear, New York: Hemisphere Publishing Comp ., 1979, p. 236.

APPENDICES

APPENDIX A

MODIFIED REYNOLDS EQUATION DERIVATION

The modified Reynolds equation as used in this thesis is the widely used Reynolds equation altered to account for feeding of lubricant through an orifice. The derivation of the Reynolds' equation for use in this thesis begins with considering a differential element of the fluid positioned within two sliding surfaces. This element is depicted below in Figure A.1.

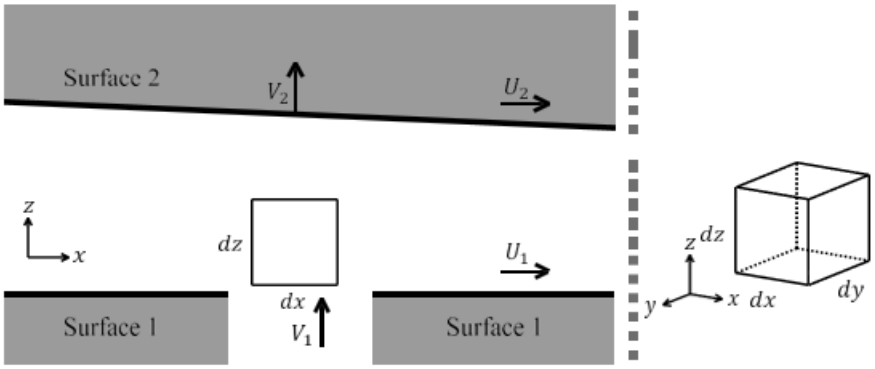

Figure A.1: The differential element between two sliding surfaces of the unwrapped bearing.

The momentum form of Reynolds Transport Theorem (RTT), Equation A.1, is considered for both the circumferential (x,φ) direction and axial (y, z) directions.

$$\sum F_x = \frac{d}{dt}\int_V (\rho u)dV + \int_S \rho u(\vec{v}\cdot\vec{n})dS \qquad \text{A.1}$$

$$\sum F_y = \frac{d}{dt}\int_V (\rho v)dV + \int_S \rho v(\vec{v}\cdot\vec{n})dS \qquad \text{A.2}$$

Inertial and Body forces will be neglected; Newton's second law then is simplified to a force balance of the pressure and considered shear force terms. Figure A.2A shows the x-direction forces and Figure A.2B shows the y-direction forces.

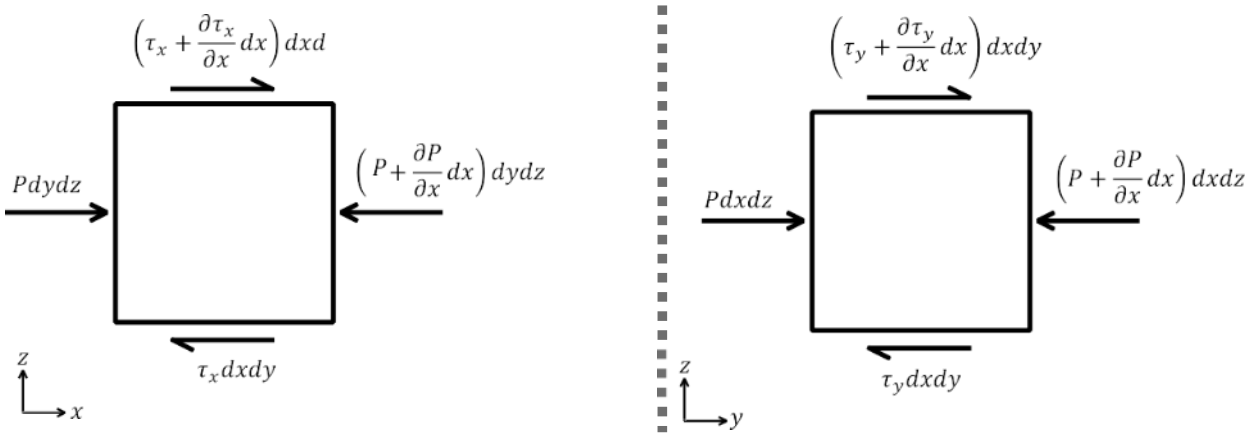

Figure A.2: Pressure and Shear Force balance on the differential element in the x-direction (A) and the y-direction (B).

The balance of the forces acting in the two directions results in equations A.2 and A.3.

$$\sum F_x = 0 = Pdydz - (P + \frac{\partial P}{\partial x}dx)dydz - \tau_x dxdy + \left(\tau_x + \frac{\partial \tau_x}{\partial z}dz\right)dxdy \qquad \text{A.2}$$

$$\sum F_y = 0 = Pdxdz - (P + \frac{\partial P}{\partial y}dy)dxdz - \tau_y dydz + \left(\tau_y + \frac{\partial \tau_y}{\partial z}dz\right)dxdy \qquad \text{A.3}$$

Assuming that the fluid is Newtonian, the shear terms above can be written in terms of the velocity gradient with the assumption of constant viscosity

across the gap (due to the relatively small distance h across the gap). After cancelling like terms and rearranging, equations A.2 and A.3 are simplified to equations A.4 and A.5.

$$\frac{\partial P}{\partial x} = \mu \frac{\partial^2 u}{\partial y^2} \quad \text{A.4}$$

$$\frac{\partial P}{\partial z} = \mu \frac{\partial^2 v}{\partial y^2} \quad \text{A.5}$$

Due to the assumption of constant viscosity across the fluid film viscosity can be taken outside of the partial differentiation. Integrating across the bearing clearance (z direction depicted in Figure A.1) will produce equations for u and w.

$$\iint \frac{\partial P}{\partial x} dzdz = \iint \mu \frac{\partial^2 u}{\partial y^2} dzdz \quad \text{A.6}$$

The solution to equation A.6 is an equation that describes the velocity profile in the x direction, equation A.7.

$$u = \frac{1}{2\mu} \frac{\partial P}{\partial x} z^2 + c_1 z + c_2 \quad \text{A.7}$$

Through a similar process, an equation for the velocity profile in the y direction (w) is shown in equation A.8 below.

$$v = \frac{1}{2\mu} \frac{\partial P}{\partial y} z^2 + c_3 z + c_4 \quad \text{A.8}$$

Any bearing motion in the axial direction is not considered for this analysis, thus the boundary conditions to solve for the four constants in equations A.7 and A.8 are shown in equation A.9.

$$u(z = 0) = U_1 \qquad u(z = h) = U_2 \qquad v(z = 0) = 0 \qquad v(z = h) = 0 \quad \text{A.9}$$

Applying these boundary conditions results in the following velocity profiles for the x-direction (A.10) and y-direction (A.11)

$$u = \frac{1}{2\mu}\frac{\partial P}{\partial x} z(z-h) + \frac{h-z}{h} U_1 + \frac{z}{h} U_2 \qquad \text{A.10}$$

$$v = \frac{1}{2\mu}\frac{\partial P}{\partial y} z(z-h) \qquad \text{A.11}$$

The conservation of mass for the differential element is investigated next. Similar to before, the mass conservation is first considered in the form of RTT, equation A.12.

$$0 = \frac{d}{dt}\int_V \rho dV + \int_S \rho(\vec{v}\cdot\vec{n})dS \qquad \text{A.12}$$

Figure A.3 shoes the various mass transport terms that cross the surfaces of the differential element.

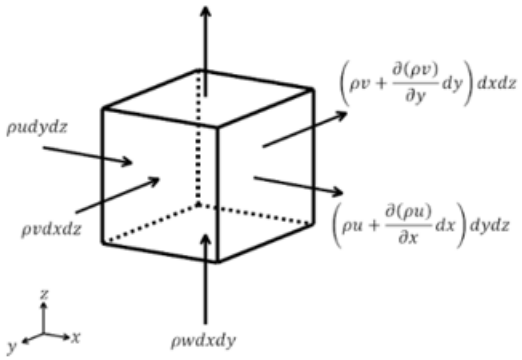

Figure A.3: Conservation of mass for the differential element.

In addition to the terms shown in figure A.3, the transient change in the density of the fluid must be accounted for in the conservation of mass. After simplifying these terms, equation A.13 displays the familiar form of the conservation of mass for the differential element.

$$\frac{\partial \rho}{\partial t} + \frac{\partial (\rho u)}{\partial x} + \frac{\partial (\rho v)}{\partial y} + \frac{\partial (\rho w)}{\partial z} = 0 \qquad \text{A.13}$$

Integration over the local radial clearance, h, from bearing surface 1 to bearing surface 2 is the next step. Integration of term I is shown below (equation A.14); note that density is constant across the gap.

$$\int_0^h \frac{\partial \rho}{\partial t} dz = \frac{\partial \rho}{\partial t} \int_0^h dz = h \frac{\partial \rho}{\partial t} \qquad \text{A.14}$$

Term IV is next to be considered; velocities V_1 and V_2 from figure A.1 are used to form the boundary conditions show in equation A.15.

$$w(z = 0) = V_1 \qquad w(z = h) = V_2 \qquad \text{A.15}$$

Applying these boundary conditions while executing the integral in the z direction across the bearing gap results in a solution in terms of V_2 and V_1, shown in A.16.

$$\int_0^h \frac{\partial (\rho w)}{\partial z} dz = (\rho w)|^h - (\rho w)|^0 = \rho V_2 - \rho V_1 \qquad \text{A.16}$$

To evaluate the integrals for terms II and III, the Leibnitz integral rule must be utilized to switch the order of the integral and derivative since h could be a function of either x, y or both. The Leibnitz integral rule for moving an outside integral with a constant lower bound (in this case 0) within a partial derivative is reviewed below in equation A.17. When applied to terms II and III, ZZ is either x or y.

$$\int_0^{h(\xi)} \frac{\partial}{\partial \xi} f(\xi, z) dz = \frac{\partial}{\partial \xi} \int_0^{h(\xi)} f(\xi, z) dz + f(\xi, z) \frac{\partial 0}{\partial \xi} - f(\xi, h) \frac{\partial h}{\partial \xi} \qquad \text{A.17}$$

Applying the Leibnitz integral rule to term II and III results in equations A.18 and A.19. The value of u(x,h) and v(x,h) were given in equation A.9.

$$\int_0^{h(x)} \frac{\partial(\rho u)}{\partial x} = \frac{\partial}{\partial x}\int_0^{h(x)} \rho u dz - \rho u(x,h)\frac{dh}{dx} \quad \text{A.18}$$

$$\int_0^{h(y)} \frac{\partial(\rho v)}{\partial y} = \frac{\partial}{\partial y}\int_0^{h(y)} \rho v dz - \rho v(y,h)\frac{dh}{dy} \quad \text{A.19}$$

The velocities u and v are replaced with the form determined in equations A.10 and A.11 and the integral is solved analytically.

$$\frac{\partial}{\partial x}\int_0^{h(x)} \rho\left(\frac{1}{2\mu}\frac{\partial P}{\partial x}z(z-h) + \frac{h-z}{h}U_1 + \frac{z}{h}U_2\right)dz - \rho\left(\frac{1}{2\mu}\frac{\partial P}{\partial x}h(h-h) + \frac{h-h}{h}U_1 + \frac{h}{h}U_2\right)\frac{dh}{dx} \quad \text{A.20}$$

$$\frac{\partial}{\partial x}\left(\frac{-\rho h^3}{12\mu}\frac{\partial P}{\partial x} + \frac{\rho h}{2}U_1 + \frac{\rho h}{2}U_2\right) - \rho U_2\frac{dh}{dx}$$

A similar process is carried out for term III.

$$\frac{\partial}{\partial y}\int_0^{h(y)} \rho\left(\frac{1}{2\mu}\frac{\partial P}{\partial y}z(z-h)\right)dz = \frac{\partial}{\partial y}\left(\frac{-\rho h^3}{12\mu}\frac{\partial P}{\partial y}\right) \quad \text{A.21}$$

Combining the executed integrals, the form of the mass conservation equation (A.13) produces the following form of the Reynolds equation (A.22).

$$h\frac{\partial \rho}{\partial t} + \frac{\partial}{\partial x}\left(\frac{-\rho h^3}{12\mu}\frac{\partial P}{\partial x} + \frac{\rho h}{2}U_1 + \frac{\rho h}{2}U_2\right) - \rho U_2\frac{dh}{dx} + \frac{\partial}{\partial y}\left(\frac{-\rho h^3}{12\mu}\frac{\partial P}{\partial y}\right) + \rho V_2 - \rho V_1 = 0 \quad \text{A.22}$$

In this derivation, V_1 is considered to be any potential injection velocity (V_{inj}). The other shaft motion terms, U_1, U_2 and V_2 are analyzed after the equation is rearranged to a form more familiar to the Reynolds equation, equation A.23.

$$\frac{\partial}{\partial x}\left(\frac{\rho h^3}{12\mu}\frac{\partial P}{\partial x}\right) + \frac{\partial}{\partial y}\left(\frac{\rho h^3}{12\mu}\frac{\partial P}{\partial y}\right) = h\frac{\partial \rho}{\partial t} + \frac{\partial}{\partial x}\left(\rho h\frac{U_1+U_2}{2}\right) - \rho U_2\frac{dh}{dx} + \rho V_2 - \rho V_{inj} \quad \text{A.23}$$

Due to the angle, α, the velocity $V_2$and U_2 are made up of components of velocity from both rotational velocity and shaft motion (transient change in eccentricity). The velocities are illustrated in Figure A.4. In the figure, the subscript of x or y indicates the direction of velocity. $V_{2,0}$ is the velocity of the wall normal to surface 2 while $U_{2,0}$ is the velocity of the wall tangential to surface 2. $V_2$and U_2 are made from components of each.

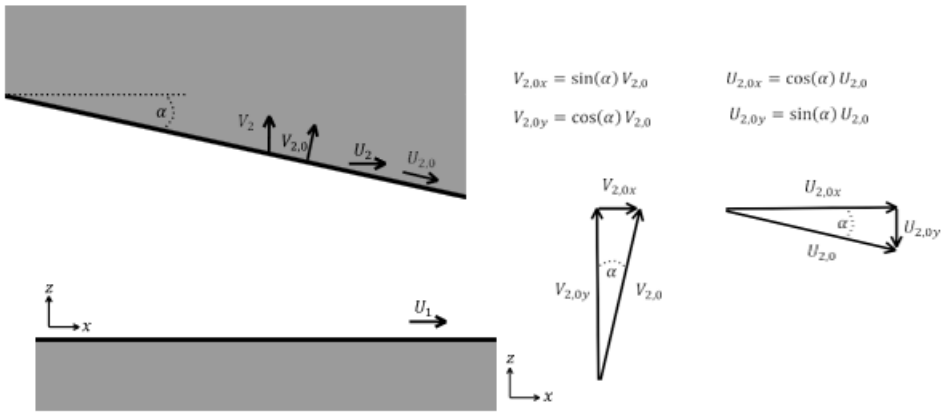

Figure A.4: Depiction of the x direction and z direction components of velocity.

The shaft velocity in the x direction is made up primarily of the motion parallel to the boundary, $U_{2,0x}$. Additionally, it is made up of shaft motion due to a transient change in eccentricity, $V_{2,0x}$. However, $V_{2,0}$ is assumed to be small compared to the rotational velocity, $U_{2,0}$, and sin (α) is assumed to be small. Therefore, $V_{2,0x}$ is neglected in equation A.25.

$$U_2 = U_{2,0x} + V_{2,0x} = \overbrace{\cos(\alpha)}^{\approx 1} U_{2,0} + \overbrace{\sin(\alpha) V_{2,0}}^{\ll U_{2,0x}} \approx U_{2,0} \quad \text{A.24}$$

The shaft velocity in the y direction is also made up of two components. In this case, the cos(α) term is acting on the $V_{2,0}$ term and is approximated as being equal to one due to alpha being small. Due to the potentially large value of $U_{2,0}$, a different approach is taken to the approximation compared to that in equation A. 24.

$$V_2 = U_{2,0y} + V_{2,0y} = \sin(\alpha) U_{2,0} + \overbrace{\cos(\alpha)}^{\approx 1} V_{2,0} \approx \sin(\alpha) U_{2,0} + V_{2,0} \quad \text{A.25}$$

The value of sin(α) for this equation was again approximated, but this time with a slightly different take to conveniently create a differential function.

$$\sin(\alpha) \approx \frac{\sin(\alpha)}{\cos(\alpha)} = \tan(\alpha) = \frac{\partial h}{\partial x} \quad \text{A.26}$$

Additionally, $V_{2,0}$is rewritten as the velocity normal to surface 2 in the form of a derivative, $\frac{\partial h}{\partial t}$.

$$V_2 \approx U_{2,0} \frac{dh}{dx} + \frac{\partial h}{\partial t} \quad \text{A.27}$$

Applying these approximations to equation A.23 yields a nearly finalized form the Reynolds equation, equation A.28

$$\frac{\partial}{\partial x}\left(\frac{\rho h^3}{12\mu}\frac{\partial P}{\partial x}\right) + \frac{\partial}{\partial y}\left(\frac{\rho h^3}{12\mu}\frac{\partial P}{\partial y}\right) = h\frac{\partial \rho}{\partial t} + \frac{\partial}{\partial x}\left(\rho h \frac{U_1 + U_{2,0}}{2}\right) - \rho(U_{2,0}\frac{dh}{dx} + \frac{\partial h}{\partial t}) - \rho V_{inj} \quad \text{A.28}$$

The final assumption applied is that the bushing would not have motion, therefore making $U_1 = 0$. Simplification of the above equation, applying this assumption and renaming $U_{2,0}$ to simply U concludes the development of the modified Reynolds equation for the solid bearing.

$$\frac{\partial}{\partial x}\left(\frac{\rho h^3}{12\mu}\frac{\partial P}{\partial x}\right) + \frac{\partial}{\partial y}\left(\frac{\rho h^3}{12\mu}\frac{\partial P}{\partial y}\right) = \frac{\partial(\rho h)}{\partial t} + \frac{\partial}{\partial x}\left(\frac{\rho h U}{2}\right) - \rho V_{inj} \quad \text{A.29}$$

This thesis needs a modified Reynolds equation for a porous bearing, which requires a more thorough investigation into V_{inj}. The fluid injection from the porous medium is represented by Darcy's law, equation A.30.

$$\frac{dP}{dr} = -\frac{\mu_f}{K} V_{inj} \quad \text{A.30}$$

Equation A.30 can be rearranged to solve for the injection velocity. Note that the 'r' direction is the direction perpendicular to the fluid film of the unwrapped bearing; the thickness of the porous medium.

$$V_{inj} = \frac{-dP}{dr}\frac{K}{\mu_f} \quad \text{A.31}$$

Incorporating this new definition for V_{inj} a more complete equation for the modified Reynolds equation is obtained, equation A.32.

$$\frac{\partial}{\partial x}\left(\frac{\rho h^3}{12\mu}\frac{\partial P}{\partial x}\right) + \frac{\partial}{\partial y}\left(\frac{\rho h^3}{12\mu}\frac{\partial P}{\partial y}\right) = \frac{\partial(\rho h)}{\partial t} + \frac{\partial}{\partial x}\left(\frac{\rho h U}{2}\right) + \rho\frac{dP}{dr}\frac{K}{\mu_f} \quad \text{A.32}$$

APPENDIX B

POROUS BUSHING SOLUTION

Starting with a differential element within the porous medium, the fluxes in each direction can be drawn and collected, equation B.1.

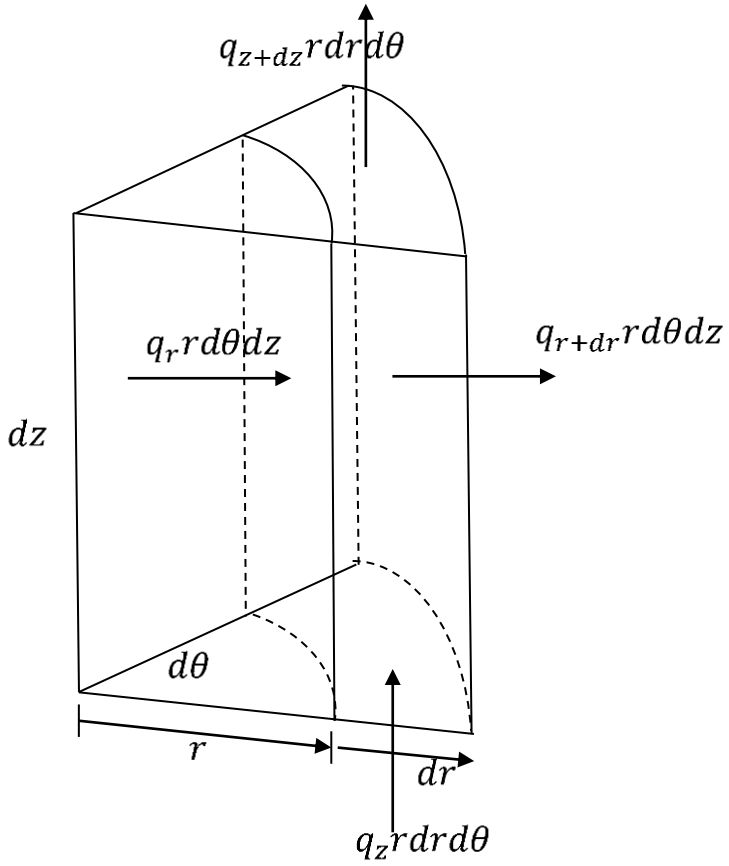

$$(q_r - q_{r+dr})rd\theta dz - q_{r+dr}rd\theta dz + (q_\theta - q_{\theta+d\theta})drdz + (q_z - q_{z+dz})drd\theta = 0 \quad \text{B.1}$$

Where q represents the fluid flow within the porous medium. Applying the definition of a derivative and eliminating like terms leads to equation B.2.

$$\frac{1}{r}\frac{\partial}{\partial r}r\frac{\partial q}{\partial r}+\frac{1}{r^2}\frac{\partial^2 q}{\partial \theta^2}+\frac{\partial^2 q}{\partial z^2}=0 \qquad \text{B.2}$$

The flow within the porous medium is pressure driven and damped by the permeability of the fluid-medium pairing.

$$q=kP \qquad \text{B.3}$$

Substituting the definition of q and assuming that the permeability is constant in all directions leads to the 3D Laplace equation, B.4.

$$\frac{1}{r}\frac{\partial}{\partial r}r\frac{\partial P}{\partial r}+\frac{1}{r^2}\frac{\partial^2 P}{\partial \theta^2}+\frac{\partial^2 P}{\partial z^2}=0 \qquad \text{B.4}$$

The figure below shows the three axes. Z represents the axial direction where a parabolic distribution is expected along the length of the bearing (measured from 0 to L). The θ direction represents the circumferential direction of the unwrapped bearing and is defined from 0 to 2π. The r direction is the radial direction, or the axis through the thickness of the unwrapped porous medium, extends from R_i at the interface between the fluid film and the porous medium. The problem has the following boundary conditions (B.5)

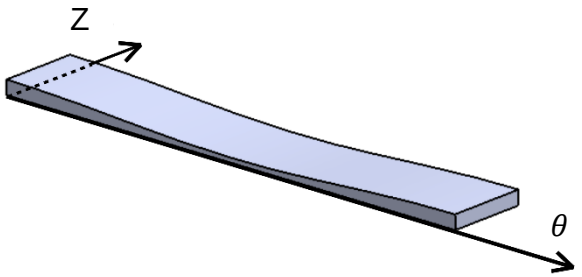

As seen above, both ends of the bearing are exposed to a reference pressure. Periodic boundary conditions are present in the circumferential direction. In the radial direction, at the inner radius, R_i, the pressure is equal to the bearing pressure and at the outer radius, R_o, the pressure is equal to a supply pressure. Equating the bearing and porous media pressures, P_b and P_s respectively, at the interface is considered a no-slip boundary condition at the interface. The discussion of this boundary condition can be seen in the literature review portion of this thesis.

Original Boundary Conditions		
Z direction	$p(r,\theta,z=0)=p_{ref}$ $p(r,\theta,z=L)=p_{ref}$	B.5
R direction	$p(r=R_i,\varphi,z)=p_b$ $p(r=R_o,\theta,z)=p_s$	
θ direction	$p(r,\theta,z)=p(r,\theta+2\pi,z)$ $\frac{\partial p}{r\partial\theta}(r,\theta,z)=\frac{\partial p}{r\partial\theta}(r,\theta+2\pi,z)$	

To simplify the boundary conditions, a change of variable is employed which defines the pressure found in solution to be defined based on the reference pressure, not zero. This will create a second homogeneous direction in the axial direction.

$$P = p - p_{ref} \tag{B.6}$$

Change of Variable Boundary Conditions		
Z direction	$P(r, \theta, z = 0) = 0$ $P(r, \theta, z = L) = 0$	B.7
R direction	$P(r = R_i, \theta, z) = P_b$ $P(r = R_o, \theta, z) = P_s$	
θ direction	$P(r, \theta, z) = P(r, \theta + 2\pi, z)$ $\frac{\partial P}{r\partial\theta}(r, \theta, z) = \frac{\partial P}{r\partial\theta}(r, \theta + 2\pi, z)$	

Superposition can be used to separate the problem by splitting the R direction boundary conditions. The first problem will have the boundary condition at the bearing surface set equal to zero and the second will have the boundary condition at the outer edge of the porous bearing set equal to zero. The split problems are shown below for reference.

First Problem	Second Problem
$\frac{1}{r}\frac{\partial}{\partial r}r\frac{\partial P_1}{\partial r}+\frac{1}{r^2}\frac{\partial^2 P_1}{\partial \theta^2}+\frac{\partial^2 P_1}{\partial z^2}=0$	$\frac{1}{r}\frac{\partial}{\partial r}r\frac{\partial P_2}{\partial r}+\frac{1}{r^2}\frac{\partial^2 P_2}{\partial \theta^2}+\frac{\partial^2 P_2}{\partial z^2}=0$
$P_1(r,\theta,z=0)=0$ $P_1(r,\theta,z=L)=0$	$P_2(r,\theta,z=0)=0$ $P_2(r,\theta,z=L)=0$
$P_1(r=R_i,\theta,z)=0$ $P_1(r=R_o,\theta,z)=P_s$	$P_2(r=R_i,\theta,z)=P_b$ $P_2(r=R_o,\theta,z)=0$
$P_1(r,v,z)=P_1(r,\theta+2\pi,z)$ $\frac{\partial P_1}{r\partial\theta}(r,\theta,z)=\frac{\partial P_1}{r\partial\theta}(r,\theta+2\pi,z)$	$P_2(r,\theta,z)=P_2(r,\theta+2\pi,z)$ $\frac{\partial P_2}{r\partial\theta}(r,\theta,z)=\frac{\partial P_2}{r\partial\theta}(r,\theta+2\pi,z)$

After each of these problems is solved, $P_1$and P_2 will be added together to get the total pressure distribution within the porous media. This development will solve the first problem and then the second problem.

As can be seen in the table above, there are two homogeneous directions: the axial and circumferential directions. Separation of variables is used to find a solution in each direction that can then be multiplied with the others to form the pressure solution for the first problem.

$$P_1 = RZ\Phi \qquad \text{B.8}$$

The new definition for P_1 is used in the governing equation resulting in B.9.

$$\Phi Z\frac{1}{r}\frac{\partial}{\partial r}r\frac{\partial R}{\partial r}+RZ\frac{1}{r^2}\frac{\partial^2\Phi}{\partial\theta^2}+R\Phi\frac{\partial^2 Z}{\partial z^2}=0 \qquad \text{B.9}$$

The governing equation can be rearranged to separate the z direction terms and equate the two sides of the equation to a constant which results in a homogeneous equation in the z direction.

$$\frac{1}{R}r\frac{\partial}{\partial r}r\frac{\partial R}{\partial r}+\frac{1}{\Phi}\frac{1}{r^2}\frac{\partial^2\Phi}{\partial\theta^2}-\lambda^2=0 \qquad \text{B.10}$$

$$\frac{\partial^2 Z}{\partial z^2}+\lambda^2 Z=0 \qquad \text{B.11}$$

Once again, the variables of B.12 are separated and set equal to a constant which results in a homogeneous equation in the circumferential direction.

$$\frac{1}{R}r\frac{\partial}{\partial r}r\frac{\partial R}{\partial r}-\lambda^2r^2=\frac{-1}{\Phi}\frac{\partial^2\Phi}{\partial\theta^2}=\mu^2 \qquad \text{B.12}$$

$$\frac{1}{R}r\frac{\partial}{\partial r}r\frac{\partial R}{\partial r}-\lambda^2r^2-\mu^2=0 \qquad \text{B.13a}$$

$$\frac{\partial^2\Phi}{\partial\theta^2}+\mu^2\Phi=0 \qquad \text{B.13b}$$

Equation B.13a is in the form of a modified Bessel equation. Using the Bessel solution [73] with the boundary condition at the inner radius (where pressure=0) the solution in the radial direction is achieved with unknown coefficient E.

$$R(r) = E[I_\mu(\lambda r) - \frac{I_\mu(\lambda R_i)}{K_\mu(\lambda R_i)} K_\mu(\lambda r)] \quad \text{B.14}$$

Equation B.11 is revisited with the boundary conditions that pressure is equal to zero at the edges of the bearing to find the solution in the axial direction.

$$Z = \sum_{n=1}^{\infty} B_n \sin(\lambda_n z) \ \ where\ \lambda_n = \frac{n\pi}{L} \quad \text{B.15}$$

Similarly, equation B.13b results in the following equation in the circumferential direction.

$$\Phi = C_o + \sum_{m=1}^{\infty} (C_m \cos(m\theta) + D_m \sin(m\theta) \quad \text{B.16}$$

Recomposing the solution from the separation of variables the following is obtained.

$$P_1 = \sum_{n=1}^{\infty} E_{no} C_o B_n \left[I_0(\lambda r) - \frac{I_o(\lambda R_i)}{K_o(\lambda R_i)} K_o(\lambda r) \right] \sin(\lambda_n z) +$$

$$\sum_{n=1}^{\infty} \sum_{m=1}^{\infty} (C_m B_n E_{nm} \cos(m\theta) + D_m B_n E_{nm} \sin(m\theta)) [I_\mu(\lambda r) -$$

$$\frac{I_\mu(\lambda R_i)}{K_\mu(\lambda R_i)} K_\mu(\lambda r)] \sin(\lambda_n z) \qquad \text{B.17}$$

The coefficients can be combined into one coefficient. $\mu_m = m = 1,2,3 \ldots$ simplifies the Bessel form of the solution to be a member of the 'm' infinite series. The simplified solution for problem one is below.

$$P_1 = \sum_{n=1}^{\infty} a_{no} \left[I_0(\lambda r) - \frac{I_o(\lambda R_i)}{K_o(\lambda R_i)} K_o(\lambda r) \right] \sin(\lambda_n z) + \sum_{n=1}^{\infty} \sum_{m=1}^{\infty} (a_{mn} \cos(m\theta) +$$

$$b_{nm} \sin(m\theta)) [I_\mu(\lambda r) - \frac{I_\mu(\lambda R_i)}{K_\mu(\lambda R_i)} K_\mu(\lambda r)] \sin(\lambda_n z) \qquad \text{B.18}$$

The remaining boundary condition, $P_1(r = R_o, \varphi, z) = P_s$, will be used to solve for the coefficients. After applying the boundary condition orthogonality is applied in the circumferential direction. To complete the process, orthogonality is applied in the axial direction.

$$a_{no} \left[I_0(\lambda R_o) - \frac{I_o(\lambda R_i)}{K_o(\lambda R_i)} K_o(\lambda R_o) \right] = \frac{P_s \left(\frac{-1}{\lambda_n} \right) \cos(\lambda_n z) |_0^L}{\int_0^L sin^2(\lambda_n z) dz} = \frac{\frac{-P_s}{\lambda_n} (\cos(n\pi - 1))}{L/2} \qquad \text{B.19}$$

The same process reveals that $a_{mn}\ and\ b_{nm}$ are both zero for the first solution. The final form of the solution to the first problem is shown below.

$$P_1(r,\theta,z) = \sum_{n=0}^{\infty} \frac{-2P_s(\cos(n\pi-1))}{\lambda_n L} \frac{\left[I_0(\lambda r) - \frac{I_o(\lambda R_i)}{K_o(\lambda R_i)} K_o(\lambda r)\right]}{\left[I_0(\lambda R_o) - \frac{I_o(\lambda R_i)}{K_o(\lambda R_i)} K_o(\lambda R_o)\right]} sin(\lambda_n z) \quad \text{B.20}$$

The second problem now needs to be solved for pressure. Again, separation of variables is used to obtain individual solutions in each direction that can be later combined. These equations are the same as seen in problem one for the axial and circumferential directions since the only difference in boundary conditions occurs in the radial direction. Thus, in addition to B.15 and B.16, the radial direction equation is below.

$$R(r) = E[I_\mu(\lambda r) - \frac{I_\mu(\lambda R_o)}{K_\mu(\lambda R_o)} K_\mu(\lambda r)] \quad \text{B.21}$$

Again, these solutions are multiplied together which results in many coefficients that can be combined to form just three coefficients that will need solved.

$$P_2 = \sum_{n=1}^{\infty} a_{no} \left[I_0(\lambda r) - \frac{I_o(\lambda R_o)}{K_o(\lambda R_o)} K_o(\lambda r)\right] \sin(\lambda_n z) + \sum_{n=1}^{\infty} \sum_{m=1}^{\infty} (a_{mn} \cos(m\theta) + b_{nm} \sin(m\theta))[I_\mu(\lambda r) - \frac{I_\mu(\lambda R_o)}{K_\mu(\lambda R_o)} K_\mu(\lambda r)] \sin(\lambda_n z) \quad \text{B.22}$$

The last boundary condition, , $P_2(r = R_i, \theta, z) = P_b$, will be used to solve for the coefficients. The Fourier series that was populated at each axial location, forming a piecewise solution is detailed in B.23.

$$y = f_0 + \sum_{k=1}^{8} f_k \cos(k\omega x) + g_k \sin(k\omega x) \quad \text{B.23}$$

Next, the constants need to be fully defined. The first constant solved will be a_{no}. The remaining boundary condition, that $P_2(r = R_i, \theta, z) = P_b$ is used to solve for the constant.

After setting the pressure at the outside radius is set equal to the bearing pressure, each side is multiplied by $\cos m\varphi$ and integrated from 0 to 2π with $m = 0$.

$$\sum_{n=1}^{\infty} a_{no}[I_\mu(\lambda R_i) - \frac{I_\mu(\lambda R_o)}{K_\mu(\lambda R_o)} K_\mu(\lambda R_i)] \sin \lambda_n z \int_0^{2\pi} \cos m\theta \, d\theta =$$

$$\int_0^{2\pi} P_b(\theta, z) \cos(m\theta) \, d\theta \quad \text{B.24}$$

$$\sum_{n=1}^{\infty} a_{no}[I_\mu(\lambda R_i) - \frac{I_\mu(\lambda R_o)}{K_\mu(\lambda R_o)} K_\mu(\lambda R_i)] \sin \lambda_n z = \frac{1}{2\pi} \int_0^{2\pi} P_b(\theta, z) \, d\theta$$

B.25

$$\int_0^{2\pi} P_b(\theta) \, d\theta = \int_0^{2\pi} f_0 \, d\varphi + \int_0^{2\pi} f_k \cos(k\omega\theta) \, d\theta + \int_0^{2\pi} g_k \sin(k\omega\theta) \, d\theta$$

B.26

$$\int_0^{2\pi} P_b(\theta) \, d\varphi = 2\pi(\sum_{k=0}^{8} f_k + \sum_{k=1}^{8} g_k)$$

B.27

Orthogonality in the axial direction continues:

$$\sum_{n=1}^{\infty} a_{no}[I_\mu(\lambda R_i) - \frac{I_\mu(\lambda R_o)}{K_\mu(\lambda R_o)} K_\mu(\lambda R_i)] \int_0^L sin^2(\lambda_n z)\, dz = \int_0^L 2\pi(\sum_{k=0}^{8} f_k + \sum_{k=1}^{8} g_k) sin(\lambda_n z)\, dz \quad \text{B.28}$$

The infinite series is approximated by n=1 to n=8 because there are only eight terms in the Fourier series. Since the only non-zero terms are those when the arguments are equal, the infinite series is only non-zero for the eight terms where the trigonometric arguments are the same.

$$\sum_{n=1}^{\infty} a_{no}[I_\mu(\lambda R_i) - \frac{I_\mu(\lambda R_o)}{K_\mu(\lambda R_o)} K_\mu(\lambda R_i)] = \frac{1}{\pi L} \int_0^L 2\pi\, (\sum_{k=0}^{8} f_k + \sum_{k=1}^{8} g_k) sin(\lambda_n z)\, dz \quad \text{B.29}$$

$$a_{no} = \frac{2}{L} \frac{1}{[I_\mu(\lambda R_i) - \frac{I_\mu(\lambda R_o)}{K_\mu(\lambda R_o)} K_\mu(\lambda R_i)]} \int_0^L (\sum_{k=0}^{8} f_k + \sum_{k=1}^{8} g_k)\, sin(\lambda_n z)\, dz \quad \text{B.30}$$

The integral will be integrated using the trapezoid method. Each axial location will have a different coefficient (from the piecewise Fourier curve fit).

The second constant solved for, a_{mn}, also uses the properties of orthogonality for trigonometric functions in both the phi and z direction.

$$\int_0^{2\pi} P_b(\theta, z)\, cos(m\theta)\, d\theta = \sum_{n=1}^{\infty} a_{mn}[I_\mu(\lambda R_i) -$$

$$\frac{I_\mu(\lambda R_o)}{K_\mu(\lambda R_o)} K_\mu(\lambda R_i)]\, sin(\lambda_n z) \int_0^{2\pi} cos^2(m\theta)\, d\theta \qquad \text{B.29}$$

$$\sum_{n=1}^{\infty} a_{mn}[I_\mu(\lambda R_i) - \frac{I_\mu(\lambda R_o)}{K_\mu(\lambda R_o)} K_\mu(\lambda R_i)]\, sin(\lambda_n z) = \frac{1}{\pi}\int_0^{2\pi} P_b(\theta, z)\, cos(m\theta)\, d\theta \qquad \text{B.31}$$

$$\int_0^{2\pi} P_b(\theta)\, cos(m\theta)\, d\theta = \int_0^{2\pi} f_0\, cos(m\theta)\, d\theta + \int_0^{2\pi} f_k\, cos(k\omega\theta)\, cos(m\theta)\, d\theta +$$

$$\int_0^{2\pi} g_k sin(k\omega\theta) cos(m\theta)\, d\theta \qquad \text{B.32}$$

The Fourier fit was limited to having $\omega = 1$, so the orthogonality between trigonometric functions is applicable. This leads to two cases, when the arguments are equal and when they are not. If the arguments are not equal, then the second integral is equal to zero. If the arguments are equal then the second integral becomes cos^2 and is equal to $f_k\pi$. The third integral is always equal to zero, as is the first integral.

If the arguments are equal then the next step in solving for the constant is to use orthogonality in the axial direction.

$$\sum_{n=1}^{\infty} a_{nm}\, [I_\mu(\lambda R_i) - \frac{I_\mu(\lambda R_o)}{K_\mu(\lambda R_o)} K_\mu(\lambda R_i)] \int_0^L sin(\lambda_n z)\, dz = \frac{1}{\pi}\int_0^L f_k \pi\, sin(\lambda_n z)\, dz \qquad \text{B.33}$$

The integral from zero to *L* is evaluated for each term of the Fourier series remaining from orthogonality in the circumferential direction, represented by f_k. The integral is evaluated using the trapezoid rule.

$$\sum_{n=1}^{\infty} a_{nm} = \frac{2}{L}\frac{1}{[I_\mu(\lambda R_i) - \frac{I_\mu(\lambda R_o)}{K_\mu(\lambda R_o)}K_\mu(\lambda R_i)]}\int_0^L f_k \sin(\lambda_n z)\, dz \qquad \text{B.34}$$

Next, b_{nm} is solved for using the same methods as a_{nm}.

$$\int_0^{2\pi} P_b(\theta, z)\sin(m\theta)\, d\theta = \sum_{n=1}^{\infty} b_{nm}[I_\mu(\lambda R_i) - \frac{I_\mu(\lambda R_o)}{K_\mu(\lambda R_o)}K_\mu(\lambda R_i)]\sin(\lambda_n z)\int_0^{2\pi}\sin^2(m\theta)\, d\theta \qquad \text{B.35}$$

Orthogonality in the phi direction:

$$\int_0^{2\pi} P_b(\theta, z)\sin(m\theta)\, d\theta = \sum_{n=1}^{\infty} b_{nm}[I_\mu(\lambda R_i) - \frac{I_\mu(\lambda R_o)}{K_\mu(\lambda R_o)}K_\mu(\lambda R_i)]\sin(\lambda_n z)\int_0^{2\pi}\sin^2(m\theta)\, d\theta \qquad \text{B.36}$$

$$\sum_{n=1}^{\infty} b_{mn}[I_\mu(\lambda R_i) - \frac{I_\mu(\lambda R_o)}{K_\mu(\lambda R_o)}K_\mu(\lambda R_i)]\sin(\lambda_n z) = \frac{1}{\pi}\int_0^{2\pi} P_b(\theta, z)\sin(m\theta)\, d\theta \qquad \text{B.37}$$

$$\int_0^{2\pi} P_b(\theta)\sin(m\theta)\, d\theta = \int_0^{2\pi} f_0 \sin(m\theta)\, d\theta + \int_0^{2\pi} f_k \cos(k\omega\theta)\sin(m\theta)\, d\theta + \int_0^{2\pi} g_k \sin(k\omega\theta)\sin(m\theta)\, d\theta \qquad \text{B.38}$$

Again, using trigonometric orthogonality, the second integral is equal to zero since arguments have been limited to integers. The third integral is only non-zero when the arguments are equal. The first integral is always zero.

If the arguments are equal then the next step in solving for the constant is to use orthogonality in the axial direction.

$$\sum_{n=1}^{\infty} b_{mn}[I_\mu(\lambda R_i) - \frac{I_\mu(\lambda R_o)}{K_\mu(\lambda R_o)} K_\mu(\lambda R_i)] \int_0^L sin^2\, \lambda_n z\, dz = \frac{1}{\pi} \int_0^L P_b(z)\, sin(\lambda_n z)\, dz \quad \text{B.39}$$

The integral from zero to *L* is evaluated for each term of the Fourier series remaining from orthogonality in the circumferential direction, represented by g_k.

$$\sum_{n=1}^{\infty} b_{mn} = \frac{1}{[I_\mu(\lambda R_i) - \frac{I_\mu(\lambda R_o)}{K_\mu(\lambda R_o)} K_\mu(\lambda R_i)]} \frac{1}{\pi} \int_0^L g_k \pi\, sin(\lambda_n z)\, dz \quad \text{B.40}$$

$$b_{nm} = \frac{2}{L} \frac{1}{[I_\mu(\lambda R_i) - \frac{I_\mu(\lambda R_o)}{K_\mu(\lambda R_o)} K_\mu(\lambda R_i)]} \int_0^L g_k\, sin(\lambda_n z)\, dz \quad \text{B.41}$$

The full solution is now:

$$P(r,\theta,z) = \sum_{n=0}^{\infty} \frac{-2P_s(\cos(n\pi - 1))}{\lambda_n L} \frac{\left[I_0(\lambda r) - \frac{I_o(\lambda R_i)}{K_o(\lambda R_i)} K_o(\lambda r)\right]}{\left[I_0(\lambda R_o) - \frac{I_o(\lambda R_i)}{K_o(\lambda R_i)} K_o(\lambda R_o)\right]} sin(\lambda_n z) +$$

$$\sum_{n=1}^{\infty} a_{no} \left[I_0(\lambda r) - \frac{I_o(\lambda R_o)}{K_o(\lambda R_o)} K_o(\lambda r)\right] \sin(\lambda_n z) + \sum_{n=1}^{\infty} \sum_{m=1}^{\infty} (a_{mn} \cos(m\theta) +$$

$$b_{nm} \sin(m\theta))[I_\mu(\lambda r) - \frac{I_\mu(\lambda R_o)}{K_\mu(\lambda R_o)} K_\mu(\lambda r)] \sin(\lambda_n z) \quad \text{B.42}$$

Where

$$a_{no} = \frac{1}{\pi L} \frac{1}{[I_\mu(\lambda R_i) - \frac{I_\mu(\lambda R_o)}{K_\mu(\lambda R_o)} K_\mu(\lambda R_i)]} \int_0^L \left(\sum_{k=0}^{8} f_k + \sum_{k=1}^{8} g_k \right) sin(\lambda_n z)\, dz$$

$$a_{nm} = \frac{2}{L} \frac{1}{[I_\mu(\lambda R_i) - \frac{I_\mu(\lambda R_o)}{K_\mu(\lambda R_o)} K_\mu(\lambda R_i)]} \int_0^L f_k\, sin(\lambda_n z)\, dz$$

$$b_{nm} = \frac{2}{L} \frac{1}{[I_\mu(\lambda R_i) - \frac{I_\mu(\lambda R_o)}{K_\mu(\lambda R_o)} K_\mu(\lambda R_i)]} \int_0^L g_k\, sin(\lambda_n z)\, dz$$

APPENDIX C

MATLAB CODE

Global Script for Self-Circulating Bearing with Rayleigh-Plesset-Scriven Cavitation

```
clear
is_energy_on = 1;       %0, energy off
                        %1, energy on
%data file info
date=011524;
varA='HTCboth';
%VAR=[0.1 0.2 0.3];
VAR = [20 50 100];
%VAR = [3.75*10^(-2) 3.75*10^(-3) 3.75*10^(-4)];
%VAR = [1000 5000 10000];
for MM=1:1
var=VAR(MM);
pflag=['q','r','s','d','e'];

%ER=[0.1 0.2 0.3 0.4 0.5 0.6 0.7 0.8 0.9];
ER=[0.2 0.4 0.6 0.8];
for N=4:4
icase=N;
cflag=['A','B','C','D','E','F','G','H'];

%insert if loop to switch between cases
%bearing geometry and operating conditions---------
wrpm=5000;              %rotational frequency [rpm]
er=ER(N);                %eccentricity ratio
R_bearing=12.426*10^(-3);       %shaft radius meters [m]
L=38.1*10^(-3);               %bearing length [m]
C=0.0254*10^(-3);       %clearance [m]
e=er*C;                 %eccentricity [m]
Pinf=101325;            %atmospheric or surrounding pressure [Pa]

%-----------------------------------------------------

%Cav model settings--------------------------------------
kap=3.75*10^(-3);       %Dilatation Viscosity
%kap=var;
init_void=1e-2;         %initial void fraction
```

```
R_char=2e-05;           %charachteristic bubble radius
S=0.035;                %surface tension of bubble
%-------------------------------------------------------

%spatial and temporal step size, grid gen-----------------
dt=1E-6;                %time step [s]
y_div=61;               %steps in axial direction
x_div=200;              %steps in circumpherential direction

%grid generation function
[x,y,dx,dy,h]= gen_grid(R_bearing,L,x_div,y_div,e,C);
%-------------------------------------------------------
%supply pressure surrounding porous media [Pa]
for i=1:length(x)
Ps(i)=(-9e6*x(i)^6 +2e6*x(i)^5 +132891*x(i)^4 -45455*x(i)^3 +1174.1*x(i)^2
+65.96*x(i) +4.0068)*1000;
end

%fluid properties for isothermal simulation----------------------------
if is_energy_on ==0
    RhoL=840.724*ones(length(x),length(y)); %Density of oil kg/m^3 (for
isothermal calcs)
    MuL=0.00689;                            %Viscosity of oil [Pas]
(isothermal calcs)
    MuL=ones(length(x),length(y))*MuL;      %Matrix for MuL, needed for cav
model
    MuB=2.12076e-5;                         %Visosity of gas bubble
(isothermal calcs)
end
%-----------------------------------------------------------------------

%-------parameters for energy equation
htc_0=var;            %htc coeficients
htc_h=var;
T0=80;                  %initial temp
RhoB0=1.225*(288.15)/(273.15+T0)*Pinf/101325; %initial density of air
T=T0*ones(length(x),length(y));         %initial value of T
T0=T;                                   %value of T0 in matrix form
%-------------------------

%Relaxation factors and sim convergence settings--------------------

%relaxation factors must all be 1 for a time accurate simulation; also
%see note in the Reynolds equation section of this script. Mess with these
%as you wish if only a steady state solution is required
%P_relax = 0.5 and alpha_relax=0.5 seems to work well for most
%simulations... also consider reducing time step to 1e-6... for smaller
%values of kappa such as O(10^-4), a denser grid may be necessary due to
%rapid bubble collapse.

rlxMu=1;                %Relaxation coefficient for Mixture Dynamic Viscosity
rlxRho=1;               %Relaxation coefficient for Mixture Density
P_relax=0.2;            %Relaxation coefficient for Pressure after first sweep
alpha_relax=0.1;        %Relaxation coefficient for void fraction
```

```
T_lim=750;              %limit the value of T (helps low HTC conditions avoid
simulation failure)
T_relax=0.5;            %Relaxation coefficient for temperature
Vinj_relax=0.2;         %relaxtion coefficient for Vinj

min_iter=300;          %minimum number of iterations
load_conv=1e-7;         %value of load_tol to determine load has converged
alpha_conv=1e-7;        %same, determines alpha convergence
T_conv=1e-8;            %same, determines Temp convergence
Total_conv=1e-5;        %same, determines load conv between Vinj loops

%-------------------------------------------------------

%Porous Properties
H=0.2*R_bearing;       %thickness of porous media [m]
Ro=R_bearing+H;          %outer radius of porous media [m]
Ri=R_bearing;
r_div=5;                 %number of steps in porous media
K=1e-12;            %viscous permeability or fluid conductivity [m^2]

inject_relax=0.01;      %Relaxation coefficient for injection velocity

%computed bearing properties
w=wrpm*2*pi/60;         %rotational frequency [rad/s]
U=w*R_bearing;          %sliding speed [m/s]


%Initialze bubble size and void fraction
alpha=ones(length(x),length(y))*init_void;
A=R_char/init_void^(1/3);
P0=Pinf+2*S./R_char;         %initial bubble pressure

    %----------- Energy Equation initializations-------------%
if is_energy_on==1

    e_new=zeros(length(x),length(y));
    c=ones(length(x),length(y))*2150;


    k_oil=0.120;    %heat conduction coefficient of the oil
    ktherm=ones(length(x),length(y))*k_oil; %k in matrix form


    T_bush=80;                                  %Temo of bushing
    T_sh=80;                                    %Temp of shaft

%viscosity equation

    AA=5.58E-5;
    BB=911.03;
    CC=109.15;
    MuL=AA*exp(BB./(T+CC)); %Viscosity of Oil (kg/m-s)
    Mu_inj=AA*exp(BB./(80+CC));
    lambda=1.512E-6;          %several constants grouped together
    CCC=120;                  %Sutherland's Constant
```

```
    T_k= T + 273.15;
    MuB=lambda*T_k.^1.5./(T_k+CCC);    % Viscosity of gas in bubble Pa.s

    %Density equation
    AAA=889.5;
    BBB=-0.6097;
    RhoL= AAA + BBB*T;              %Density of Oil(kg/m^3)
end

% Initialize Pressure, Mu, Rho, other stuff

P=Pinf*ones(length(x),length(y));
Mu=alpha.*MuB+(1-alpha).*MuL; %Dynamic viscosity of mixture

RhoB=RhoB0*ones(length(x),length(y));
Rho=alpha.*RhoB+(1-alpha).*RhoL;
Uave=zeros(length(x),length(y));
dpdx=zeros(length(x),length(y));
Vave=zeros(length(x),length(y));
dpdy=zeros(length(x),length(y));
R_averaged=zeros(length(x),length(y));
V_inj=zeros(length(x),length(y));
Vinj_old=zeros(length(x),length(y));
% More initialization
load=0;
load_tol=1;
Alphtol=1;
Alphsum=0;
T_sum=0;


phi1=linspace(0,2*pi,length(x));  %rotating coordinate system angle (for load
calc)
for i = 1:length(y)
phi(:,i)=phi1;                   %Matrix for this angle (used in Fx,Fy
equation)
end
%% Vinj loop
count=2;
VLoad=[0 1];
Totalerr=1;
while abs(Totalerr)>Total_conv
%%
iter = 1;
whichdir=1;
Vinj_old=V_inj;
%% Global loop
while abs(Alphtol) > alpha_conv ||iter < min_iter || abs(load_tol)> load_conv
|| abs(Ttol) > T_conv

    %Store old vaues
    alpha_old=alpha;
    load_old=load;
    P_old=P;
    Rho_old=Rho;
```

```
if is_energy_on == 1
    T_old=T;
end
    h_old=h;

%============================RP Equation=====================

%average velocities and pressure gradients
[Uave,Vave,dpdx,dpdy] = vel_and_press_grad(P,dpdx,dpdy,U,h,Mu,...
                                    dx,dy,x,y);


%Cavitation model

[ alpha ] = Cav_model122122(P0,P,T0,T,R_char,alpha,alpha_old,A,kap,...
                                S,MuL,Uave,Vave,dt,dx,dy,x,y,alpha_relax);

RhoB=RhoB0*R_char.^3./(A.*alpha.^(1/3)).^3; %bubble density

%================Energy Equation=====================


if is_energy_on == 1
energy=c.*T;
Q_gen=Mu*U^2./h + h.^3./(12*Mu).*(dpdx.^2+dpdy.^2);
    T=energy_equation_solver(T,T_sh,T_bush,energy,e_new,c,ktherm,Rho,...
                             htc_h,htc_0,Q_gen,Vave,Uave,dt,dx,dy,x,y,h);


    for i=1:length(x)
        for j=1:length(y)
            if T(i,j) > T_lim
                T(i,j)= T_lim;
            end
        end
    end
    T=(1-T_relax)*T_old+(T_relax)*T;    %Temp Relaxation

    %-------------Vary Properies due to temp variation---------------
    MuL=AA*exp(BB./(T+CC)); %Viscosity of liquid as f(T)
    RhoL= AAA + BBB*T;      %Density of liquid as f(T)
    T_k= T + 273.15;        %Temp in kelvin, use in bubble visc equation
    MuB=lambda*T_k.^1.5./(T_k+CCC);      % Viscosity of gas in bubble Pa.s

    %bubble pressure is affected by temp in the RP_solver function

end


Rho_new=alpha.*RhoB+(1-alpha).*RhoL;    %update Rho
Mu_new=alpha.*MuB+(1-alpha).*MuL;       %update Mu
Mu=rlxMu*Mu_new+(1-rlxMu).*Mu;          %Mu relaxation
Rho=rlxRho*Rho_new+(1-rlxRho)*Rho;      %Rho Relaxation
```

```
%====================== Reynolds Equation solution===========
M=Rho.*h.^3./(12.*Mu); %these terms are gouped into a single variable

P = Reynolds_solver_semi_implicit(
M,x,y,dx,dy,dt,U,Rho,RhoL,h,Rho_old,h_old,P,V_inj);
P = (1-P_relax)*P_old+(P_relax)*P;    %Pressure Relaxation


%%%%%%%%%%%%%%%%%%%%%%%%%%%%%%%%%%%%%%%%%%%%%%%%%%%%%%%%%%%%%%%%%%%%%%%
%load Tolerance Compute and Print

iter=iter+1; %next iteration



Alphsum_old=Alphsum;                  %store old Rsum
Alphsum=sum(sum(alpha));               %new Rsum (convergence property)
Alphtol=(Alphsum-Alphsum_old)/Alphsum; %normalized difference previous and
current step
Fr=sum(sum(P.*dx*dy.*cos(phi))); %radial force
Ft=sum(sum(P.*dx*dy.*sin(phi))); %tangential force
at=atan2d(Ft,Fr);    %attitude angle, only important for placing injector in
theta reference frame
load=sqrt(Fr^2+Ft^2) ;          %load compuation
T_sum_old=T_sum;
T_sum=sum(sum(T));
Ttol=(T_sum-T_sum_old)/T_sum;



load_tol=(load-load_old)/load;  %load convergence property
max_alpha=max(max(alpha));
min_Uave=min(min(Uave));
max_T=max(max(T));
clc
fprintf('Iteration: %g \nAlpha tol: %g \nLoad tol:  %g \nTemp tol:  %g \n
\nMax Alpha: %g \nMin U Vel: %g \nMax Temp:  %g \n',...
    iter, Alphtol,load_tol,Ttol,max_alpha,min_Uave,max_T)

end
%figure(1)
%surf(y,x,P)
store(count)=iter;
%============================Injection=============================

%[dpdr,Ptotal,P1,P2]=Porous_Media_122122(L,Ps,Ro,R_bearing,r_div,y_div,x_div,P
,Pinf);
[dpdr,Ptotal,P1,P2]=Porous_Media_062323(L,Ps,Ro,R_bearing,r_div,y_div,x_div,P,
Pinf);
V_inj=-K.*dpdr;          %Darcy's law
V_inj = (1-Vinj_relax)*Vinj_old+(Vinj_relax)*V_inj;    %Pressure Relaxation
VLoad(count)=load;           %saving the load from previous Re-Cav solution
% % % Totalerr=(VLoad(count)-VLoad(count-1))/VLoad(count);    %total
convergence
count=count+1;
```

```
% figure(2)
% surf(y,x,V_inj)
end
%data storage
%first the file for parameters

filename = ['cavPara' cflag(N) pflag(MM) '2.out'];
fid=fopen(filename,'a');
%File_ID=fopen(filename,'a');
fprintf(fid,'Iteration: %g \nAlpha tol: %g \nLoad tol:  %g \nTemp tol:  %g
\nMax Alpha: %g \nMin U Vel: %g \nMax Temp:  %g \nDate %g \n',...
    iter, Alphtol,load_tol,Ttol,max_alpha,min_Uave,max_T,date);
fprintf(fid,'Load: %g\nAttitude Angle: %g\nspeed: %g\neccentricity
%g\nLength: %g\nRadius: %g\nClearance: %g\nPinf: %g\nx_div: %g\ny_div:
%g\n',...
    load,at,wrpm,er,L,R_bearing,C,Pinf,x_div,y_div);
fprintf(fid,'%s\n','changing Parameter: HTC');
fprintf(fid,'load_conv= %g \nmin_iter= %g\nalpha_conv= %g\nVinj
%g\n',load_conv,min_iter,alpha_conv,V_inj(1,1));
fprintf(fid,'Ft= %g\nFr= %g\nRo= %g\nThickness porous= %g\nPermeability=
%g\nVisosity= %g\n',Ft,Fr,Ro,H,K,kap);
fclose(fid);
    filename = ['cavPress' cflag(N) pflag(MM) '2.mat'];
    save(filename,'P'); %this stores a matlab matrix

    filename = ['cavVoid' cflag(N) pflag(MM) '2.mat'];
    save(filename,'alpha');

    filename = ['cavUave' cflag(N) pflag(MM) '2.mat'];
    save(filename,'Uave');

    filename = ['cavVave' cflag(N) pflag(MM) '2.mat'];
    save(filename,'Vave');

    filename = ['cavVinj' cflag(N) pflag(MM) '2.mat'];
    save(filename,'V_inj');

    filename = ['cavTemp' cflag(N) pflag(MM) '2.mat'];
    save(filename,'T');
test(MM,N)=load;
end
end
```

Grid Generation Function

```
function [x,y,dx,dy,h,L_unwrap]= gen_grid(R_bearing,L,x_div,y_div,e,C)

%This function generates the grid for the cavitation model
%y points and step size
y=linspace(0,L,y_div);      %y grid setup
dy=y(2)-y(1);               %y step

%x points and step size
L_unwrap=2*pi*R_bearing;
x=linspace(0,L_unwrap,x_div);
dx=x(2)-x(1);
h=jbFilmThickness(x,y,e,C,R_bearing); %Set Height
```

Velocity and Pressure Gradient Function

```
function [Uave,Vave,dpdx,dpdy] = vel_and_press_grad(P,dpdx,dpdy,U,h,Mu,...
                                    dx,dy,x,y)
%determine pressure gradient for velocity calculations
    for j = 2:length(y)-1
        for i=1:length(x)
            dpdy(i,j)=(P(i,j+1)-P(i,j-1))/(2*dy);
        end
        for i=2:length(x)-1
            dpdx(i,j)=(P(i+1,j)-P(i-1,j))/(2*dx);

        end
    end
    for j=2:length(y)-1
       dpdx(length(x),j)=(P(2,j)-P(length(x)-1,j))/dx;
    end

    Uave=U/2-dpdx.*h.^2./(12.*Mu);  %avg circumpherential velocity
    Vave=-dpdy.*h.^2./(12.*Mu);      %avg axial velocity
    Uave(1,:)=Uave(length(x),:);    %first and last circum positions are the
same position
```

Rayleigh-Plesset-Scriven Cavitation Function

```
function [ alpha ] =
Cav_model122122(P0,P,T0,T,R_char,alpha,alpha_old,A,kap,...
                                S,MuL,Uave,Vave,dt,dx,dy,x,y,alpha_relax)

Pb=P0.*R_char.^3.*(273+T)./((273+T0).*(A.*alpha_old.^(1/3)).^3);

for i=2:length(x)
     for j=2:length(y)-1

        if Uave(i,j)>=0
            if Vave(i,j)>=0
                alpha(i,j)=alpha_old(i,j)+dt*(3*alpha_old(i,j)^(2/3)/A*...
                    (Pb(i,j)-P(i,j)-2*S/(A*alpha_old(i,j)^(1/3)))...
                    /(4*MuL(i,j)/(A*alpha_old(i,j)^(1/3))...
                    +4*kap/(A*alpha_old(i,j)^(1/3))^2)...
                    -Uave(i,j)*(alpha_old(i,j)-alpha_old(i-1,j))/dx...
                    -Vave(i,j)*(alpha_old(i,j)-alpha_old(i,j-1))/dy);
            else
                alpha(i,j)=alpha_old(i,j)+dt*(3*alpha_old(i,j)^(2/3)/A*...
                    (Pb(i,j)-P(i,j)-2*S/(A*alpha_old(i,j)^(1/3)))...
                    /(4*MuL(i,j)/(A*alpha_old(i,j)^(1/3))...
                    +4*kap/(A*alpha_old(i,j)^(1/3))^2)...
                    -Uave(i,j)*(alpha_old(i,j)-alpha_old(i-1,j))/dx...
                    -Vave(i,j)*(alpha_old(i,j+1)-alpha_old(i,j))/dy);
            end

        else

            if Vave(i,j)>=0
                if i==length(x)
                    alpha(i,j)=alpha_old(i,j)+dt*(3*alpha_old(i,j)^(2/3)/A*...
                        (Pb(i,j)-P(i,j)-2*S/(A*alpha_old(i,j)^(1/3)))...
                        /(4*MuL(i,j)/(A*alpha_old(i,j)^(1/3))...
                        +4*kap/(A*alpha_old(i,j)^(1/3))^2)...
                        -Uave(i,j)*(alpha_old(1,j)-alpha_old(i,j))/dx...
                        -Vave(i,j)*(alpha_old(i,j)-alpha_old(i,j-1))/dy);
                else
                    alpha(i,j)=alpha_old(i,j)+dt*(3*alpha_old(i,j)^(2/3)/A*...
                        (Pb(i,j)-P(i,j)-2*S/(A*alpha_old(i,j)^(1/3)))...
                        /(4*MuL(i,j)/(A*alpha_old(i,j)^(1/3))...
                        +4*kap/(A*alpha_old(i,j)^(1/3))^2)...
                        -Uave(i,j)*(alpha_old(i+1,j)-alpha_old(i,j))/dx...
                        -Vave(i,j)*(alpha_old(i,j)-alpha_old(i,j-1))/dy);
                end

            else

                if i==length(x)
                    alpha(i,j)=alpha_old(i,j)+dt*(3*alpha_old(i,j)^(2/3)/A*...
                        (Pb(i,j)-P(i,j)-2*S/(A*alpha_old(i,j)^(1/3)))...
                        /(4*MuL(i,j)/(A*alpha_old(i,j)^(1/3))...
                        +4*kap/(A*alpha_old(i,j)^(1/3))^2)...
```

```
                        -Uave(i,j)*(alpha_old(1,j)-alpha_old(i,j))/dx...
                        -Vave(i,j)*(alpha_old(i,j+1)-alpha_old(i,j))/dy);

                else
                    alpha(i,j)=alpha_old(i,j)+dt*(3*alpha_old(i,j)^(2/3)/A*...
                        (Pb(i,j)-P(i,j)-2*S/(A*alpha_old(i,j)^(1/3)))...
                        /(4*MuL(i,j)/(A*alpha_old(i,j)^(1/3))...
                        +4*kap/(A*alpha_old(i,j)^(1/3))^2)...
                        -Uave(i,j)*(alpha_old(i+1,j)-alpha_old(i,j))/dx...
                        -Vave(i,j)*(alpha_old(i,j+1)-alpha_old(i,j))/dy);
                end
            end
        end

    end
end

alpha(1,:)=alpha(length(x),:);
alpha=(1-alpha_relax)*(alpha_old)+alpha_relax*alpha; %relaxation of bubble
radius values
for i=1:length(x)
    for j=1:length(y)
        if alpha(i,j)>0.99
            alpha(i,j)=0.99;
        end
%         if alpha(i,j)<0.01
%             alpha(i,j)=0.01;
%         end
    end
end
```

Reynolds Equation Function

```
function [ P ] = Reynolds_solver_semi_implicit( M,x,y,dx,dy,dt,U,Rho,RhoL,...
    h,Rho_old,h_old,P,Vinj)
%Reynolds Equation Solve Function
%   Semi-implicit MATRIX formation.  The values for P(i,j+1) are from
%   previous time step.  All others are from current step.
MAT=sparse(length(x),length(x));
for j=2:length(y)-1
    for i=2:length(x)-1
            MAT(i,i-1)=M(i,j)/dx^2-(M(i+1,j)-M(i-1,j))/(4*dx^2);
    end

    for i=2:length(x)-1
            MAT(i,i)=-2*M(i,j)/dx^2-2*M(i,j)/dy^2;
    end

    for i=2:length(x)-1
            MAT(i,i+1)=M(i,j)/dx^2+(M(i+1,j)-M(i-1,j))/(4*dx^2);
    end

    for i=1:length(x)
```

```
            if i == 1
                D(i,1)=0;
            elseif i > 1 && i < length(x)
                D(i,1)=(Rho(i,j)*h(i,j) - Rho_old(i,j)*h_old(i,j))/dt + ...
                    U/(4*dx)*(Rho(i+1,j)*h(i+1,j) - Rho(i-1,j)*h(i-1,j)) - ...
                    M(i,j)*(P(i,j+1)+P(i,j-1))/dy^2-...
                    (M(i,j+1)-M(i,j-1))*(P(i,j+1)-P(i,j-1))/(4*dy^2)-...
                    RhoL(i,j)*Vinj(i,j);
            elseif i == length(x)
                D(i,1)=0;
            end
    end
    %Boundary Condition

    MAT(1,1)=1;
    MAT(1,length(x))=-1;
    MAT(length(x),2)=0.5;
    MAT(length(x),length(x)-1)=0.5;
    MAT(length(x),length(x))=-1;
    u=MAT\D;


    P(1:length(x),j)=u;

end
end
```

Energy Equation Function

```
function [ T ] =
energy_equation_solver(T,T_sh,T_bush,energy,e_new,c,ktherm,Rho,...
                           htc_h,htc_0,Q_gen,Vave,Uave,dt,dx,dy,x,y,h)

for i = 2:length(x)-1
    for j = 2:length(y)-1
        if Vave(i,j) > 0
            if Uave(i,j)>=0
e_new(i,j)=energy(i,j)+...
    dt*(-Uave(i,j)*(c(i,j)*T(i,j)-c(i-1,j)*T(i-1,j))/dx - ...
    Vave(i,j)*(c(i,j)*T(i,j)-c(i,j-1)*T(i,j-1))/dy + ...
    ktherm(i,j)/Rho(i,j)*(T(i,j+1)-2*T(i,j)+T(i,j-1))/dy^2 + ...
    1/(Rho(i,j)*h(i,j))*(-htc_h*(T(i,j)-T_sh)-htc_0*(T(i,j)-
T_bush)+Q_gen(i,j)));
            else
                e_new(i,j)=energy(i,j)+...
    dt*(-Uave(i,j)*(c(i+1,j)*T(i+1,j)-c(i,j)*T(i,j))/dx - ...
    Vave(i,j)*(c(i,j)*T(i,j)-c(i,j-1)*T(i,j-1))/dy + ...
    ktherm(i,j)/Rho(i,j)*(T(i,j+1)-2*T(i,j)+T(i,j-1))/dy^2 + ...
    1/(Rho(i,j)*h(i,j))*(-htc_h*(T(i,j)-T_sh)-htc_0*(T(i,j)-
T_bush)+Q_gen(i,j)));
            end

        else
            if Uave(i,j)>=0
e_new(i,j)=energy(i,j)+...
    dt*(-Uave(i,j)*(c(i,j)*T(i,j)-c(i-1,j)*T(i-1,j))/dx - ...
    Vave(i,j)*(c(i,j+1)*T(i,j+1)-c(i,j)*T(i,j))/dy + ...
    ktherm(i,j)/Rho(i,j)*(T(i,j+1)-2*T(i,j)+T(i,j-1))/dy^2 + ...
    1/(Rho(i,j)*h(i,j))*(-htc_h*(T(i,j)-T_sh)-htc_0*(T(i,j)-
T_bush)+Q_gen(i,j)));
            else
e_new(i,j)=energy(i,j)+...
    dt*(-Uave(i,j)*(c(i+1,j)*T(i+1,j)-c(i,j)*T(i,j))/dx - ...
    Vave(i,j)*(c(i,j+1)*T(i,j+1)-c(i,j)*T(i,j))/dy + ...
    ktherm(i,j)/Rho(i,j)*(T(i,j+1)-2*T(i,j)+T(i,j-1))/dy^2 + ...
    1/(Rho(i,j)*h(i,j))*(-htc_h*(T(i,j)-T_sh)-htc_0*(T(i,j)-
T_bush)+Q_gen(i,j)));
            end
        end
    end
end
i=length(x);
    for j = 2:length(y)-1
        if Vave(i,j) > 0
            if Uave(i,j)>=0
e_new(i,j)=energy(i,j)+...
    dt*(-Uave(i,j)*(c(i,j)*T(i,j)-c(i-1,j)*T(i-1,j))/dx - ...
    Vave(i,j)*(c(i,j)*T(i,j)-c(i,j-1)*T(i,j-1))/dy + ...
    ktherm(i,j)/Rho(i,j)*(T(i,j+1)-2*T(i,j)+T(i,j-1))/dy^2 + ...
    1/(Rho(i,j)*h(i,j))*(-htc_h*(T(i,j)-T_sh)-htc_0*(T(i,j)-
T_bush)+Q_gen(i,j)));
```

```
            else
                e_new(i,j)=energy(i,j)+...
    dt*(-Uave(i,j)*(c(2,j)*T(2,j)-c(i,j)*T(i,j))/dx - ...
    Vave(i,j)*(c(i,j)*T(i,j)-c(i,j-1)*T(i,j-1))/dy + ...
    ktherm(i,j)/Rho(i,j)*(T(i,j+1)-2*T(i,j)+T(i,j-1))/dy^2 + ...
    1/(Rho(i,j)*h(i,j))*(-htc_h*(T(i,j)-T_sh)-htc_0*(T(i,j)-
T_bush)+Q_gen(i,j)));
            end

        else
            if Uave(i,j)>=0
e_new(i,j)=energy(i,j)+...
    dt*(-Uave(i,j)*(c(i,j)*T(i,j)-c(i-1,j)*T(i-1,j))/dx - ...
    Vave(i,j)*(c(i,j+1)*T(i,j+1)-c(i,j)*T(i,j))/dy + ...
    ktherm(i,j)/Rho(i,j)*(T(i,j+1)-2*T(i,j)+T(i,j-1))/dy^2 + ...
    1/(Rho(i,j)*h(i,j))*(-htc_h*(T(i,j)-T_sh)-htc_0*(T(i,j)-
T_bush)+Q_gen(i,j)));
            else
e_new(i,j)=energy(i,j)+...
    dt*(-Uave(i,j)*(c(2,j)*T(2,j)-c(i,j)*T(i,j))/dx - ...
    Vave(i,j)*(c(i,j+1)*T(i,j+1)-c(i,j)*T(i,j))/dy + ...
    ktherm(i,j)/Rho(i,j)*(T(i,j+1)-2*T(i,j)+T(i,j-1))/dy^2 + ...
    1/(Rho(i,j)*h(i,j))*(-htc_h*(T(i,j)-T_sh)-htc_0*(T(i,j)-
T_bush)+Q_gen(i,j)));
            end
        end
    end

Tnew=e_new./(c);
T(:,2:length(y)-1)=Tnew(:,2:length(y)-1);
T(1,:)=T(length(x),:);
```

Porous Bushing Function

```
function
[dpdr,Ptotal,P1,P2]=Porous_Media_062323(L,Ps,Ro,Ri,r_div,z_div,x_div,P,Pinf)

%tic
% script for porous closed form solution
%This script runs with minimal functions and no symbolic variables
%develops the 3D pressure in the porous media
%double fourier series is used as the curve fit

%turn warnings off
%warning('off','all')
P=P';               %converts from (x,y) to (y,x)

%span of each dimension
phi_div=x_div;
R=linspace(Ri,Ro,r_div);               %coordinate for height in porous
Z=linspace(0,L,z_div);                 %axial coordinate, keep same #div as Pb
PHI=linspace(0,2*pi,phi_div);            %circumference coord, keep same #div
as Pb
r_step=R(2)-R(1);
z_step=30;                           %number of divisions in axial direction

P=P-Pinf;                            %change of variable
Ps=Ps-Pinf;                          %change of variable
%% preallocate vectors
% v=zeros(1,20);
% term2=zeros(8,20);
% sum1=zeros(1,5);
% P1=zeros(r_div,z_div,phi_div);
% P2=zeros(r_div,z_div,phi_div);
% c=zeros(z_step,18);
% Ano=zeros(1,20);
% Amn=zeros(8,30);
% Bmn=zeros(8,30);
% lambda=zeros(1,20);
% dpdr=zeros(z_step,phi_div);
% test1=zeros(1,15);
%% Creating a function for bearing pressure f(z,phi)

%forming the coefficient matrix for the bearing pressure distribution
for jj=1:length (Z)
    test=P(jj,:);
    [fitresult, gof] = createFit081621(PHI, test);
    c(jj,:)=coeffvalues(fitresult);
end

%Predetermine Bessel Functions
for n=1:20
    lambda(n)=n*pi/L;              %changes value along with the infinite
series
```

```
    BessAno(n)=(besseli(0,lambda(n)*Ri)-
(besseli(0,lambda(n)*Ro)/besselk(0,lambda(n)*Ro))*besselk(0,lambda(n)*Ri));
%expression from Ano
    BessVden(n)=(besseli(0,lambda(n)*Ro)-
(besseli(0,lambda(n)*Ri)/besselk(0,lambda(n)*Ri))*besselk(0,lambda(n)*Ro));
%expression from denom of v(nn)
   % Vpart1(n)=((-2*Ps*(cos(n*pi)-1))/(lambda(n)*L));        %first term of
v(nn), P1 summation

    f=c(:,1).*sin(lambda(n).*Z(:)); %term for Ano
    AA(n)=((Z(2)-Z(1))/2) *(2*sum(f(:)));         %using the trapezodial
rule,using BC that sides=0 Pa

    f=c(:,2).*sin(lambda(n).*Z(:));       %Amn will be 'A' coeff*sin
    d=c(:,3).*sin(lambda(n).*Z(:));       %Bmn will be 'B' coeff*sin
    AA1(n)=((Z(2)-Z(1))/2) *(2*sum(f(:)));        %using BC that sides=0 Pa
    BB1(n)=((Z(2)-Z(1))/2) *(2*sum(d(:)));
    f=c(:,4).*sin(lambda(n).*Z(:));       %Amn will be 'A' coeff*sin
    d=c(:,5).*sin(lambda(n).*Z(:));       %Bmn will be 'B' coeff*sin
    AA2(n)=((Z(2)-Z(1))/2) *(2*sum(f(:)));        %using BC that sides=0 Pa
    BB2(n)=((Z(2)-Z(1))/2) *(2*sum(d(:)));
    f=c(:,6).*sin(lambda(n).*Z(:));       %Amn will be 'A' coeff*sin
    d=c(:,7).*sin(lambda(n).*Z(:));       %Bmn will be 'B' coeff*sin
    AA3(n)=((Z(2)-Z(1))/2) *(2*sum(f(:)));        %using BC that sides=0 Pa
    BB3(n)=((Z(2)-Z(1))/2) *(2*sum(d(:)));
    f=c(:,8).*sin(lambda(n).*Z(:));       %Amn will be 'A' coeff*sin
    d=c(:,9).*sin(lambda(n).*Z(:));       %Bmn will be 'B' coeff*sin
    AA4(n)=((Z(2)-Z(1))/2) *(2*sum(f(:)));        %using BC that sides=0 Pa
    BB4(n)=((Z(2)-Z(1))/2) *(2*sum(d(:)));
    f=c(:,10).*sin(lambda(n).*Z(:));       %Amn will be 'A' coeff*sin
    d=c(:,11).*sin(lambda(n).*Z(:));       %Bmn will be 'B' coeff*sin
    AA5(n)=((Z(2)-Z(1))/2) *(2*sum(f(:)));        %using BC that sides=0 Pa
    BB5(n)=((Z(2)-Z(1))/2) *(2*sum(d(:)));
    f=c(:,12).*sin(lambda(n).*Z(:));       %Amn will be 'A' coeff*sin
    d=c(:,13).*sin(lambda(n).*Z(:));       %Bmn will be 'B' coeff*sin
    AA6(n)=((Z(2)-Z(1))/2) *(2*sum(f(:)));        %using BC that sides=0 Pa
    BB6(n)=((Z(2)-Z(1))/2) *(2*sum(d(:)));
    f=c(:,14).*sin(lambda(n).*Z(:));       %Amn will be 'A' coeff*sin
    d=c(:,15).*sin(lambda(n).*Z(:));       %Bmn will be 'B' coeff*sin
    AA7(n)=((Z(2)-Z(1))/2) *(2*sum(f(:)));        %using BC that sides=0 Pa
    BB7(n)=((Z(2)-Z(1))/2) *(2*sum(d(:)));
    f=c(:,16).*sin(lambda(n).*Z(:));       %Amn will be 'A' coeff*sin
    d=c(:,17).*sin(lambda(n).*Z(:));       %Bmn will be 'B' coeff*sin
    AA8(n)=((Z(2)-Z(1))/2) *(2*sum(f(:)));        %using BC that sides=0 Pa
    BB8(n)=((Z(2)-Z(1))/2) *(2*sum(d(:)));
    for m=1:8
        BessABmn(m,n)=(besseli(m,lambda(n)*Ri)-
(besseli(m,lambda(n)*Ro)/besselk(m,lambda(n)*Ro))*besselk(m,lambda(n)*Ri));
%expression from Amn and Bmn
    end
end
Ano=(2/L).*(BessAno.^(-1)).*AA; %gives 1x20
%Ano=(2/(L*BessAno(:))).*AA(:);
Amn(1,:)=(2/L).*(BessABmn(1,:).^(-1)).*AA1;
Bmn(1,:)=(2/L).*(BessABmn(1,:).^(-1)).*BB1;
```

```
Amn(2,:)=(2/L).*(BessABmn(2,:).^(-1)).*AA2;
Bmn(2,:)=(2/L).*(BessABmn(2,:).^(-1)).*BB2;
Amn(3,:)=(2/L).*(BessABmn(3,:).^(-1)).*AA3;
Bmn(3,:)=(2/L).*(BessABmn(3,:).^(-1)).*BB3;
Amn(4,:)=(2/L).*(BessABmn(4,:).^(-1)).*AA4;
Bmn(4,:)=(2/L).*(BessABmn(4,:).^(-1)).*BB4;
Amn(5,:)=(2/L).*(BessABmn(5,:).^(-1)).*AA5;
Bmn(5,:)=(2/L).*(BessABmn(5,:).^(-1)).*BB5;
Amn(6,:)=(2/L).*(BessABmn(6,:).^(-1)).*AA6;
Bmn(6,:)=(2/L).*(BessABmn(6,:).^(-1)).*BB6;
Amn(7,:)=(2/L).*(BessABmn(7,:).^(-1)).*AA7;
Bmn(7,:)=(2/L).*(BessABmn(7,:).^(-1)).*BB7;
Amn(8,:)=(2/L).*(BessABmn(8,:).^(-1)).*AA8;
Bmn(8,:)=(2/L).*(BessABmn(8,:).^(-1)).*BB8;

% Pressure Calculation
for rr=2:r_div-1       %calculate pressure at inner radius points
    r=R(rr);            %define radius for the loop
 %preallocate Bessel function values
     for n=1:20     %formulate a vector of the bessel series to vectorize Q(n)
calc
           lambda(n)=n*pi/L;
           BessTop(n)=(besseli(0,lambda(n)*r)-
(besseli(0,lambda(n)*Ri)/besselk(0,lambda(n)*Ri))*besselk(0,lambda(n)*r));
%expression from V(nn) numerator
           BessQ(n)=(besseli(0,lambda(n)*r)-
(besseli(0,lambda(n)*Ro)/besselk(0,lambda(n)*Ro))*besselk(0,lambda(n)*r));
%expression from Q(n)
           %Q(n)=Ano(n)*(besseli(0,lambda*r)-
(besseli(0,lambda*Ro)/besselk(0,lambda*Ro))*besselk(0,lambda*r))*sin(lambda*z)
;
           for m=1:8
               Bess2(m,n)=(besseli(m,lambda(n)*r)-
(besseli(m,lambda(n)*Ro)/besselk(m,lambda(n)*Ro))*besselk(m,lambda(n)*r));
%expression from term2
           end
      end
for zz=1:z_div       %does not include boundaries
    z=Z(zz);            %define axial position for the loop

for phiphi=1:phi_div   %does not include boundaries
    phi=PHI(phiphi);    %assigning value from 0 to 2pi for the loop

%% P1 calculation
for n=1:20
Vpart1(n)=((-2*Ps(phiphi)*(cos(n*pi)-1))/(lambda(n)*L));        %first term of
v(nn), P1 summation
end
 v=Vpart1.*(BessTop./BessVden).*sin(lambda.*z);          %gives 1x20
    P1(rr,zz,phiphi)=sum(v(:));       %sum of series for P1; total P1 value

%Q=Ano(:).*BessQ(:).*sin(lambda(:).*z);
Q=Ano.*BessQ.*sin(lambda.*z);           %gives 1x20
term1=sum(Q(:));
for m=1:8
```

```
    test1(m,:)=(Amn(m,:).*cos(m*phi)+Bmn(m,:).*sin(m*phi));
    test2(m,:)=Bess2(m,:);
    test3(m,:)=sin(lambda(:).*z);
    inter(m,:)=test2(m,:).*test3(m,:);
    final(m,:)=test1(m,:).*inter(m,:);
    %inter2(m,:)=test1(m,:).*test2(m,:);
    %final2(m,:)=inter2(m,:).*test3(m,:);

%term2(m,:)=(Amn(m,:).*cos(m*phi)+Bmn(m,:).*sin(m*phi)).*Bess2(m,:).*sin(lambd
a(:).*z);
     sum1(m)=sum(final(m,:));  %"infinite" sum for n direction
end


 term2total=sum(sum1(:));    %"infinite" sum for m direction
 P2(rr,zz,phiphi)=term1+term2total;
end
end
end

Ptotal=P2+P1;               %total pressure

Ptotal(1,:,:)=P;                %at r=1 the pressure in porous media=bearing
pressure from Reynolds
for i=1:phi_div
Ptotal(r_div,:,i)=Ps(i);           %at r=r_step (Ro) Ps value outside the
bearing
end

Ptotal=Ptotal+Pinf;             %undoing change of variable for derivative
%% Calculating dPdr
%To use Darcy's law to calculate the injection velocity, need the change in
%pressure across the thickness of the porous medium
%we will be using a backwards difference method with second order error
for i=1:length(Z)
    for j=1:length(PHI)
        %backward difference
        dpdr(i,j)=(3*Ptotal(1,i,j)-4*Ptotal(2,i,j)+Ptotal(3,i,j))/(2*r_step);
        %forward difference
        %dpdr(i,j)=(-3*Ptotal(1,i,j)+4*Ptotal(2,i,j)-
Ptotal(3,i,j))/(2*r_step);
    end
end
%toc
dpdr=dpdr';     %converts from (y,x) to (x,y)
```

Curve Fit Function

```
function [fitresult, gof] = createFit081621(PHI, test)
%CREATEFIT(PHI,TEST)
%  Create a fit.
%
%  Data for 'untitled fit 1' fit:
%      X Input : PHI
%      Y Output: test
%  Output:
%      fitresult : a fit object representing the fit.
%      gof : structure with goodness-of fit info.
%
%  See also FIT, CFIT, SFIT.

%  Auto-generated by MATLAB on 19-Jul-2021 12:49:12


%% Fit: 'untitled fit 1'.
[xData, yData] = prepareCurveData( PHI, test );

% Set up fittype and options.
ft = fittype( 'fourier8' );
opts = fitoptions( 'Method', 'NonlinearLeastSquares' );
opts.Display = 'Off';
opts.Lower = [-Inf -Inf -Inf -Inf -Inf -Inf -Inf -Inf -Inf -Inf -Inf -Inf -Inf
-Inf -Inf -Inf -Inf 1];
opts.StartPoint = [0 0 0 0 0 0 0 0 0 0 0 0 0 0 0 0 0 1];
opts.Upper = [Inf Inf Inf Inf Inf Inf Inf Inf Inf Inf Inf Inf Inf Inf Inf Inf Inf
Inf 1];

% Fit model to data.
[fitresult, gof] = fit( xData, yData, ft, opts );
```